UNIVERSITY OF CALIFORNIA
Los Angeles

Electron-THz Wave Interactions in a Guided Inverse Free Electron Laser

A dissertation submitted in partial satisfaction
of the requirements for the degree
Doctor of Philosophy in Physics

by

Emma Joyce Curry Snively

2018

ABSTRACT OF THE DISSERTATION

Electron-THz Wave Interactions
in a Guided Inverse Free Electron Laser

by

Emma Joyce Curry Snively
Doctor of Philosophy in Physics
University of California, Los Angeles, 2018
Professor Pietro Musumeci, Chair

The THz frequency regime holds the possibility of a new frontier in advanced accelerator research. In bridging the gap between optical and RF technology, THz-based accelerating structures can retain advantages from both, achieving high field gradients while maintaining large temporal acceptance relative to beam size. These features make THz radiation an exciting tool for beam manipulation, but, thus far, exploration of its application to accelerator physics has been limited by the low power of today's THz source technology, typically limited to a μJ-level pulse energy, often in a near single cycle waveform.

In this dissertation, we present a guiding technique for phase and group velocity matched interaction between a near single cycle THz pulse and an electron beam copropagating in a magnetic undulator. This "zero-slippage" scheme results in efficient energy exchange, necessary for utilizing a low power THz source, and in extended interaction, necessary for harnessing short and intense THz pulses, along with unique features like broadband coupling and tunable resonance that stem from the waveguide-induced dispersion. We explore the applications of "zero-slippage" coupling in an inverse free electron laser (IFEL), for THz-driven acceleration and beam manipulation, and a free electron laser (FEL), for broadband THz amplification or a stand-alone THz source based on spontaneous superradiance.

To model this novel interaction regime, we developed a 1-dimensional FEL simulation tool that tracks the THz pulse undergoing dispersion in a waveguide, along with the longitudinal

phase space dynamics of the beam. The experimental work presented in this dissertation includes a THz IFEL and FEL experiment, both conducted on the PEGASUS beamline at UCLA using a 30 cm, planar, permanent magnet undulator and 1 μJ-level laser-based THz source. The THz IFEL experiment produced a record 150 keV energy modulation of the relativistic beam, verified the tunable resonance of the guided IFEL interaction, and provided longitudinal phase space measurements demonstrating potential applications of the technique, including bunch compression by a factor of two.

Measurements from the THz FEL experiment show evidence of both stimulated amplification/absorption of the THz seed pulse, and spontaneous superradiant emission, due to the short bunch length relative to THz wavelength after bunch compression driven by the PEGASUS linac. Extrapolating to a 100-200 pC beam in a tapered undulator, simulations predict corresponding THz outputs exceeding 100 μJ with up to 30 % beam energy extraction, from broadband amplification with a long beam or spontaneous superradiance from a short beam, inviting the development of exciting and competitive new THz sources using the "zero-slippage" FEL technology.

The dissertation of Emma Joyce Curry Snively is approved.

James Rosenzweig

Benjamin Joel Schwartz

Pietro Musumeci, Committee Chair

University of California, Los Angeles

2018

To my mothers

TABLE OF CONTENTS

1 Introduction **1**

1.1 Inverse Free Electron Laser acceleration 2

1.1.1 Transverse ponderomotive vs. longitudinal coupling 4

1.2 THz frequencies 6

1.3 A "Zero-slippage" IFEL 8

1.4 Outline of this dissertation 11

2 The "Zero-Slippage" Inverse Free Electron Laser **12**

2.1 IFEL Theory 12

2.1.1 A waveguide IFEL 19

2.2 "Zero-Slippage" velocity matching 22

2.2.1 THz pulse description 26

2.3 "Zero-slippage" IFEL Simulations 30

2.3.1 WAFFEL Simulation Code: Wide-bandwidth AmpliFication in a Free Electron Laser 31

2.4 THz-driven transverse deflection 36

2.4.1 GPT simulations of a THz-driven streaking diagnostic 41

3 Experimental Techniques: THz generation, detection, and guided propagation **46**

3.1 Optical rectification 47

3.1.1 Pulse front tilting for optical rectification 50

3.2 THz source setup 56

3.2.1 THz detection 58

3.2.2 THz transport . . . 59
3.3 Electro-Optic Sampling . . . 61
3.4 Curved Parallel Plate Waveguide . . . 67
3.4.1 EOS measurements of tunable group velocity . . . 70
3.4.2 CPPWG modes for THz streaking diagnostic . . . 73
3.5 THz detection using photoconductive antennas . . . 77

4 THz IFEL Experiment . . . 85
4.1 Guided IFEL design and construction . . . 86
4.1.1 Undulator design . . . 87
4.1.2 CPPWG and mount design . . . 93
4.2 PEGASUS Beamline: Experimental setup . . . 93
4.2.1 THz generation . . . 93
4.2.2 UV generation . . . 96
4.2.3 Electron beam . . . 98
4.3 THz IFEL measurements . . . 105
4.3.1 Tunable IFEL resonance condition . . . 110
4.3.2 Longitudinal phase space measurements . . . 113
4.3.3 THz-driven bunch compression . . . 118

5 THz FEL Experiment . . . 124
5.0.1 THz diagnostics . . . 125
5.0.2 Electron bunch compression . . . 127
5.1 THz FEL measurements . . . 129
5.2 THz FEL simulations . . . 134
5.2.1 Broadband THz amplification . . . 135

5.2.2 Spontaneous superradiance 137

6 Conclusion 143

A EOS signal calculation 145

References 149

LIST OF FIGURES

1.1 Dispersion curves for "zero-slippage" interaction 9

2.1 Diagram of an IFEL 13
2.2 Particle trajectories in the ponderomotive bucket 18
2.3 Diagram of the guided IFEL, showing waveguide and undulator 20
2.4 Phase and group velocity matching conditions in a guided IFEL 25
2.5 Comparison of resonant interaction bandwidth 29
2.6 Visualizations of THz-driven streaking schemes 39
2.7 GPT simulations of beam trajectory through the undulator 42
2.8 GPT simulation results for THz streaking using the TE_{11} mode 43
2.9 GPT simulation results for THz streaking using the TE_{20} mode 44

3.1 Optical rectification with tilted laser pulse front 51
3.2 Pulse front tilt set-up using a diffraction grating 52
3.3 Determining pulse front tilt geometry 54
3.4 Benchtop THz source diagram 57
3.5 THz transport system 60
3.6 Diagram of ZnTe orientation for EOS 63
3.7 EOS characterization of THz source 66
3.8 Curved parallel plate waveguide (CPPWG) diagram 68
3.9 TE_{01} mode profile used for IFEL 68
3.10 Diagram of EOS setup used to characterize THz dispersion in the CPPWG . . . 71
3.11 EOS characterization of THz source 72
3.12 EOS measurements after THz propagation in CPPWG 74

3.13 CPPWG mode profiles for THz streaking 76
3.14 Photograph of the PCA device 78
3.15 Comparison of THz measurements using the PCA and EOS 79
3.16 PCA experiment setup 80
3.17 Diagram of the photoconductive antenna 80
3.18 PCA signal timing scan 82
3.19 PCA signal for varying beam charge 83
3.20 PCA signal for varying beam distance 83

4.1 IFEL resonance at 0.8 THz in free space vs. "zero-slippage" regime 86
4.2 Diagram of undulator Halbach array 88
4.3 Radia model of the undulator 89
4.4 Diagram of undulator cross section 90
4.5 Photograph of undulator tuning 91
4.6 Photograph of combined undulator-CPPWG apparatus 92
4.7 THz source and undulator setup on beamline 95
4.8 Photograph of CPPWG entrance and ZnTe for EOS measurements 96
4.9 Diagram of the PEGASUS beamline 99
4.10 Diagram of the THz IFEL experiment at PEGASUS 101
4.11 Photograph of CPPWG entrance with DRZ for beam position monitoring 102
4.12 Photograph of the PEGASUS beamline 103
4.13 3-D visualization of the streaking diagnostic 104
4.14 Examples of the beam energy distribution after THz IFEL interaction 106
4.15 Analysis of energy distribution slices after THz IFEL interaction 107
4.16 Timing scan of IFEL energy modulation 108

4.17 LPS simulation of the THz IFEL interaction 109
4.18 Measurements demonstrating the tunable IFEL resonance condition 111
4.19 Raw LPS images with THz off and THz on 113
4.20 Processing of raw LPS images to remove RF curvature 114
4.21 Frequency chirp in LPS image and dispersed THz profile 115
4.22 Example LPS image with irregular energy modulation 116
4.23 Scaling of the energy modulation as a function of THz energy 117
4.24 Raw LPS images with varying beam TOA 118
4.25 LPS image processing 119
4.26 Example images of short beam bunch compression 120
4.27 Distribution of short beam LPS measurements 122

5.1 Diagram of the beamline set up for the THz FEL experiment 126
5.2 GPT simulations using linac as bunching cavity 128
5.3 WAFFEL simulation of beam LPS in THz FEL experiment 129
5.4 Simulated output THz energy vs. input arrival time 130
5.5 Measurements of THz output energy vs. input arrival time 131
5.6 Measurements of THz output energy vs. beam charge 133
5.7 WAFFEL simulation of seeded THz FEL gain 136
5.8 WAFFEL simulation of seeded THz FEL gain without tapering 137
5.9 WAFFEL simulation of spontaneous superradiant THz FEL gain 139
5.10 Resonant energy and bucket height in the tapered undulator simulation 140
5.11 Simulated evolution of THz spectrum produced via spontaneous superradiance . 141

A.1 Rotation of index of refraction ellipse in ZnTe 146

LIST OF TABLES

2.1 Comparison of THz streaking schemes 40

3.1 CPPWG coupling efficiency for THz streaking 75

3.2 Parameters for the PCA-based beam timing experiment 81

4.1 Undulator magnet specifications 87

4.2 PEGASUS beam parameters 98

5.1 FEL Gain Simulations 142

ACKNOWLEDGMENTS

I'd like to begin by thanking my adviser Pietro Musumeci. From the projects and collaborations he has steered my way, to the conferences I have attended, I am immensely grateful for his dedication to ensuring every opportunity for success is available to me, and to all the students in his research group. I am still amazed to have stumbled into such a wonderful research environment. As it evolves through generations, PBPL maintains a balance of respect and irreverence that fosters both the drive for excellence in our research and also a ridiculously fun and welcoming sense of community. In the interest of brevity I should not name everyone, but really I would like to thank each and every member of PBPL, please know you have been greatly appreciated.

For teaching me the ropes, I want to thank Joe, Cheyne, Renkai, Oliver, Gerard, and especially Josh Moody, for laying the groundwork for the THz IFEL that became my thesis project, along with a big thank you to Kristin, Hoss, Evan, Sean, Long, and Kevin for welcoming me in, not just as a co-worker, but as a friend, when I was new in L.A. and had no idea what I was getting into. I want to thank my generation of Pietro's grad students, David, Nick, and Eylene, along with Claudio, Ryan, Ivan, DB and Jared for what have become wonderful, I hope lifelong, friendships. I've had so much fun these years, from PBPL BBQs and foosball tournaments, to D&D and musical gigs.

I want to thank Pietro's undergrads Siara, who helped me design and build the THz IFEL, and Junwen, who helped me run the THz FEL experiment, as well as Pietro's post docs Jared, for running PEGASUS with me on my first THz IFEL experiment, and Jorge and Xinglai, whom I've had the pleasure of collaborating with on the split ring resonator project. I'd also like to thank my collaborators outside of PBPL. Prof. Avraham Gover has been an invaluable source of knowledge on the "zero-slippage" technique and the design and theory of the waveguide IFEL. Thank you to Bryce Jacobson and Alex Murokh, for coming to me with the photoconductive antenna project, and to Tolga Yardimci and Prof. Mona Jarrahi, for contributing the plasmonics-enhanced PCA technology that has made it a success.

I'd like to thank Nickie Ng for all her help with my traveling logistics, and the UCLA Physical Sciences Division Machine shop, led by Harry Lockart, for making all the parts of the undulator, the waveguide, and numerous other pieces and modifications that were critical to the success of my project. I also want to thank both the U.S. DOE and NSF for supporting much of my research through grants DE-SC0009914 and PHY-1734215.

To my family and friends, thank you for showering me with love and support through the many years of my academic journey. Your enthusiasm for my work is contagious and always much appreciated.

Finally, to my husband, River, your unbridled confidence in me and my abilities leaves me humbled and filled with pride. As we have gone through this odyssey of physics graduate school together, you've seen the best and worst parts of me in both physics and life. Thank you for fielding my most cringe-worthy questions, being a party to my best breakthroughs, supporting me through each moment of doubt, and filling my life with joy every day.

VITA

2009–2012	Undergraduate Research Assistant, Physics Department, University of Chicago.
2012	B.A. in Physics (with Honors), University of Chicago
2013	M.S. in Physics, University of California, Los Angeles
2013-2014	Teaching Assistant, Physics and Astronomy Department, University of California, Los Angeles
2012-2018	Graduate Student Researcher under Pietro Musumeci, UCLA Particle Beam Physics Laboratory

PUBLICATIONS

M. Ave, M. Bohacova, E. Curry, P. Di Carlo, C. Di Giulio, P. Facal San Luis, D. Gonzales et al. "Precise measurement of the absolute fluorescence yield of the 337 nm band in atmospheric gases." *Astroparticle Physics*, 42 (2013): 90-102.

E. Curry, P. Musumeci, J. Moody, and J. Duris. "THz-based phase-space manipulation of electron bunches." *In AIP Conference Proceedings*, vol. 1777, no. 1, p. 080003. AIP Publishing, 2016.

E. Curry, A. Gover, S. Fabbri, and P. Musumeci. "THz Based Phase-Space Manipulation in a Guided IFEL." *In FEL 2015 Conference Proceedings*, (2015): TUP069.

E. Curry, B. Jacobson, A. Murokh, and P. Musumeci. "Sub-picosecond shot-to-shot electron

beam and laser timing using a photoconductive THz antenna." *In 4th International Beam Instrumentation Conference (IBIC2015)*, Melbourne, Australia, 13-17 September 2015, pp. 243-245. JACOW, Geneva, Switzerland, 2016.

E. Curry, S. Fabbri, P. Musumeci, and A. Gover. "THz-driven zero-slippage IFEL scheme for phase space manipulation." *New Journal of Physics*, 18, no. 11 (2016): 113045.

E. Curry, B. Jacobson, M. Jarrahi, P. Musumeci, and N. Yardimci. "Synchronization of ps Electron Bunches and fs Laser Pulses Using a Plasmonics-Enhanced Large-Area Photoconductive Detector." *In 5th Int. Beam Instrumentation Conf. (IBIC'16)*, Barcelona, Spain, Sept. 13-18, 2016, pp. 775-778. JACOW, Geneva, Switzerland, 2017.

E. Curry, S. Fabbri, P. Musumeci, and A. Gover. "Simulation of 3-D effects in THz-based phase space manipulation." *Nuclear Instruments and Methods in Physics Research Section A: Accelerators, Spectrometers, Detectors and Associated Equipment*, 865 (2017): 67-70.

E. Curry, S. Fabbri, J. Maxson, P. Musumeci, and A. Gover. "Meter-scale terahertz-driven acceleration of a relativistic beam." *Physical review letters*, 120, no. 9 (2018): 094801.

E. C. Snively, N. T. Yardimci, B. T. Jacobson, M. Jarrahi, P. Musumeci, and A. Murokh. "Non-invasive low charge electron beam time-of-arrival diagnostic using a plasmonics-enhanced photoconductive antenna." *Accepted to Applied Physics Letters*, (2018).

E. C. Snively, J. Xiong, P. Musumeci, and A. Gover. "Broadband THz Amplification and Superradiant Spontaneous Emission in a Guided FEL." *Under review at Optica*, (2018).

*Last name changed to Snively from Curry in 2018

CHAPTER 1

Introduction

Particle accelerators are a formidable tool in the arsenal of scientific discovery. On the most expansive scale, they give us the ability to find new particles and verify theories like the Standard Model of particle physics, bolstering our knowledge of fundamental physics and inspiring humanity with greater understanding of our universe. That enhancement of knowledge is complemented at the microscopic scale, with accelerators enabling the study of materials and dynamical processes at the atomic level, providing insight into structural biology and chemistry. Just as impressively, the influence of accelerator technology reaches, often unseen, into our everyday lives, from the extremely personal level, with medical diagnostics and treatment, to the societal level with industrial applications and security imaging.

Accelerator technology has flourished in the radiofrequency (RF) regime. Around the world, the infrastructure of modern accelerator facilities has been built upon robust, reliable RF technology, which remains largely unchanged from its original form [1]. There are many paths forward now as the accelerator physics community seeks to push the peak attainable beam energy and the efficiency of interaction beyond our current capabilities. There is extensive research on improving RF technology, including superconducting RF cavities [2] and innovative normal conducting RF structures [3], and a massive body of work is dedicated to plasma based acceleration [4], with wakefields driven by lasers [5] and wakefields driven by beams [6]. There is also a diverse field of research dedicated to novel structures and coupling schemes [7].

Hand in hand with these efforts is ongoing research into driving acceleration with electromagnetic fields in higher ranges of the frequency spectrum. The interest in acceleration schemes using higher frequencies is in large part the result of one of the key limitations

on current RF accelerator technology, which consists of the breakdown within structures operating above a certain threshold of accelerating field. From the empirical scaling of this breakdown threshold, $\propto f^{1/2}$ [8], it is clear that a higher breakdown threshold is attainable at higher frequencies. In addition to sustaining larger gradient fields, moving to higher frequencies allows energy manipulation at shorter length scales, making advantageous properties, like shorter bunch lengths, more easily attainable.

The substantial energy density available from contemporary laser technology has promoted a wide range of laser-driven acceleration schemes in today's field of advanced accelerator research. To harness higher frequencies for acceleration, alternative structures or coupling techniques must be implemented. A structure-based acceleration technique operating at laser frequencies cannot be obtained by simply re-scaling the components of RF-driven structures. Instead, non-conventional machining techniques and specialized materials are necessary to reach the length scales and damage thresholds required.

A prominent example of this groundbreaking technology is the fused silica dielectric laser accelerator (DLA) developed by the Accelerator on a Chip International Program (ACHIP). The high frequency driving field and novel nanofabricated structures have enabled record-high (GeV/m) accelerating gradients [9], but they also place stringent requirements on the electron beam emittance and control of both spatial alignment and timing. Only a small fraction of those electrons making it through the structure aperture are injected at a phase resulting in energy gain, while others fall outside of the temporal acceptance window to interact at a phase inducing beam energy loss.

1.1 Inverse Free Electron Laser acceleration

The work presented in this dissertation falls into another category of laser-driven acceleration, the Inverse Free Electron Laser (IFEL), which can circumvent the problem of breakdown entirely. This technique uses ponderomotive coupling from the combined effects of a periodic magnetostatic undulator field and an electromagnetic wave to exchange energy between the laser and the electron beam. The only structure required for the conventional IFEL process

is the source of the magnetic field, typically a periodic array of undulator magnets which acts on the beam as a far field process, leaving no fundamental breakdown limitation for the electromagnetic field of the laser.

The IFEL, proposed by Palmer in 1972 [10], is the inverse process of the energy exchange in a Free Electron Laser (FEL), in which the beam is decelerated to radiate energy as a coherent light source. In both cases, the principle of the interaction requires a periodic magnetic field to give the beam a wiggling trajectory. This transverse motion enables energy exchange with the transverse electric field of a laser that is copropagating with the beam.

The FEL mechanism, originally conceived by John Madey in 1971 [11], uses a seed laser to modulate the beam energy in order to form a periodic density modulation, i.e. "microbunching", which allows the synchrotron radiation produced by the beamlets bending in the undulator field to add coherently, amplifying the initial laser. Taking advantage of concepts such as the Self-Amplified Spontaneous Emission (SASE) FEL [12], the so-called "FEL instability" can be tuned for operation as a coherent light source without any seed laser, ideal for frequencies not accessible with conventional bound-electron-based laser technology. Most notably, the SASE-FEL has enabled the development of coherent Xray sources with revolutionary capabilities [13].

In contrast to acceleration in a laser-driven dielectric structure, the laser-driven IFEL allows full beam transmission and is not limited by a structure damage threshold. However, side-by-side comparison of these techniques would be overreaching, given that much of the driving force behind DLA research is dominated by unique advantages, like its radically small footprint and potential for inexpensive mass production. Instead, we'll note that the two techniques share the disadvantage of small temporal acceptance window relative to beam size, as determined by the driving frequency. For the DLA, this is evident in the acceleration and deceleration of electrons at different injection phases within the transmitted beam. Similarly, for the IFEL, this effect produces the periodic energy modulation that results in "microbunching" at the laser wavelength.

1.1.1 Transverse ponderomotive vs. longitudinal coupling

To establish resonant IFEL interaction between the laser and the beam as it wiggles in the undulator, a phase velocity matching condition

$$\omega = (k_0 + k_u)\beta_z c. \tag{1.1}$$

is required, where ω and k_0 are the radiation frequency and wavenumber in free space, k_u is the wavenumber corresponding to an undulator period, $\lambda_u = \frac{2\pi}{k_u}$, and $\beta_z c$ is the longitudinal beam velocity. This allows the beam to slip backwards along the electromagnetic wave by one period (may also be an integer number of periods) as it progresses through one period of the undulator, maintaining a constant interaction phase, as we'll describe in more detail in Chapter 2.

Alternatively, in a longitudinal "slow-wave" (Cherenkov and Smith-Purcell [14, 15]) coupling scheme for exchanging energy between a laser and electron beam, the specialized structure, such as a dielectric or corrugated waveguide, which supports a mode of the electromagnetic wave with a longitudinal component to the field must have a periodicity satisfying, for particles traveling at velocity $c\beta_z$, the phase synchronism condition

$$\omega = k_z \beta_z c \tag{1.2}$$

for the selected mode. In the following discussion, we highlight the relevant results from a comparison of laser-to-beam coupling schemes compiled in Ref. [16].

For both IFEL and longitudinal coupling schemes, the fields driving the interaction are supported by a physical structure. The periodic magnetostatic field of the undulator decays exponentially with increasing distance from the magnets, and the slow radiation mode supported by the longitudinal structure decays exponentially with distance from the structure wall. In both cases, the need for a structure imposes a limitation on the device size in order to have a substantial field in the space occupied by the electron beam. However, as we will see, this distance is much larger for the undulator case, especially for ultrarelativistic parti-

cles, giving it significant advantages over the near field structures necessary for longitudinal coupling.

A useful point of comparison between the two coupling schemes is provided by the decay constant, $k_\perp$, that appears in the field description, i.e. proportional to $e^{-k_\perp x}$ where x is the distance away from the magnetic field source or slow wave structure wall. The decay constant, $k_\perp$, is determined by the geometry of the periodic field source or slow wave structure and by the interaction frequency. For the case of transverse ponderomotive coupling in an undulator, $k_\perp$ is equal to the undulator wavenumber k_u to satisfy the magnetostatic Laplace equation. In the case of longitudinal coupling with a TM mode, $k_\perp$ should satisfy the Helmholtz equation. The decay constants are then given by

$$k_\perp = \begin{cases} k_u \ , & \text{transverse coupling} \\ \left(k_z^2 - \frac{\omega^2}{c^2}\right)^{1/2} \ , & \text{longitudinal coupling.} \end{cases} \tag{1.3}$$

The decay constant establishes a transverse acceptance interaction range, inversely proportional to that parameter, in which there is strong coupling for beam-wave interaction. We can use the dispersion relations for phase synchronism in each case (Eqs. 1.1 and 1.2) to write this distance in terms of the beam Lorentz factor with normalization by the wavelength for both schemes. Defining the interaction range to be $\frac{1}{2k_\perp}$, we have

$$\frac{1}{2k_\perp} = \frac{\lambda}{4\pi} \begin{cases} \frac{\beta_z}{1-\beta_z} \ , & \text{transverse coupling} \\ \beta_z \gamma_z \ , & \text{longitudinal coupling.} \end{cases} \tag{1.4}$$

In the non-relativistic limit, the interaction ranges have equivalent magnitudes for both manipulation techniques, but as one approaches the highly relativistic limit the interaction range is proportional to $2\gamma_z^2$ for the transverse coupling technique and to γ_z for the longitudinal technique. This larger transverse acceptance of the interaction region is the main advantage of transverse ponderomotive coupling using an undulator magnetic field (commonly referred to as FEL or IFEL coupling) as compared to longitudinal "slow-wave" (Cherenkov and Smith-Purcell) coupling in a dielectric or corrugated waveguide structure.

This scaling is advantageous for beam transmission, making it substantially easier to propagate significant charge through the device when the wavelength of the driving field is shrunk by two or three orders of magnitude from conventional radiofrequency. The cross-section of the relativistic beam accelerated by the electromagnetic wave can be significantly larger in the undulator coupling case. Furthermore, because the electromagnetic wave exchanging energy with the beam remains far from the boundaries set by the undulator, for free space laser propagation there is no attenuation due to ohmic losses, improving the efficiency of the interaction, and no fundamental limit to the field strength imposed by breakdown in the device.

1.2 THz frequencies

The frequency range that corresponds to wavelengths two to three orders of magnitude smaller than conventional RF, but still larger than laser wavelengths, is the THz regime. Accelerating structures operating in the THz range (0.1-10 THz) still have a length scale large enough to retain advantages associated with RF structures, such as broad temporal acceptance windows and large structure apertures, but the higher frequency means such structures can sustain higher field gradients and provide a more efficient energy chirp for beam phase space manipulation or transverse deflection for longitudinal diagnostics.

In addition to these unique advantages for accelerator applications, the THz regime is also of particular relevance as an FEL application, as it falls outside the range of frequencies that can typically be generated by bound-electron-based laser sources, without a subsequent process of difference frequency mixing. The THz regime deserves an introduction of its own, as it has been significant for both the challenge of developing sources as well as the broad range of applications in which it has already proven invaluable, within only a few decades of research.

Until recently, the frequency range of 0.3-10 THz was referred to as the "THz gap" due to a dearth of powerful sources, but after decades of intensive research, a broad array of THz generation techniques have become available, from quantum cascade lasers, to THz vac-

uum electronics, to laser-driven and accelerator-based sources [17, 18]. These THz sources have been implemented in a wide range of applications across several fields of research, including high frequency communications, medical and security imaging, and nonlinear spectroscopy [18, 19].

State-of-the-art optical rectification techniques can produce picosecond-scale THz pulses with pulse energies on the order of tens of microjoules from a femtosecond laser source in a university laboratory setting [20]. These laser-driven sources, based on pulse-front-tilted optical rectification in lithium niobate [21] or optical rectification in large-area organic crystals [22], are of particular interest for accelerator applications because of the high peak fields attainable (now routinely on the order of 100 MV/m; peak demonstrated field of >3 GV/m [22]) and the inherent synchronization to the laser source which can be used for multiple processes like beam generation and subsequent pump-probe experiments.

With the advent of these intense laser-driven sources, THz-based accelerator projects have flourished, creating an active and exciting new field of research. Recent experiments have included applications such as a THz-driven linac [23], photoinjector [24], and transverse deflecting beam diagnostic [25, 26]. Some THz-driven structures have even been demonstrated as multi-functional, with experiments showing implementation as both accelerator and then diagnostic [27, 28]. While large accelerating and deflecting gradients have been achieved in these examples, a key constraint in each of these cases has arisen from the duration of interaction that can be achieved with the short THz pulse. Given the current limitations on available THz intensity, though drastically improved over the last few decades, a necessary goal for any THz-driven accelerator application is efficient coupling for energy exchange and, ideally, extendable interaction length.

The IFEL process provides a highly efficient method for energy exchange, making it an attractive candidate for utilizing today's THz sources. However, the IFEL scheme relies on the beam slipping backwards relative to the laser pulse. To have the net effect of the energy exchange add constructively over many periods of oscillation within the undulator, the beam must slip backwards relative to the electromagnetic wave by a phase difference of $2\pi n$, with integer multiple n, as it traverses a single undulator period, codified in the

resonance condition of Eq. 1.1. As a result, the duration of interaction is limited by the laser pulse length, which becomes a particularly serious problem for an IFEL driven by the short, intense THz pulse that is produced from a laser-driven source.

1.3 A "Zero-slippage" IFEL

The work described in this dissertation has focused on developing a method to harness these short, intense THz pulses for efficient beam phase space manipulation over an extended interaction using a novel modification of the IFEL mechanism to operate in a "zero-slippage" regime. This new IFEL technique uses a waveguide to control the dispersion of the THz pulse, with the energy exchange occurring not in free-space propagation within the undulator, but inside a waveguide nested between the parallel arrays of undulator magnets. The addition of the waveguide facilitates simultaneous phase and group velocity matching between the beam and guided THz pulse. The conventional phase matching required for IFEL interaction is modified only in that the laser wavenumber now reflects propagation inside the waveguide. The group velocity matching keeps the THz pulse envelope spatially overlapped with the beam, achieving meter-scale interaction.

In Figure 1.1, we show the dispersion curves governing the THz propagation for a plane wave in free space and in a waveguide, alongside the effective dispersion relation for the electron beam in the undulator, given by the phase velocity matching condition for IFEL resonance. Intersection points correspond to frequencies at which there is resonant interaction; tangential intersection indicates group velocity matching. While these curves are not drawn to scale in order to better illustrate the intersection points, they make it immediately clear that the "zero-slippage" regime enables resonant interaction over a range of frequencies, rather than the single frequency model of a typical free space IFEL interaction.

This broadband coupling represents a novel regime of IFEL operation, requiring new simulation tools, as we discuss in Chapter 2, and offering new benefits and applications. This effect improves the efficiency of energy extraction from a short laser pulse, because it makes a greater portion of the broad spectral content available for resonant interaction,

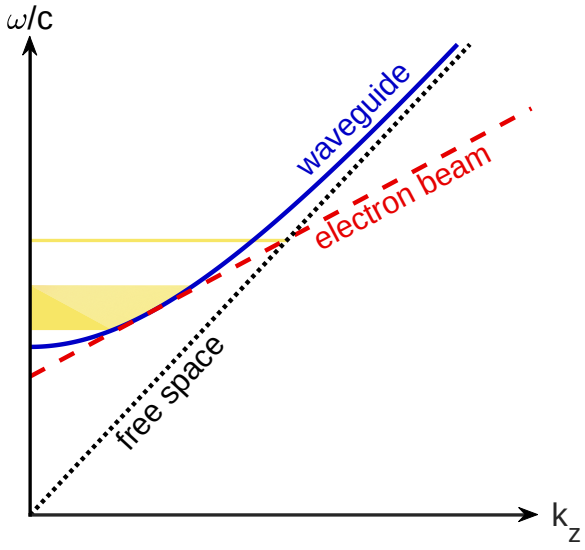

Figure 1.1: Dispersion curves for planar free-space (dotted black) and guided (solid blue) propagation. Intersection with the line corresponding to electron beam oscillation (dashed red) indicates resonant phase matching. The comparative bandwidth over which this can be achieved is highlighted in yellow for the two cases. Tangential intersection, i.e. having the same slope, indicates group velocity matching for a "zero-slippage" interaction.

a feature that is particularly relevant for interaction with the short THz pulses typically produced by laser-driven sources. The limited power available from current THz sources calls for highly efficient methods of interaction. Beyond the IFEL application of this technique, the broadband coupling enabled by "zero-slippage" operation also provides an attractive opportunity for FEL amplification and generation of broadband THz pulses, which we discuss in Chapter 5.

The concept of using a waveguide to match both group and phase velocity within an FEL was first discussed by Yu et al. in 1987 [29], and several studies have since been performed to explore an analytical model of the system [30, 31]. While the "zero-slippage" technique is a novel application of a waveguide-modified IFEL, the use of a waveguide for the purpose of maintaining laser intensity during IFEL interaction is certainly not new. One of the earliest demonstrations of IFEL acceleration, performed at Brookhaven National Laboratory in 1993, used a sapphire waveguide to control the intensity of the CO_2 laser driving the interaction

[32]. While subsequent IFEL experiments at laser frequencies would go on to explore the diffraction limited regime [33] and achieve significant accelerating gradients via tapering of the undulator [34], the use of waveguides has remained a common feature in THz FEL systems.

There are many examples of THz FEL facilities around the world [35, 36, 37, 38, 39, 40] and numerous proposals for compact, and even table-top scale, THz FEL sources [41, 42, 43]. In most of these cases a waveguide is used to control the diffraction of the THz pulse, confining the THz field over a longer interaction length. The THz-driven IFEL and FEL interactions discussed in this dissertation are unique among THz FELs in that the waveguide parameters were chosen not just to mitigate diffraction, but to allow operation in this novel "zero-slippage" regime. The improvement to interaction efficiency that comes from maintaining spatial overlap between the electron beam and short THz pulse is key to the success of this experiment which efficiently used a THz source with just up to 1 μJ pulse energy, making it the only demonstration of a THz-driven IFEL to date.

This dissertation includes proof-of-principle results from a series of "zero-slippage" IFEL and FEL experiments performed on the PEGASUS beamline at UCLA. The undulator and waveguide apparatus were designed for compatibility with the PEGASUS beamline parameters and fabricated at UCLA's Physical Sciences Machine Shop. The THz pulse driving the IFEL interaction was produced by pulse-front-tilted optical rectification of an 800 nm Ti:Sapphire laser pulse with $\sim 0.1\%$ conversion efficiency. The initial 2.5 mJ IR laser pulse was split, with the majority of the pulse energy dedicated to the THz source. The remaining IR pulse was converted into UV and used to generate electron bunches from the 1.6 cell S-band photogun installed on PEGASUS [44].

Initial results, discussed in Chapter 4, include the demonstration of a tunable IFEL resonance condition, based on a dynamically adjustable waveguide aperture, over a range of beam energies (5-8 MeV). The technique was then employed for the applications of beam timestamping and bunch length compression. Full longitudinal phase space measurements of the beam provided valuable insight into the interaction process, beam parameters, and diagnostic capabilities, informing subsequent measurements. A second round of tests centered

on the THz output energy after "zero-slippage" interaction. Measurements of the output THz pulse showed evidence of both stimulated emission and a novel regime of spontaneous superradiant emission, due to the short bunch length ($<$ 200 fs rms) relative to resonant THz frequency (0.8 THz).

1.4 Outline of this dissertation

The content of this dissertation is as follows. In the subsequent chapter, we introduce a simple 1-D analytical model for an IFEL and then extend our discussion to the "zero-slippage" regime of IFEL interaction. We then formalize the equations used to determine the charged particle phase space and THz field evolution in our newly developed multi-frequency FEL code named WAFFEL. We also briefly review our investigation into a THz-driven streaking diagnostic based on the "zero-slippage" technique. In Chapter 3, we discuss THz generation schemes and detection methods, with a focus on the techniques used over the course of experiments at UCLA. In Chapter 4, we review the experimental setup at PEGASUS and present the results of our first proof-of-principle experiment demonstrating beam phase space manipulation in a "zero-slippage" IFEL. In Chapter 5, we discuss our THz FEL experiment and present measurements of the THz output pulse after "zero-slippage" FEL interaction. We then explore the new characteristics and capabilities of a THz FEL operating in the "zero-slippage" regime using simulations of both THz generation and amplification. Finally, in Chapter 6, we summarize the results of this body of work and discuss the outlook of the "zero-slippage" technique for future IFEL and FEL applications.

CHAPTER 2

The "Zero-Slippage" Inverse Free Electron Laser

In this chapter, we lay down the theoretical framework used to guide our experimental study of the "zero-slippage" IFEL regime. We'll also discuss how we translate our simple analytical model of the interaction into a simulation with multi-particle dynamics, able to model the unique properties of a broadband "zero-slippage" interaction. The inverse free electron laser (IFEL) is a well-established form of laser-driven beam manipulation with a wealth of research [33, 34, 45, 46, 47] upon which to build when designing a new IFEL experiment. In the following sections, we discuss the interaction in terms of a simple 1-D model; for a more thorough discussion of the transverse particle dynamics we point the reader to Ref. [48].

2.1 IFEL Theory

To introduce the principles of free electron laser (FEL) interaction, we consider a 1-dimensional description of the dynamics for an electron copropagating with a laser in a planar undulator field, as illustrated in Fig. 2.1. The goal is to model the evolution of the electron energy in the presence of the combined undulator and laser fields and determine what conditions are necessary for that energy exchange to add constructively.

To good approximation, the undulator field in the vicinity of the electron beam can be described by

$$\mathbf{B}_{und} = B_u \sin(k_u z)\hat{\mathbf{y}} \tag{2.1}$$

for an undulator with period $\lambda_u = 2\pi/k_u$, and peak on-axis magnetic field B_u. To drive the energy modulation in this planar undulator, we use a laser with linear polarization that is parallel to the direction of beam wiggle, so perpendicular to the undulator field. We model

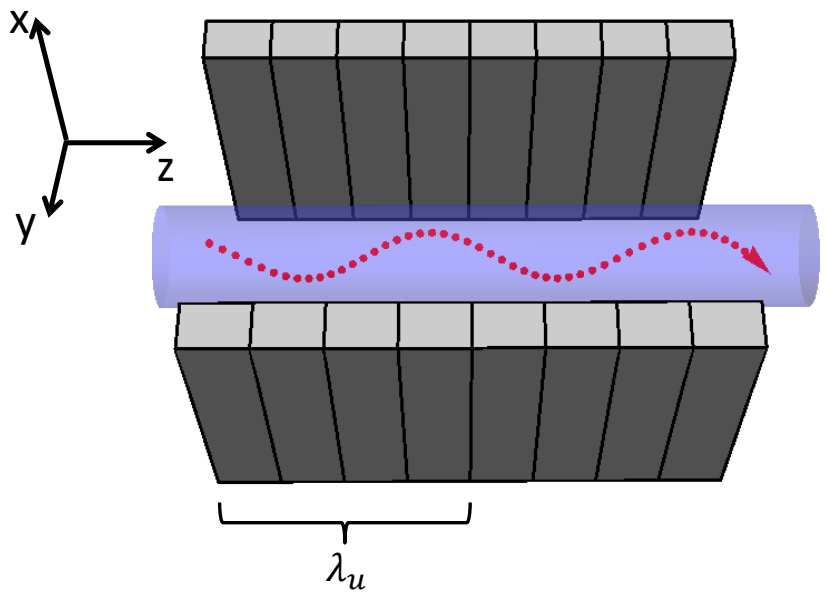

Figure 2.1: The undulator magnet arrays produce a static magnetic field pointing in the y-direction with sign and magnitude that varies sinusoidally along the beamline axis. This field causes the electron beam trajectory (dotted red line) to bend back and forth in the x-z plane while spatially and temporally overlapped with the laser field (transparent blue). One undulator period, λ_u, is four magnets long.

the laser using a plane wave with electric field written as

$$\mathbf{E}_{laser} = E_0 \sin(k_0 z - \omega t)\hat{\mathbf{x}} \tag{2.2}$$

with peak amplitude E_0, frequency ω, and wavenumber k_0 for propagation in free space.

The Lorentz force on an electron in this system, in terms of its four-momentum is

$$\left(\frac{d(\gamma mc^2)}{dt}, \frac{d(\gamma m\mathbf{v})}{dt}\right) = \Big(- e\mathbf{E}_{laser} \cdot \mathbf{v}, -e\left(\mathbf{E}_{laser} + \mathbf{v} \times (\mathbf{B}_{laser} + \mathbf{B}_{und})\right) \Big). \tag{2.3}$$

The magnitude of the normalized vector potential of the undulator, $K = \frac{eB_u}{k_u mc}$, also called the undulator parameter, is generally much larger than the normalized vector potential of the laser field, $K_{laser} = \frac{eE_0}{k_0 mc^2}$, and so we can neglect the contribution of the laser field in determining the electron motion. The transverse velocity of the electron dictated by this undulator field is

$$v_x = -\frac{cK}{\gamma}\cos(k_u z) \tag{2.4}$$

given that $v_z \approx c$.

Substituting Eqs. 2.2 and 2.4 into the scalar component of Eq. 2.3, we can determine the evolution of the particle energy, beginning from

$$mc^2\frac{d\gamma}{dt} = -e(E_0 \sin(k_0 z - \omega t))(-\frac{cK}{\gamma}\cos(k_u z)) \tag{2.5}$$

$$mc^2\frac{d\gamma}{dz}v_z = \frac{ecE_0 K}{\gamma}\sin(k_0 z - \omega t)\cos(k_u z) \tag{2.6}$$

and using the definition of K_{laser}, and once again $v_z \approx c$, to simplify the expression to

$$\frac{d\gamma}{dz} = \frac{k_0 K_{laser} K}{\gamma}\sin(k_0 z - \omega t)\cos(k_u z). \tag{2.7}$$

To understand the conditions under which this force results in a net effect on the electron's energy, it is useful to separate the expression on the right side of Eq. 2.7 into slow and fast oscillating terms,

$$\frac{d\gamma}{dz} = \frac{k_0 K_{laser} K}{2\gamma}\Big(\underbrace{\sin(k_0 z - \omega t + k_u z)}_{\text{slow}} + \underbrace{\sin(k_0 z - \omega t - k_u z)}_{\text{fast}} \Big) \tag{2.8}$$

Looking at the rate of change in phase, $\theta = k_0 z - \omega t + k_u z$, for the slowly oscillating term

$$\frac{d\theta}{dt} = (k_0 + k_u)\beta_z c - \omega \tag{2.9}$$

we see that, for net energy change to occur, this derivative can be set to 0 such that the phase of the interaction, or alternatively the sign and magnitude of the energy exchange term, remains constant, giving us the resonance condition (Eq. 1.1 from the Introduction)

$$\omega = (k_0 + k_u)\beta_z c. \tag{2.10}$$

As for the quickly oscillating term, by solving for k_0 and plugging into the expression, it is clear that the corresponding phase changes at a rate approximately equal to $-2k_u c$, resulting in multiple oscillations over a single undulator period, averaging to no net effect.

The average of the longitudinal beam velocity is used when implementing the resonance condition (Eq. 2.10) to establish the stationary phase. In practice, the longitudinal velocity varies due to the oscillations in the transverse velocity, since $\beta_0^2 = \beta_z^2 + \beta_x^2$. From Eq. 2.4, we can calculate the actual longitudinal beam velocity, v_z , as

$$v_z = c\sqrt{1 - \frac{1}{\gamma^2} - \frac{K^2}{\gamma^2}\cos^2(k_u z)} \tag{2.11}$$

with average

$$c\bar{\beta}_z \approx c\left(1 - \frac{1 + K^2/2}{2\gamma^2}\right). \tag{2.12}$$

Substituting Eq. 2.12 into Eq. 2.10, we determine the resonance condition in terms of the undulator parameters and the beam energy, γ. Starting from

$$\omega = (k_0 + k_u)c\left(1 - \frac{1 + K^2/2}{2\gamma_r^2}\right) \tag{2.13}$$

and using $k_u/k_0 << 1$ to simplify to

$$1 = \left(1 + \frac{k_u}{k_0}\right)\left(1 - \frac{1 + K^2/2}{2\gamma_r^2}\right) \approx 1 - \frac{1 + K^2/2}{2\gamma_r^2} + \frac{k_u}{k_0} \tag{2.14}$$

we have now established the resonant particle energy, $\gamma = \gamma_r$, and resonant wavelength of the laser, $\frac{2\pi}{k_0} = \lambda_r$, with

$$\frac{\lambda_r}{\lambda_u} = \frac{1 + K^2/2}{2\gamma_r^2}\ . \tag{2.15}$$

The preceding equations have governed the dynamics of a single particle navigating the IFEL potential. To move the discussion towards a description of the multi-particle dynamics of the full electron beam, it is useful to define a reference particle with stationary phase, Ψ_r (i.e. $\frac{d\Psi_r}{dt} = 0$), and resonant energy, γ_r. The value of Ψ_r determines the ponderomotive gradient of the system, since

$$\frac{d\gamma}{dz} = \frac{k_0 K_{laser} K}{2\gamma} \sin(\Psi_r) \tag{2.16}$$

where $\Psi_r = k_0 z - \omega t + k_u z$. For $\Psi_r = \pi/2$, $\frac{d\gamma}{dz}$ is maximized, producing acceleration, while for $\Psi_r = 0$ there is no net energy change of the resonant particle.

The actual ponderomotive gradient differs from this approximate relation due to the nonuniform longitudinal beam velocity by an amount quantified by the so-called coupling factor, $\mathrm{JJ} = J_0\left(\frac{K^2}{4+2K^2}\right) - J_1\left(\frac{K^2}{4+2K^2}\right)$, in terms of Bessel functions of the first kind, which modifies the effective coupling parameter such that, in Eq. 2.16, $K \to \mathrm{JJ}\, K$.

To determine the effect of the ponderomotive potential on the other particles in the electron beam, we define their energy and phase relative to the "resonant particle," using the normalized electron energy

$$\eta = \frac{\gamma - \gamma_r}{\gamma_r} \, . \tag{2.17}$$

Because $\frac{d\eta}{dz} = \frac{1}{\gamma_r}\frac{d\gamma}{dz}$, the change in particle energy is then described by

$$\frac{d\eta}{dz} = \frac{k_0 K_{laser} K \mathrm{JJ}}{2\gamma\gamma_r} \sin(\theta) \tag{2.18}$$

in which the coefficients can be gathered into a single parameter $\epsilon = \frac{k_0 K_{laser} K \mathrm{JJ}}{2\gamma_r^2}$, since $\gamma \approx \gamma_r$.

For the change in phase,

$$\frac{d\theta}{dt} = (k_0 + k_u)\beta_z c - \omega = c k_0 \left(1 + \frac{k_u}{k_0}\right)\left(1 - \frac{1 + K^2/2}{2\gamma^2}\right) - \omega \tag{2.19}$$

and given that $\frac{k_u}{k_0} << 1$, this simplifies to

$$\frac{d\theta}{dt} = c k_0 \left(-\frac{1 + K^2/2}{2\gamma^2} + \frac{k_u}{k_0}\right) \, . \tag{2.20}$$

From Eq. 2.15, we know

$$\gamma_r^2 = \frac{k_0}{k_u}\frac{1+K^2/2}{2} \tag{2.21}$$

which means

$$\frac{d\theta}{dt} = ck_0\left(-\frac{k_u}{k_0\gamma^2}\gamma_r^2 + \frac{k_u}{k_0}\right) = ck_u\left(1-\frac{\gamma_r^2}{\gamma^2}\right) \ . \tag{2.22}$$

Using the definition of η and the fact that $\eta << 1$, we have

$$\left(1-\frac{\gamma_r^2}{\gamma^2}\right) = 1-\Big[(1+\eta)^{-2}\Big] \approx 1-\Big[1-2\eta\Big] \ . \tag{2.23}$$

The resulting, simplified equations of motion are

$$\frac{d\eta}{dz} = \epsilon\sin\theta \tag{2.24}$$

$$\frac{d\theta}{dz} = 2k_u\eta \tag{2.25}$$

These equations have the form of a physical pendulum, corresponding to a Hamiltonian, $H = k_u\eta^2 + \epsilon\cos\theta$. From this framework, we can see that the ponderomotive potential resulting from the combined effects of the undulator and laser fields, produces regions of bound motion in the beam phase space, with particle trajectories rotating about the fixed point of the reference particle with stationary phase.

This phase space, referred to as longitudinal phase space (LPS), is just a part of the full beam phase space which consists of the 6 components corresponding to the 3-dimensional position and momentum of each particle in the beam distribution, (x, p_x, y, p_y, z, p_z) [49, 50]. Typically the LPS momentum component is defined as the particles' energy, and the position may be written with a distinct variable that indicates it is the particles' position along the beam trajectory or position relative to the bunch centroid, as we have done with (θ, η).

We describe these particles undergoing stable motion as "trapped" inside the ponderomotive bucket that is defined by the separatrix ($H = \epsilon$), as illustrated in Fig. 2.2. The diagram in Fig. 2.2 depicts the rotating trajectories, a.k.a. synchrotron oscillations, of example particles beginning with a range of phases at the resonant energy. In practice, the bucket height, $\eta_{max} = \sqrt{\frac{2\epsilon}{k_u}}$, determines the beam energy acceptance range, with particles

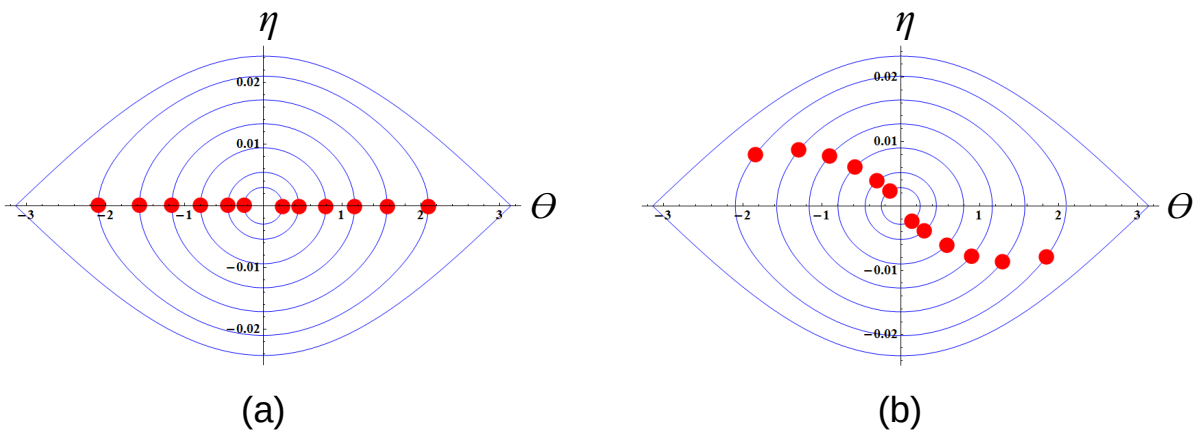

Figure 2.2: (a) Particles injected into the potential well at the resonant energy, but with different initial phases (b) then rotate about the stationary phase under the influence of the ponderomotive force, beginning the process of synchrotron oscillations within the bucket. The normalized electron energy is plotted on the y-axis; the relative phase, in units of $\lambda/2\pi$, is plotted on the x-axis.

outside of the separatrix executing unbound motion and becoming "detrapped." The bucket has an actual length in the z-coordinate of $\frac{2\pi}{k_z+k_u}$, and forms part of a sequence of ponderomotive buckets that repeats periodically. In a typical IFEL, operating at laser frequencies, the beam is broken up into these buckets, producing "microbunching," but a THz IFEL, with its comparatively long bucket, offers the possibility of total bunch capture, i.e. the short beam is trapped in a single bucket.

One of the goals of our THz IFEL project was to use this feature of the THz wave to efficiently compress the full beam. That is, to fit the entire beam near the resonant phase ($|\theta| < \pi/2$) so that it acquired a near-linear energy chirp which would then compress the beam due to velocity bunching. Fundamentally, the THz wave can induce this energy chirp more efficiently than a lower frequency wave, because a smaller field amplitude is required to achieve the same field gradient near the zero-crossing of the waveform. At higher frequencies, it becomes prohibitively difficult to get the beam short enough to fit within the region of near-linear energy chirp. In the discussion of the THz IFEL experiment in Chapter 4, we present beam measurements demonstrating compression via the THz IFEL interaction.

Another potential application of the total bunch capture effect is to decrease the beam timing jitter that arises from the RF system used to accelerate the beam. The limited stability of accelerator drive sources produces an unavoidable jitter (of order tens to hundreds of fs, depending on the size and scale of the machine) in the timing of electron beams [51, 52, 53, 54]. If the timing jitter is sufficiently small so that the beam arrives outside of the temporal acceptance window of the bucket, it is clear from Fig. 2.2 that an electron bunch arriving late relative to the resonant phase, that is $\theta < 0$, will be accelerated, while an early bunch ($\theta > 0$) will be decelerated. Over the course of a drift period, their adjusted velocities will then bring them closer to the ideal "reference" particle at $\theta = 0$.

The timing of the stationary phase is determined by the THz pulse, and if both the electron beam and THz pulse are generated using the same initial laser system, the timing of the THz pulse is synchronized with the ideal time of arrival (TOA) of the electron beam. Unfortunately we were not able to observe this effect during our measurements at PEGASUS, because the timing jitter was too large for the beam to consistently arrive within the same ponderomotive bucket.

2.1.1 A waveguide IFEL

Up to this point, our discussion of the IFEL dynamics has assumed the interaction takes place in free space. That is, the beam and laser are propagating in vacuum, far from any structure surface (the undulator magnets produce a far-field effect). Theoretically, there's no reason our intended THz IFEL interaction can't occur under this free space condition. In practice, however, the THz source available at UCLA to drive the IFEL interaction produces a short pulse which would interact with the beam for only a couple periods before the beam slippage would terminate the temporal overlap.

In the next section, we introduce a modification to the typical IFEL scheme in which a waveguide is added, as shown in Fig. 2.3, to slow the group velocity of the THz pulse in order to allow an extended interaction. The presence of the waveguide inherently limits the relevance of some of the free space advantages of IFEL operation, like the lack of laser

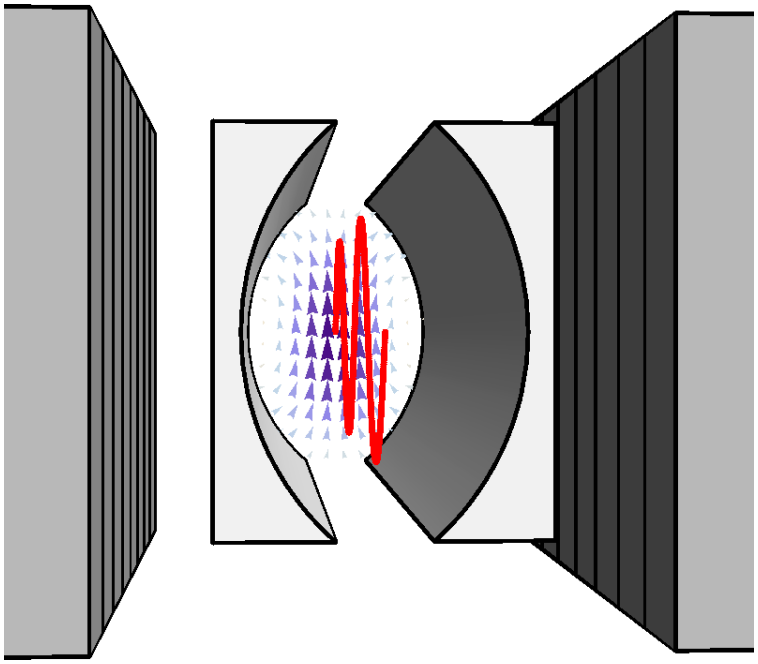

Figure 2.3: In the "zero-slippage" IFEL, the electron beam trajectory (red line) wiggles inside of the waveguide that is nested between the undulator magnet arrays. In this diagram, a curved parallel plate waveguide supports the TE_{01} mode (transverse profile shown with blue vector plot) of the THz pulse as it copropagates with the electron beam. This figure was reproduced from our publication, Ref. [55].

attenuation due to ohmic losses or a fundamental field limit due to breakdown. However, for operation in the THz frequency regime, suitable waveguide designs with cross-sections significantly larger than the radiation wavelength, on the order of a few-mm, still easily allow total beam transmission and minimize ohmic losses [56]. In addition, because the breakdown threshold in these structures typically increases for higher frequencies, all THz-driven accelerators retain an advantage over conventional RF-driven structures when it comes to sustaining high gradient (up to GV/m) fields.

An additional benefit of the waveguide is the preservation of the on-axis intensity of the electromagnetic wave, which removes the restriction on interaction length that is imposed by diffraction. In the THz frequency regime, this effect becomes particularly important, because the Rayleigh range scales inversely with wavelength. As a result, it is standard practice for FELs operating in the THz frequency regime to use a waveguide.

While propagating inside the waveguide, the longitudinal phase velocity, defined as $v_p = \omega/k_z$ for each frequency in the THz pulse, changes according to the wavenumber relation $k_0^2 = k_\perp^2 + k_z^2$. The dispersion curve is simply the modified longitudinal wavenumber, k_z, as a function of frequency, ω. The transverse wavenumber, $k_\perp$, that was zero in free space, such that $k_0 = k_z$, is now an eigenvalue of the wave equation satisfying the boundary conditions determined by the waveguide. Each solution to the eigenvalue problem defines a different mode in the waveguide. We use the low order TE_{01} mode of the curved parallel plate waveguide in our IFEL interaction, as illustrated in Fig. 2.3. The "TE" designates this mode as having only transverse electric field, i.e. $E_z = 0$ everywhere.

The group velocity of the THz pulse is controlled using the dispersion induced by the waveguide. This effect can be understood in terms of the dispersion curve, because the group velocity is just the slope of that curve, $v_g = \frac{\partial \omega}{\partial k_z}$. The phase and group velocity at each frequency is related according to $v_p v_g = (c/n)^2$ where n is the index of refraction in the medium, equal to 1 in vacuum, indicating that a reduced group velocity corresponds to a phase velocity greater than c.

By solving the FEL resonance condition in Eq. 2.10 for the axial wavenumber, we

establishes an effective dispersion relation indicating the conditions for resonant interaction. The expression in Eq. 2.10 was left in terms of the free-space wavenumber, k_0, to simplify subsequent calculations in free space, but to be more general this parameter should be the axial wavenumber, k_z (where $k_z = k_0$ in the free space case), making the resonance condition

$$\omega = (k_z + k_u)\bar{\beta}_z c \ , \tag{2.26}$$

with the "dispersion curve"

$$k_z = \frac{\omega}{\bar{\beta}_z c} - k_u \tag{2.27}$$

giving the axial wavenumber as a function of radiation frequency.

For a planar laser wave propagating in free space, i.e. $\omega = k_0 c$, both the phase velocity and the group velocity are c, meaning the dispersion curve is a straight line. Since the effective dispersion curve given by the IFEL resonance condition is also linear, there can only be a single frequency at which the dispersion curves intersect, indicating the frequency at which phase velocity matching can occur in free space. In a waveguide the dispersion curve is nonlinear, so there may be two intersections with the linear IFEL resonance curve, or there may be a tangential intersection. This is the "zero-slippage" condition that we seek to exploit, where the slope of the THz dispersion curve, i.e. the group velocity $\frac{\partial \omega}{\partial k_z}$, is equal to the slope of the resonance curve, corresponding to the average beam velocity $\bar{\beta}_z c$.

The two conditions for "zero-slippage" interaction, that is simultaneous phase velocity matching and group velocity matching, are

$$\omega = (k_z + k_u)\beta_z c \tag{2.28}$$

$$\frac{\partial \omega}{\partial k_z} = \beta_z c. \tag{2.29}$$

2.2 "Zero-Slippage" velocity matching

We discuss here the characteristics of ponderomotive coupling in the new "zero-slippage" IFEL operating regime. A key feature of the IFEL resonance condition established in Eq. 2.10 is slippage between the electron beam and laser. In free space propagation, the laser

inherently outruns the beam. The phase velocity matching condition requires that the beam slips backwards along the electromagnetic wave by one period, or an integer multiple of periods, as it advances through one undulator period. The length of the laser pulse then limits the duration of interaction, with very short pulses (few optical cycles long) maintaining effective coupling for only a few undulator periods. The use of a waveguide to match the group velocity of the laser pulse to the average longitudinal velocity of the electron beam can overcome this limitation for IFEL interaction driven by a short laser pulse.

For propagation in the waveguide, the axial laser wavenumber in Eq. 2.10 must be modified from the free space case, but the resonance condition itself remains essentially unchanged, as shown in Eq. 2.28. The beam still slips backwards relative to the electromagnetic wave by one period (or an integer multiple) for each undulator period, but the phase velocity of that wave is greater than c. This poses no obstacle, as the IFEL resonance condition already inherently assumes the laser phase velocity is greater than the beam velocity, with the phase synchronism supported by the wiggling trajectory in the undulator.

The term "zero-slippage" has been adopted to indicate that with group velocity matching, the beam does not slip backwards relative to the peak of the laser pulse envelope. Reference [29] began the discussion of simultaneous group and phase velocity matching in an FEL, operating in the millimeter range, for the purpose of eliminating the sideband instability, that is, amplification of frequency components away from the desired fundamental resonance which arises from slippage between the radiation and the beam. At the time, powerful coherent THz sources did not exist for driving the complementary process of IFEL acceleration. Subsequent studies of the "zero-slippage" interaction would highlight its potential benefits for broadband amplification [30, 31], still in the context of an FEL.

With the advent of intense, short, and therefore broadband, THz sources, that could potentially be used to drive beam manipulation, both the prolonged spatial overlap and the broadband coupling enabled by "zero-slippage" operation became crucial advantages for an IFEL interaction. With this technique, the length over which strong IFEL coupling persists can be extended to the meter scale and the energy stored in the broadband THz pulse is more effectively exchanged with the beam via multi-frequency coupling.

By definition, group velocity matching between the laser and electron beam propagation implies dispersion curves with the same slope. For simultaneous group and phase velocity matching we therefore have a tangential intersection between the dispersion relations for the laser propagating in the waveguide and the resonance condition for IFEL interaction. This effect was illustrated in Figure 1.1 of the Introduction, comparing the tangential intersection for "zero-slippage" IFEL interaction to the single-frequency intersection for the standard planar wave IFEL interaction in free space, as discussed in the section 2.1 of this chapter. However, the plot in Fig. 1.1 exaggerated the relative scales of the dispersion curves to more clearly illustrated the characteristics of the different intersections.

In Figure 2.4, we now examine the same phenomenon using realistic beam, undulator, and waveguide parameters for a THz pulse propagating in the TE_{01} mode of the waveguide. For a detailed description of the transverse mode and dispersion relation of the curved parallel plate waveguide (CPPWG) see Chapter 3. Figure 2.4 does not show the dispersion curves of the THz propagation and IFEL resonance, but rather the resonant beam energy required for interaction at a given frequency (x-axis) and waveguide aperture (color shading). By substituting the expression for the beam velocity (Eq. 2.12) into the resonance condition (Eq. 2.28) and solving for γ_r, we have

$$\gamma_r = \sqrt{\frac{k_z(1 + K^2/2)}{2(k_z - \omega/c + k_u)}} \tag{2.30}$$

where k_z is determined by the CPPWG spacing.

In practice, the electron beam will have a narrow energy spread, appearing like the "resonance" line in Fig. 2.4a. For a particular waveguide setting, we'll have a tangential intersection, indicating near-resonant interaction for that beam energy over a range of THz frequencies. Using the dashed black "resonance" line, we highlight the difference in interaction bandwidth for an 8 MeV beam. A single intersection point, at 1.33 THz, with the "free space" curve indicates resonance at one frequency, the tangential intersection near 0.7 THz indicates resonance over a range of frequencies for a plate spacing of 2.7 mm.

Figure 2.4a only utilizes the phase velocity matching condition. To see the corresponding group velocity mismatch ($c\bar{\beta}_z - \frac{\partial\omega}{\partial k}$), we look to Figure 2.4b, in which the waveguide value

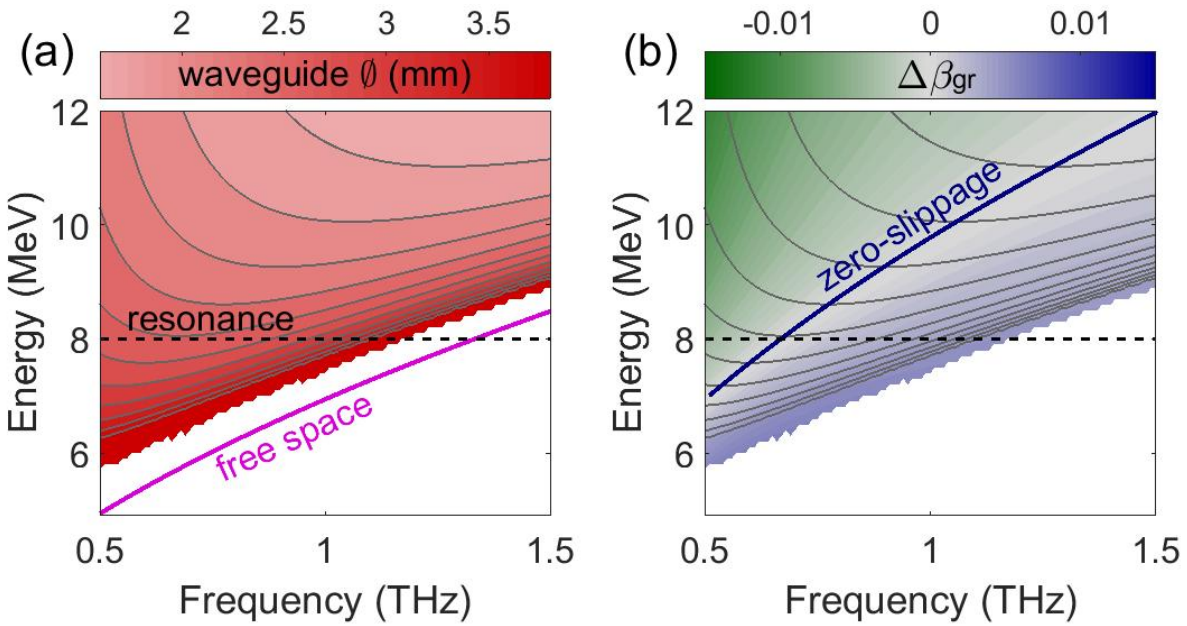

Figure 2.4: (a) Red shading indicates the curved parallel plate waveguide (CPPWG) aperture necessary to achieve resonant phase velocity matching for any given THz frequency and beam energy. The pink curve shows the correspondence required for resonant interaction with a planar wave in free space. (b) The shaded contour plot shows the group velocity mismatch between beam and THz pulse for any given THz frequency and beam energy, calculated using the corresponding waveguide aperture from (a). The "zero-slippage" curve highlights the set of frequencies and beam energies at which there is group velocity matching in addition to phase velocity matching.

depicted in (a) is used to calculate the group velocity mismatch at the given THz frequency and beam energy. Between these two plots, we see that while phase velocity matching can occur for many different combinations of beam energy and THz frequency, due to the flexibility added by the waveguide dispersion, only a single combination of beam energy and plate spacing will give us "zero-slippage" interaction at a particular frequency.

Although Figure 2.4 indicates that a range of frequencies are available for resonant interaction, in practice, the dispersion of the pulse effects the bandwidth of interaction and eventually limits the range of strong coupling. Other effects, like diffraction out of the gap between plates will also reduce the field. For a given combination of beam energy and waveguide spacing, there is only a single frequency at which both the resonant phase matching and group velocity matching are *exactly* satisfied. The bandwidth of neighboring frequencies that remain spatially overlapped with the short beam grows smaller as the initial near-single cycle pulse is dispersed into a frequency-chirped multicycle pulse. Given a long beam, the result is a frequency-chirped multicycle energy modulation as we will see in the experimental results shown in Chapter 4.

2.2.1 THz pulse description

For a more quantitative discussion of the effects of dispersion, we'll need to describe the electromagnetic field of the THz pulse. We define here a formula for the evolution of the THz pulse for propagation in a single mode, q. In practice, the total electromagnetic field can be decomposed into a sum of different modes, indexed by q. In Chapter 3, we will discuss in more detail the actual TE_{01} mode profile of the CPPWG used to control the THz pulse during IFEL interaction. Here, we'll use the assumption that the transverse profile of mode q is independent of frequency, as is the case for a smooth waveguide, like the curved parallel plate structure used in our experiments, to isolate the description of the transverse profile in a term, $\boldsymbol{\mathcal{E}}_{q\perp}(x, y)$, dependent only on the transverse coordinates.

The full description of the electric field propagating in mode q would then include this transverse term multiplied by a longitudinal, time-dependent component $\Psi(z, t)$ which can

be written as a Fourier integral in order to facilitate calculation of the frequency-dependent evolution of the spectral components.

$$\Psi(z,t) = \frac{1}{2\pi}\int_{-\infty}^{\infty} c_q(z,\omega)e^{ik_{zq}(\omega)z-i\omega t}d\omega \tag{2.31}$$

The initial Fourier coefficients, $c_q(0,\omega)$, are determined by the Fourier transform of the field at the entrance to the waveguide. For now we neglect the effects of energy exchange between electron beam and THz pulse, and assume no diffraction losses, such that the Fourier coefficients are equal to $c_q(0,\omega)$ for all z positions. This condition is called the frozen field approximation and will be used in our simulations of IFEL interaction. During the THz IFEL experiment, discussed in Chapter 4, the beam charge was kept low enough that the radiation absorbed/emitted by those electrons was negligible compared to the THz pulse energy.

We express the propagation wavenumber, k_{zq}, in mode q as an expansion around the peak frequency, ω_0, such that

$$k_{zq}(\omega) = k_{zq}(\omega_0) + \frac{\partial k_{zq}}{\partial\omega}\Big|_{\omega_0}(\omega-\omega_0) + \Delta k_{zq}(\omega,\omega_0) \tag{2.32}$$

where $\frac{\partial k_{zq}}{\partial\omega}\big|_{\omega_0}$ is the inverse of the group velocity, $1/v_g$, and $\Delta k_{zq}(\omega,\omega_0)$ represents terms of second order and higher in $\omega-\omega_0$. Inserting this expansion into Eq. (2.31) and factoring the ω-independent terms out of the integrand, we get an expression for the THz pulse in terms of a sinusoidal carrier wave modulated by a time-dependent envelope, that is

$$\Psi(z,t) \;=\; \underbrace{e^{ik_{zq}(\omega_0)z-i\omega_0 t}}_{\text{carrier wave}}\underbrace{\frac{1}{2\pi}\int_{-\infty}^{\infty} c_q(0,\omega)e^{-i(\omega-\omega_0)\left(t-\frac{z}{v_g}\right)+i\Delta k_{zq}(\omega,\omega_0)z}d\omega}_{\text{time-dependent envelope}}. \tag{2.33}$$

The carrier wave accumulates phase $k_{zq}(\omega_0)z$ and propagates with constant phase velocity $\omega_0/k_{z_q}(\omega_0)$. The full expression for the field, with the time-dependent envelope now referred to as $f_{\text{env}}(t-z/v_g)$, is

$$\mathbf{E}(\mathbf{r},t) \;=\; Re\left[\boldsymbol{\mathcal{E}}_{q\perp}(x,y)\Psi(z,t)\right] \;=\; Re\left[\boldsymbol{\mathcal{E}}_q(x,y)f_{\text{env}}(t-z/v_g)e^{ik_{zq}z-i\omega_0 t+i\phi_0}\right]. \tag{2.34}$$

When the THz pulse is group velocity matched to the beam, $t-z/v_g$ reduces to a time constant determined by the initial conditions. As a result, only the higher order terms in f_{env}

are time dependent. Looking at the bandwidth of frequencies over which the higher orders of the phase expansion can be neglected, as a function of interaction length L, provides insight into the broadband coupling enabled by "zero-slippage" interaction. A threshold value for phase mismatch, $\Delta\phi$, can be used to define the bandwidth of strong interaction using $\left|\Delta k_z(\omega,\omega_0)L\right| \ll \Delta\phi$. Assuming negligible contributions from third order and higher terms in the Taylor expansion, the range of frequencies that satisfies the condition is

$$\left|\omega-\omega_0\right| \ll \sqrt{\frac{2\Delta\phi}{DL}} \tag{2.35}$$

where D is the curvature parameter, $D=\frac{\partial^2 k_{z_q}}{\partial\omega^2}\Big|_{\omega_0}$.

In Figure 2.5, we use this formulation to compare "zero-slippage" interaction at two beam energies. By moving to a higher beam energy, we can dramatically increase the bandwidth of strong coupling, but in either case, the bandwidth diminishes as $1/\sqrt{L}$ with interaction distance. Using the interaction parameters from Fig. 2.5 as an example, for the high frequency case, $D=3.7\times10^{-7}$, and for the low frequency case, $D=1.6\times10^{-6}$, in units of $\frac{m}{rad\cdot c^2}$. If the acceptable range of phase mismatch is up to $\frac{\pi}{4}$, then after two undulator periods the interaction bandwidth defined by Eq. 2.35 would be 0.74 THz and 0.36 THz for each case, very large given the respective resonant frequencies of 1 THz and 0.5 THz.

The usefulness of this second order calculation is limited. For example, in Fig. 2.5a, the range of "strongly-coupled" frequencies extends out symmetrically around the resonant frequency. However, the asymptotic curves marking the beam energy and frequency correspondence (required for exact phase velocity matching at the two plate spacings) do not approach the beam energies (dashed lines) symmetrically, indicating the actual bandwidth of strong coupling will not be centered on the exact resonant frequency.

As the broad spectrum, near single-cycle THz pulse undergoes dispersion within the guide, the amplitude envelope becomes less sharply peaked. The decrease in local amplitude of the field driving energy exchange in Eq. 2.7 reduces the efficiency of the process, limiting, for example, the available chirping gradient for beam manipulation. Although dispersive pulse broadening degrades the long-term efficiency of energy exchange between laser and electron beam, a small silver-lining to this effect is that the group velocity matching condition

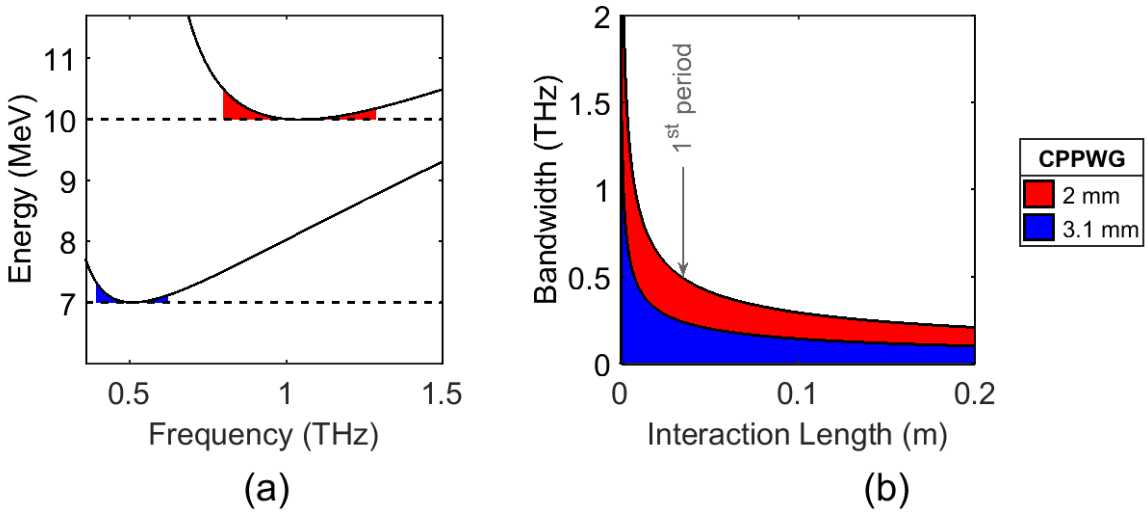

Figure 2.5: We examine two cases of "zero-slippage" interaction at beam energies of 7 MeV and 10 MeV, with corresponding CPPWG spacings of 3.1 mm and 2 mm, respectively. The solid curves in plot (a) highlight these two cases from the general contour plot in Fig. 2.4. To compare the broadband coupling, we use the two cases of beam energy and waveguide parameters in Eq. 2.35. The bandwidth of frequencies within which the phase slippage is less than 10° after the 1st period is shaded. In plot (b) we track how that bandwidth ($< 10°$ of slippage) decreases with interaction length. At the higher beam energy, the interaction bandwidth is effectively doubled.

is slightly relaxed. For a beam traveling with a small group velocity mismatch, the beam will not remain spatially overlapped with the peak of the THz envelope, but because of broadening of the envelope due to dispersion, the relative change in local amplitude will be less significant.

An alternative framework for understanding this effect is in terms of distortionless propagation. For a THz pulse composed of spectral content within the frequency range set by Eq. 2.35, such that the higher order terms are negligible, the envelope function becomes time-independent and the pulse travels without distortion. Within this limit, it would not be necessary to model dispersion of the THz pulse in an IFEL simulation. In practice however, the THz pulse spectrum produced by optical rectification generally includes a wide range of frequencies, as is the case for the THz source at UCLA discussed in Chapter 3. For simulations of meter-scale interaction, numerical integration is required to track the dispersion of the higher order terms in the time-dependent envelope description. We'll now move our discussion on to the simulation work we've performed for modeling a "zero-slippage" IFEL interaction.

2.3 "Zero-slippage" IFEL Simulations

Conventional FEL simulation tools like GENESIS are ill-suited to modeling the energy exchange in a "zero-slippage" interaction for several reasons. Primarily, the model must allow for coupling over a broad range of frequencies and characterize the evolution of that spectral content throughout the interaction. In addition, the propagation of the THz pulse must be determined by the dispersive properties of the waveguide.

Over the course of our studies, we relied on two primary means of simulating the "zero-slippage" interaction, developing our own 1-dimensional code in Matlab and implementing a custom element to describe the field in GPT. With our own simulation code, we were able to simulate non-negligible energy exchange between the THz pulse and the electron beam, but without 3-dimensional effects. With our custom element in GPT, we were able to describe the field of a multifrequency pulse undergoing dispersion in the CPPWG structure, allowing

us to simulate the 3-dimensional dynamics of the "zero-slippage" interaction, but only under the frozen field assumption.

After we benchmarked our 1-dimensional code against GPT, it became the foundation of our simulation studies on IFEL and FEL interaction, producing the simulation results presented in Chapters 4 and 5 alongside our experimental measurements. For both IFEL and FEL interactions, we used the TE_{01} mode in the curved parallel plate waveguide (CPPWG), which lends itself to a 1-D model. The electric field is nearly constant in magnitude with purely linear polarization within the range of maximum beam excursion, providing ideal spatial overlap for a beam undulating in the plane parallel to the plate surfaces.

In addition to IFEL and FEL interaction, we investigated one other application of the "zero-slippage" mechanism which did require the full 3-dimensional capabilities of GPT, that is a THz-driven transverse deflection technique for longitudinal beam diagnostics. In the final section of this chapter, we will discuss the analytical predictions for transverse deflection using higher order modes in the CPPWG which led us to explore this application more fully and our subsequent GPT simulation results, published in Ref. [57]. First, we'll describe our 1-dimensional simulation code, which we have named WAFFEL.

2.3.1 WAFFEL Simulation Code: Wide-bandwidth AmpliFication in a Free Electron Laser

The natural choice for developing a simulation tool to model the dispersion of a multifrequency pulse is to decompose the THz pulse into its Fourier components and track the evolution of the Fourier coefficients. In this respect our calculation is similar to several other multi-frequency FEL codes [58, 59], including MUFFIN [60], developed for SASE studies using a period averaged model with a focus on the coherent spontaneous emission due to a user-defined current profile.

By definition, the Fourier components quantifying the spectral content of the electromagnetic wave are determined by an integral with respect to time. In keeping with this formalism, the differential equations used in the simulation to describe the system must

evolve in terms of position along the undulator, rather than time. Our one-dimensional coordinate system then describes the temporal offset of each particle.

As in section 2.1, we restrict our calculation to the case of a planar undulator and neglect the effect of the laser field on the beam trajectory, i.e. the small-amplitude high frequency oscillations which average to zero relative to the wiggling induced by the undulator. The derivation presented here assumes a waveguide mode with linear polarization and uniform magnitude in the vicinity of the beam. Adaptation of our calculation for different undulator and waveguide configurations should be straightforward, but we have limited our current implementation to the CPPWG and planar undulator used in our proof-of-principle experiments.

2.3.1.1 Longitudinal Phase Space Evolution

We describe the electric field driving the IFEL interaction in terms of an integral over the frequency components

$$\mathbf{E} = \int \frac{d\omega}{2\pi} \boldsymbol{\mathcal{E}}_{q\perp}(x,y) c_q(z,\omega) e^{i(k_z(\omega)z - \omega t)} \hat{\mathbf{x}}. \tag{2.36}$$

In practice we simulate a discrete set of frequencies, with the integral in Eq. 2.36 becoming a sum over those spectral points.

Because the interaction takes place inside a waveguide, the effects of diffraction are minimized. While a 1-D model is sufficient to describe the waveguide-induced longitudinal dispersion, it may neglect key aspects of the interaction dynamics determined by the transverse mode profile in the waveguide, represented here by $\boldsymbol{\mathcal{E}}_{q\perp}(x,y)$. Because the TE_{01} mode used for IFEL interaction provides ideal spatial overlap with the beam, it can be reasonably described by a 1-D model, and so we set $\boldsymbol{\mathcal{E}}_{q\perp}(x,y)$ to one. In practice, the actual overlap with the e-beam will not be perfect and thus causes a small degradation of the coupling factor.

To implement Equation 2.7, describing the change in electron energy, we insert our new

description of the field (Eq. 2.36) with the sum over simulated spectral points

$$\frac{d\gamma_l}{dz} = -\frac{e}{mc^2}\sum_{\omega}\frac{\Delta\omega K q_l}{2\pi\beta_{z,l}\gamma_l} Re\left(c_q(z,\omega)e^{i(k_z(\omega)z-\omega t_l)}\right)\cos k_u z. \tag{2.37}$$

The simulation uses a set of macroparticles, indexed by l, initialized with a particle energy γ_l and temporal position t_l with a weighted charge $e\,q_l$. For the case of a single frequency simulation, the $\Delta\omega$ in equation (2.37) becomes that single frequency.

The evolution of the t_l positions is simply

$$\frac{dt_l}{dz} = \frac{1}{\beta_{l,z}c}, \tag{2.38}$$

where the longitudinal beam velocity, β_z, is given by Eq. 2.12.

The formulas used in the WAFFEL simulation code to determine the electron beam longitudinal phase space are equations (2.37) and (2.38). Numerical integration is performed with a built in Matlab ode solver using a variable steps size Runge-Kutta (4,5) algorithm based on the Dormand-Prince method [61]. The longitudinal wavenumber, k_z, for THz propagation is specified from the dispersion relation for the TE_{01} mode of the CPPWG defined in Ref. [62].

If we assume the beam has low charge, such that the frozen field approximation is applicable, then these equations are enough to predict the modulated phase space of the electron beam. This formulation accounts for multi-frequency coupling with the THz pulse defined by the Fourier coefficients, c_q, input by the user, along with the dispersion of that waveform, but assumes that the values of those Fourier coefficients do not change over the course of the interaction.

The more rigorous description of the evolution of the laser field calculates the change in the Fourier coefficients when there is appreciable energy exchange with the electron beam. This becomes essential for electron beams with more than a few 100 fC. At very high charge, the interaction pushes the boundary of where the slowly varying envelope approximation (SVEA) is a valid model of the energy exchange, suggesting the need for a calculation without the SVEA assumption. In practice, for the simulation studies performed during the course of this thesis work, simulation results determined with the SVEA option turned "on"

were consistent with results from simulations without the assumption, and so, primarily to save simulation time, the results presented in Chapters 4 and 5 use the SVEA condition.

2.3.1.2 Multifrequency Field Evolution

To calculate the laser field evolution, we begin from Maxwell's equations using the Lorenz gauge condition, where $\mathbf{E}$ and $\mathbf{B}$ have the form

$$\mathbf{E} = -\nabla\phi - \frac{\partial \mathbf{A}}{\partial t} \tag{2.39}$$

$$\mathbf{B} = \nabla \times \mathbf{A} \tag{2.40}$$

and we have the wave equations

$$\left(\nabla^2 - \frac{1}{c^2}\frac{\partial^2}{\partial t^2}\right)\mathbf{A} = -\mu_0 \mathbf{J} \tag{2.41}$$

$$\left(\nabla^2 - \frac{1}{c^2}\frac{\partial^2}{\partial t^2}\right)\phi = -\frac{\rho}{\epsilon_0}. \tag{2.42}$$

The goal now is to calculate the change in $\mathbf{A}$ as a function of the copropagating electron beam current $\mathbf{J}$. The vector potential describing the field in Eq. 2.36 has the form

$$\mathbf{A} = -\int \frac{d\omega}{2\pi}\boldsymbol{\mathcal{E}}_{q\perp}(x,y)\frac{ic_q(z,\omega)}{\omega}e^{i(k_z(\omega)z-\omega t)}\hat{\mathbf{x}}. \tag{2.43}$$

The left hand side of Eq. 2.41 becomes

$$-\int \frac{d\omega}{2\pi}\frac{i}{\omega}\boldsymbol{\mathcal{E}}_{q\perp}(x,y)\Big[c_q''(z,\omega) + 2ik_z(\omega)c_q'(z,\omega) - \left(k_x^2(\omega)+k_y^2(\omega)+k_z^2(\omega)\right)c_q(z,\omega) + \frac{\omega^2}{c^2}c_q(z,\omega)\Big]e^{i(k_z(\omega)z-\omega t)}\hat{\mathbf{x}}. \tag{2.44}$$

To show that $\frac{\partial^2 A_x}{\partial x^2} = -k_x^2 A_x$ and $\frac{\partial^2 A_x}{\partial y^2} = -k_y^2 A_x$ are a consequence of the transverse mode profile, we can look at the longitudinal magnetic field in the TE_{01} mode, which takes the form

$$H_z = Ae^{\pm ik_z z}\int_{-\infty}^{\infty} f(k_x)e^{ik_x x}\begin{pmatrix}\cos(k_y y)\\ \sin(k_y y)\end{pmatrix}dk_x \tag{2.45}$$

and substitute into the standard relations for propagation in a waveguide,

$$E_x = \frac{-i}{k_{mn}^2}\left(k_z\frac{\partial E_z}{\partial x} + \omega\mu_0\frac{\partial H_z}{\partial y}\right) \tag{2.46}$$

$$E_y = \frac{-i}{k_{mn}^2}\left(k_z\frac{\partial E_z}{\partial y} - \omega\mu_0\frac{\partial H_z}{\partial x}\right). \tag{2.47}$$

In Eq. 2.44, the terms proportional to $c_q(z,\omega)$ cancel and we will set $\boldsymbol{\mathcal{E}}_{q\perp}(x,y)$ to one for our 1-dimensional model, leaving

$$-\int \frac{d\omega}{2\pi}\frac{i}{\omega}\left(c_q''(z,\omega) + 2ik_z(\omega)c_q'(z,\omega)\right)e^{i(k_z(\omega)z-\omega t)}\hat{\mathbf{x}}. \tag{2.48}$$

We would like to compare Fourier components on either side of equation 2.41. To put the right hand side in terms of an integral over ω, we take the Fourier transform and inverse Fourier transform like so

$$-\mu_0\mathbf{J} = \int \frac{d\omega}{2\pi}\left(\int dt\,(-\mu_0\mathbf{J})\,e^{-i(k_z(\omega)z-\omega t)}\right)e^{i(k_z(\omega)z-\omega t)}. \tag{2.49}$$

Equating the Fourier coefficients from equations 2.48 and 2.49 we have

$$-\frac{i}{\omega}\left(c_q''(z,\omega) + 2ik_z(\omega)c_q'(z,\omega)\right) = \int dt\,(-\mu_0 J_x)\,e^{-i(k_z(\omega)z-\omega t)}. \tag{2.50}$$

The x-component of the current is defined as

$$J_x = \frac{-ec}{A_e}\sum_{l=1}^{N_p} q_l\delta(z-z_l)\beta_{l,x}. \tag{2.51}$$

For a calculation which evolves in z, rather than time, the delta function at the particles' location needs to be reformulated in terms of their time of arrival at a particular z position. J_x is then defined as

$$J_x = \frac{-ec}{A_e}\sum_{l=1}^{N_p} q_l\frac{\delta(t-t_l)}{\beta_{l,z}c}\beta_{l,x}. \tag{2.52}$$

Substituting this definition for J_x into the right hand side of equation 2.50 we have

$$-\frac{i}{\omega}\left(c_q''(z,\omega) + 2ik_z(\omega)c_q'(z,\omega)\right) = \int dt\frac{\mu_0 ec}{A_e}\sum_{l=1}^{N_p} q_l\frac{\delta(t-t_l)}{\beta_{l,z}c}\beta_{l,x}e^{-i(k_z(\omega)z-\omega t)}. \tag{2.53}$$

Applying the delta function we get

$$-\frac{i}{\omega}\left(c_q''(z,\omega)+2ik_z(\omega)c_q'(z,\omega)\right)=\frac{\mu_0 e}{A_e}\sum_{l=1}^{N_p}q_l\frac{\beta_{l,x}}{\beta_{l,z}}e^{-i(k_z(\omega)z-\omega t_l)}. \tag{2.54}$$

Substituting the form of β_x determined by Eq. 2.4, we have

$$-\frac{i}{\omega}\left(c_q''(z,\omega)+2ik_z(\omega)c_q'(z,\omega)\right)=\frac{\mu_0 eK}{A_e}\sum_{l=1}^{N_p}\frac{q_l}{\gamma_l\beta_{l,z}}\cos(k_u z)e^{-i(k_z(\omega)z-\omega t_l)}. \tag{2.55}$$

Including the frozen field approximation, WAFFEL offers three options for determining the field. To implement the full form of Eq. 2.55, we can include the second order derivative in Matlab by defining a system of equations

$$dc_q(z,\omega)=c_{qprime} \tag{2.56}$$

$$dc_{qprime}(z,\omega)=-2ik_z(\omega)c_{qprime}(z,\omega)+\frac{i\omega\mu_0 eK}{A_e}\sum_{l=1}^{N_p}\frac{q_l}{\gamma_l\beta_{l,z}}\cos(k_u z)e^{-i(k_z(\omega)z-\omega t_l)}. \tag{2.57}$$

Alternatively, under most operating conditions it is reasonable to assume that the second order derivative of c_q in Eq. 2.55 is negligible. In this case, we use

$$c_q'(z,\omega)=\frac{\omega\mu_0 eK}{2k_z(\omega)A_e}\sum_{l=1}^{N_p}\frac{q_l}{\gamma_l\beta_{l,z}}\cos(k_u z)e^{-i(k_z(\omega)z-\omega t_l)}. \tag{2.58}$$

to describe the evolution of the field.

WAFFEL also offers the optional inclusion of space charge effects, which become relevant when the beam has appreciable charge. The force due to space charge repulsion is determined by integrating the beam density along the z-axis. Parameters that change along the length of the undulator, namely tapering of the undulator parameter, K, are defined within a loop which breaks the simulation up into smaller steps, each with constant parameters.

2.4 THz-driven transverse deflection

Because transverse deflection using THz waves benefits from the same fundamental frequency scaling as first discussed for a THz-induced beam energy chirp (producing bunch length compression), streaking techniques aimed at developing a THz-driven longitudinal diagnostic

have generated a lot of interest, including a new wave of experiments demonstrating THz-based streaking [25, 26, 27, 28].

We have already seen that the addition of the waveguide to the IFEL interaction increases the flexibility of the resonance condition, but we can take that even a step further and change the type of interaction by changing the mode in the waveguide. Zholents and Zolotorev [63] first proposed using an odd waveguide mode to produce streaking in an undulator, sparking subsequent research by Andonian et al. ref. [64] into a CO_2 laser-driven longitudinal profile diagnostic. To see how an antisymmetric mode profile can produce beam deflection, we'll derive an analytical prediction for the altered transverse beam momentum, following closely our discussion in Ref. [55].

As with the calculation of IFEL energy exchange, we begin from the Lorentz force equation (Eq. 2.3), now focused on the transverse momentum

$$\frac{d\mathbf{p}_\perp}{dt} = -e\Big(\mathbf{E}_\perp(\mathbf{r},t) + v_{z0}\hat{\mathbf{e}}_z \times \mathbf{B}_\perp(\mathbf{r},t) + \mathbf{v}_\perp \times \hat{\mathbf{e}}_z \mathbf{B}_z(\mathbf{r},t)\Big). \tag{2.59}$$

We'll express the THz field in terms of the carrier wave and envelope, $f_{\text{env}}(t - z/v_g)$, as in Eq. 2.34, giving

$$\begin{aligned} \mathbf{E}(\mathbf{r},t) &= Re\left[\boldsymbol{\mathcal{E}}_q(x,y) f_{\text{env}}(t - z/v_g) e^{-i\omega_0 t + ik_{zq}z + i\phi_0}\right] \\ \mathbf{H}(\mathbf{r},t) &= Re\left[\boldsymbol{\mathcal{H}}_q(x,y) f_{\text{env}}(t - z/v_g) e^{-i\omega_0 t + ik_{zq}z + i\phi_0}\right] \ . \end{aligned} \tag{2.60}$$

The magnetic field profile in the waveguide is related to the electric field profile by

$$\hat{\mathbf{e}}_z \times \boldsymbol{\mathcal{B}}_{q\perp} = \frac{-\boldsymbol{\mathcal{E}}_{q\perp}}{c} \begin{cases} k_{zq}/k_0 \ , & \text{TE mode} \\ k_0/k_{zq} \ , & \text{TM mode.} \end{cases} \tag{2.61}$$

Depending on the mode profile we use, we can change the direction of deflection relative to the plane of the wiggling trajectory of the beam, as shown in Fig. 2.6. An antisymmetric mode profile produces deflection in the plane parallel to the beam wiggle, while a mode supporting a longitudinal magnetic field produces deflection perpendicular to the beam wiggle. For the parallel case, substituting the THz field expression into Eq. 2.59 gives us

$$\frac{d\mathbf{p}_x}{dt} = -e\alpha\, Re\left[\boldsymbol{\mathcal{E}}_q(x,y) f_{\text{env}}(t - z/v_g) e^{-i\omega_0 t + ik_{z0}z + i\phi_0}\right] \tag{2.62}$$

where

$$\alpha = \begin{cases} 1 - \beta_z \frac{k_{zq}}{k_0} & , \quad \text{TE mode} \\ 1 - \beta_z \frac{k_0}{k_{zq}} & , \quad \text{TM mode.} \end{cases} \tag{2.63}$$

Using the fact that $v_g v_p = c^2$, we know that $v_g = \frac{k_{zq}}{k_0} c$, indicating that only a TE mode can impart this parallel deflection while operating in the "zero-slippage" regime, in which $v_g \approx v_z$.

Near the beam axis, we can approximate the antisymmetric mode profile necessary for transverse deflection in the x-direction, using

$$\boldsymbol{\mathcal{E}}_q(x_e, y_e) \approx \hat{\mathbf{e}}_x \frac{\partial \mathcal{E}_{qx}}{\partial x}\Big|_0 x_e(t) = -\hat{\mathbf{e}}_x \mathcal{E}'_{qx} \frac{iKe^{-ik_u z}}{\beta_z \gamma k_u}. \tag{2.64}$$

Substituting this expression into Eq. 2.62, the change in p_x for the phase-synchronous term becomes

$$\frac{dp_x}{dt} = \frac{e\alpha K}{2\beta_z \gamma k_u} Re\left[i\mathcal{E}'_{qx} f_{\text{env}}(t - z/v_g) e^{-i\omega_0 t + ik_{zq} z - ik_u z + i\phi_0} \right]. \tag{2.65}$$

For an electron entering the wiggler on-axis with velocity v_z at initial time t_0, we can integrate with respect to time, using $z = v_z(t - t_0)$, to determine the final transverse momentum

$$p_x = \frac{e\alpha K}{2\beta_z \gamma k_u} Re\Big[\mathcal{E}'_{qx} e^{-i(\omega_0 t_0 - \phi_0 - \pi/2)} \int_0^{L/v_z} f_{\text{env}}\left(\left(1 - \frac{v_z}{v_g}\right) t + t_0 \right) e^{i((k_{z0} + k_u)v_z - \omega_0)t} dt \Big] \tag{2.66}$$

for an interaction length L. With the assumption $v_z \approx v_g$ for the zero-slippage case, the corresponding angular deflection is

$$\Delta\Theta_x = \frac{p_x}{mc\gamma\beta_z} = \frac{e\alpha K L\, \mathcal{E}'_{qx} f_{\text{env}}(t_0)}{2\beta_z^3 \gamma^2 mc^2 k_u} \text{sinc}\left(\frac{\theta L}{2}\right) \sin\left(\omega_0 t_0 - \phi_0 + \frac{\theta L}{2}\right) \tag{2.67}$$

where $\theta = \frac{\omega_0}{v_z} - (k_0 + k_u)$, very similar in form to [63].

By a similar method we can calculate the deflection in the plane perpendicular to the wiggling electron trajectory from the longitudinal coupling in the third term of Eq. (2.59). The resulting angular deflection

$$\Delta\Theta_y = \frac{eKL\, \mathcal{B}_{qz} f_{\text{env}}(t_0)}{2\beta_z^2 \gamma^2 mc} \text{sinc}\left(\tfrac{\theta L}{2}\right) \cos\left(\omega_0 t_0 - \phi_0 + \frac{\theta L}{2}\right) \tag{2.68}$$

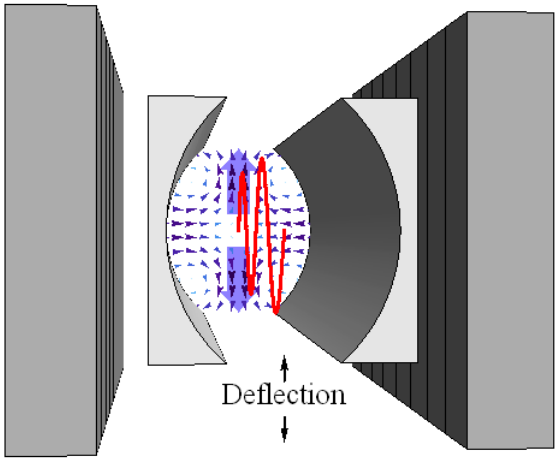

(a)

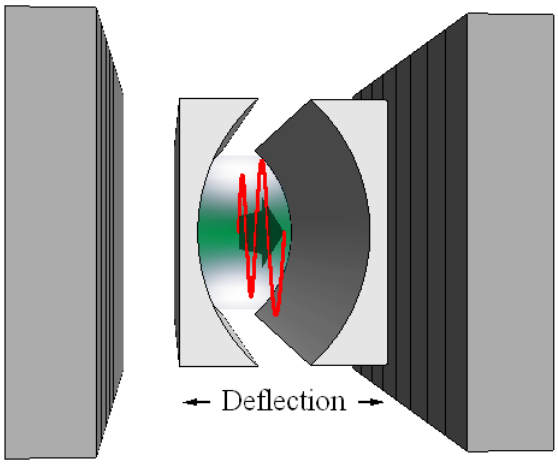

(b)

Figure 2.6: Representations of the streaking interaction using (a) the vertical electric field of the TE_{11} mode (transverse mode profile shown with blue arrows) and (b) the longitudinal magnetic field of the TE_{20} mode (field magnitude represented in green, with directional arrow). The wiggling trajectory of the electron beam (shown in red) is nested inside of the curved parallel plates of the waveguide structure, with the linear arrays of undulator magnets on either side. These figures are reproduced from our publication, Ref. [57].

is optimized for an on-axis B-field.

In Ref. [55], we used these analytical calculations of the angular deflection to predict the timing resolution that could be achieved using these THz-driven deflection schemes. The results are summarized in Table. 3.1

Table 2.1: Comparison of THz streaking schemes

	TE_{11} mode	**TE_{20} mode**
THz coupling efficiency	0.278	0.638
CPPWG spacing	2.65 mm	1.95 mm
Resonant energy	7.703 MeV	6.225 MeV
Angular deflection	3.3 mrad	7.9 mrad
Effective angular deflection	0.9 mrad	5.0 mrad
Timing resolution	30 fs	7 fs
(for $\epsilon_{n,x} = .1$ mm-mrad, $\sigma_x = 45\,,\mu$m)		

Assuming no position-angle correspondence in the initial beam distribution, the effective timing resolution is defined, for deflection in the x, or y, direction, as [64]

$$\Delta t = \frac{\epsilon_{n,\{x,y\}}}{\gamma\sigma_{\{x,y\}}\Delta\Theta_{\{x,y\},\max}ck_z} \tag{2.69}$$

where $\epsilon_{n,\{x,y\}}$ is the normalized emittance and $\sigma_{\{x,y\}}$ is the beam size. The emittance, ε, of the beam is proportional to the area occupied by the beam distribution in phase space by a factor of π, such that

$$\varepsilon = \sqrt{\langle x^2\rangle\langle x'^2\rangle - \langle xx'\rangle^2}\,. \tag{2.70}$$

The normalized emittance, $\varepsilon_n = \langle\beta\gamma\rangle\varepsilon$, is then independent of the beam energy.

The predicted fs-level temporal resolution is possible, despite only a few MV/m THz field, because the deflection mechanism scales with the wavelength of the modulating field. While an X-band deflector can already achieve fs resolution, as demonstrated at PEGASUS in Ref. [65], improvements like increasing the THz field strength or interaction length could push the THz-driven streaking scheme to sub-femtosecond resolution.

The calculations in Table 3.1 are based on optimized THz coupling schemes which we'll describe in more detail in Chapter 3. The low coupling efficiencies determined for this idealized hypothetical indicate that coupling may be a substantial obstacle when it comes to implementing this scheme in practice. In addition, while these predictions for the THz-induced deflection of the beam suggest an exciting new application of the "zero-slippage" interaction technique, we will see in our GPT simulations that the 3-dimensional effects of the undulator focusing can undermine the actual deflection.

2.4.1 GPT simulations of a THz-driven streaking diagnostic

The well-established General Particle Tracer (GPT) code provides a simulation platform in which we can model the full, 3-dimensional, charged particle dynamics in electromagnetic fields [66]. In order to use GPT to simulate interaction within a waveguide, we need to supply the code with a field map of the THz mode inside the CPPWG. This map must incorporate the effects of dispersion as the interaction progresses. By allowing the assumption of a frozen field, in which the energy exchange with the beam has negligible effect on the THz pulse energy, we can build a custom element using the GPT programming interface to describe the THz field.

We use the CPPWG mode functions calculated in Ref. [62] (see CPPWG section of Chapter 3) to define the field inside the waveguide, requiring the user to input the plate spacing, curvature, and length, along with the relevant mode numbers. We assume a Gaussian THz spectrum, with a user defined peak frequency, FWHM, and peak electric field on-axis. To simulate the broadband pulse, the user assigns a bandwidth and the number of discrete spectral points to include. The custom element then sums the field calculated for each frequency, with a normalization factor assigning the initial peak field on-axis. Once the element is given a position on the beamline, GPT simulates the 6-D phase space of a user-defined beam distribution as it travels down the beamline, through the field generated by the custom element.

To include the static magnetic field produced by the undulator in our simulation, we

import the 3-D field map generated during the design stage of the undulator. We began this chapter with the approximation that the magnetic field of the undulator was described by a purely horizontal sinusoidal field (Eq. 2.1), but clearly this cannot be true since the field would have non-zero divergence, violating Maxwell's equations. In reality, the magnetic field of the undulator produces a focusing effect leading to betatron oscillations, as illustrated by the simulated particle trajectories in Fig. 2.7.

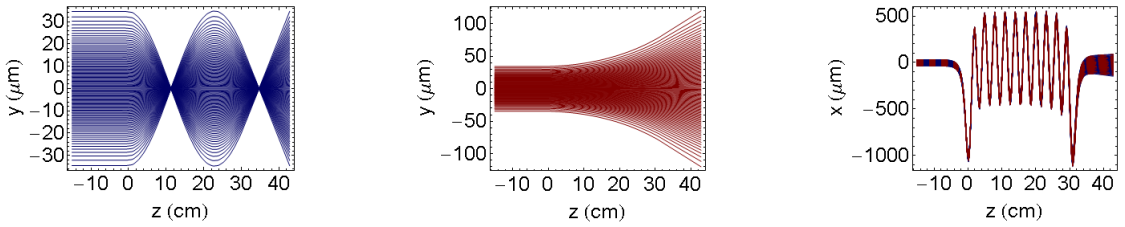

(a) (b) (c)

Figure 2.7: (a) Collection of electron trajectories in the y-z plane with $B_{z,und}$ included in simulation. (b) Collection of electron trajectories in the y-z plane with $B_{z,und}$ "turned off". (c) Collection of electron trajectories in the x-z plane with $B_{z,und}$ "turned off" (dashed red) over-layed on the trajectories with $B_{z,und}$ included in simulation (blue). These figures are reproduced from our publication, Ref. [57].

The overall wiggling motion of the beam in the x-z plane is largely unchanged between a simulation with the full undulator field map and a simulation with the longitudinal component set to zero (Fig. 2.7c), validating our assumption during the 1-D calculation of IFEL energy exchange that the field could be approximated by a purely horizontal field. However, when the aim of the interaction is to impart a transverse deflection, displacing electrons from on-axis propagation, the focusing effect of the undulator field works to counteract the desired deflection. This effect became immediately apparent, as shown in Figs. 2.8 and 2.9, when we performed GPT simulations of our proposed THz streaking scheme.

Figure 2.8 shows the input THz electric field and GPT simulation results for a streaking scheme based on the TE_{11} mode of the CPPWG structure using an input 200 fs electron bunch with zero emittance and a round transverse profile, $\sigma = 20$ um. In Fig. 2.8c, we

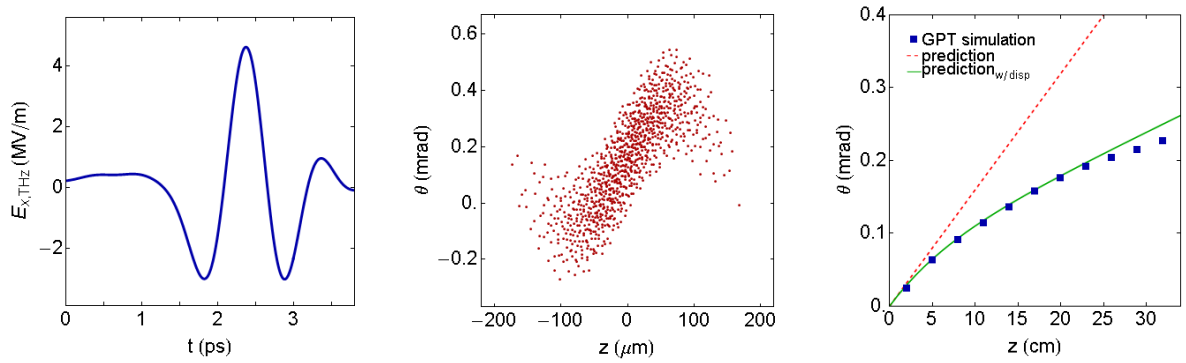

(a) (b) (c)

Figure 2.8: (a) Snapshot of the TE_{11} mode field profile, E_x, taken at an x-displacement of 0.977 mm, corresponding to the mode peak, and a depth of 1 cm inside the guide. (b) Angular deflection of a zero-emittance beam streaked by interaction with the TE_{11} mode. (c) A plot of the predicted and simulated angular deflection at different times throughout the duration of interaction, given an idealized, on-axis test beam. These figures are reproduced from our publication, Ref. [57].

show the peak angular deflection simulated in GPT as a function of interaction distance. Alongside the GPT results, we compare the magnitude of the deflection predicted by our analytical model (Eq. 2.67), with and without the field amplitude adjusted to account for dispersive pulse broadening.

The value of the envelope function, f_{env}, used in the analytical prediction was determined from snapshots of the GPT profile of the THz field in the guide. Although the GPT simulation results are in excellent agreement with the analytical prediction, once the calculation is adjusted for the approximate decay in field amplitude due to pulse dispersion, the magnitude of the angular deflection imparted by this scheme is simply too small to make the technique competitive with THz-driven split ring resonator schemes, already demonstrating 2.5 fs resolution [26].

For comparison, Fig. 2.9 shows the input THz magnetic field and GPT simulation results for a streaking scheme using the TE_{20} mode of the CPPWG structure. Based on our analytical prediction, we expect this scheme to produce a much larger angular deflection than

the TE_{11} case, but as we see in Fig. 2.9c, the value simulated by GPT diverges significantly from the analytical prediction, even with dispersion accounted for by an attenuated peak field.

The GPT simulation and analytical prediction are consistent for the first few periods, but as electrons move farther off-axis, the focusing force of the undulator reverses the direction of deflection, such that by the end of the 30 cm undulator, the beam is deflected with the opposite sign. To see this effect, after identifying the electron with maximum simulated deflection in the final beam distribution, we plotted the angular deflection of this electron at regular intervals during the interaction, shown as blue squares in Fig. 2.9c. The simulation results in Fig. 2.9c suggest that the deflection was reaching another local maximum, just prior to reversing direction again under the influence of undulator focusing. With the longitudinal component of the undulator field turned off in the GPT simulation, this reversing effect disappears without the corresponding undulator focusing (seen in Fig. 2.7).

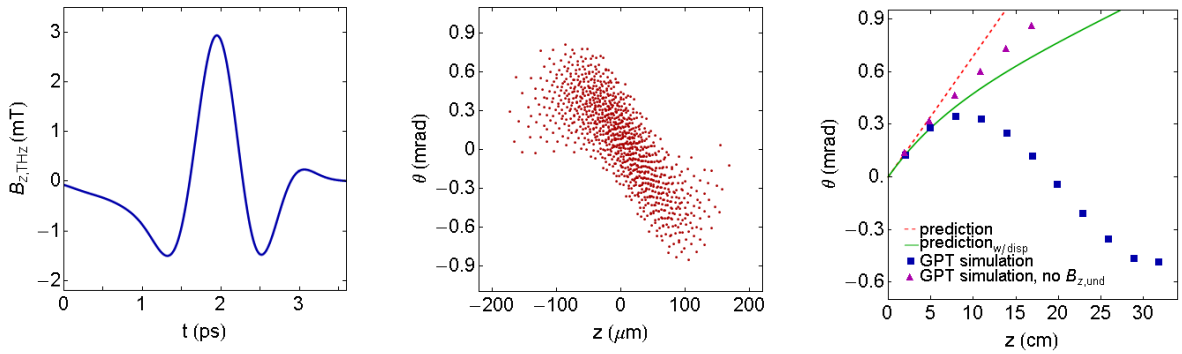

(a) (b) (c)

Figure 2.9: (a) Snapshot of the on-axis TE_{20} mode field profile, B_z, taken at a depth of 6 mm inside the guide. (b) Angular deflection of a zero-emittance beam streaked by interaction with the TE_{20} mode. (c) A plot of the predicted and simulated angular deflection at different times throughout the duration of interaction. The simulated maximum angular deflection with the longitudinal undulator field $B_{z,und}$ turned off is marked by pink triangles. These figures are reproduced from our publication, Ref. [57].

Surprisingly, even with the TE_{20} streaking scheme spoiled by the undulator focusing,

the final angular deflection simulated by GPT is still larger than the deflection in the TE_{11} case, given the same initial THz pulse energy. However, if we were to improve the coupling efficiency and/or the available THz energy, we can expect the TE_{11} scheme to outperform the TE_{20} case, in which the magnitude of the deflection is fundamentally limited by the undulator focusing. These simulation results indicate that at best we could expect resolution at the sub-ps level given our current setup capabilities.

CHAPTER 3

Experimental Techniques: THz generation, detection, and guided propagation

The increasing availability and power of today's THz sources is the result of significant contributions from many different research areas, including electrical engineering, accelerator physics, and nonlinear optics, along with frequent interdisciplinary collaborations. The course of research presented in this thesis has intersected with a variety of THz technologies, from the optical rectification used to generate the THz pulse and electro-optic sampling used to characterize it, to the FEL experiment performed to amplify it.

This chapter begins with an introduction to the optical rectification technique that produced the THz used for this experimental work, followed by a discussion of the THz source set-up and transport system. We will also review the THz detection methods used to characterize the source and the curved parallel plate waveguide with which we controlled the THz propagation during IFEL interaction.

The diagnostic work for this experiment was performed primarily using pyroelectric detectors and electro-optic sampling in zinc telluride. However, the THz source presented an opportunity to work on an additional project using plasmonics-enhanced photoconductive antennas for THz detection. Ultimately this technology was used for measurements of the transient electric field of a passing electron beam, providing a non-invasive timing diagnostic on the PEGASUS beamline. We discuss the motivation for this experiment and the capabilities of this detection method along with a summary of the experimental results at the end of this chapter.

3.1 Optical rectification

The process of optical rectification takes its name from the analogous mechanism of electronic signal rectification in diodes, whereby an AC current is converted into a DC current. For optical rectification in nonlinear anisotropic crystals, an incoming oscillating electric field produces a time-averaged shift in the polarization of the bound electronic charge, rather than a symmetrically alternating polarization of charges in the material [67].

To give a more detailed picture of the process, we will begin with a description of the polarization of the crystal. The polarization is determined by the displacement of charges from their equilibrium positions in the crystal structure. To define the polarization $\mathbf{P}$, we need the sum over the charges, q, indexed by l, such that

$$\mathbf{P} = \sum_l q_l \left(x_l - x_{l,0}\right) \tag{3.1}$$

where x_l is the current position and $x_{l,0}$ is the equilibrium position. In a dielectric crystal, like lithium niobate, an applied electric field can induce a non-zero polarization, i.e. shift the position of the charges, because the anisotropic nature of the crystal structure means there is a preferred direction for that shift in position. This asymmetry shows up in the description of how the material polarization, $\mathbf{P}$, depends on the external electric field, $\mathbf{E}$, that is, the electric susceptibility, χ. For anisotropic materials, this relation can be decomposed into a Taylor expansion to isolate the different order effects. The phenomenon of optical rectification is a second order effect, which means it typically doesn't become relevant until there is a substantial external electric field, like the intense femtosecond laser pulses used to drive THz generation. The polarization as a function of external electric field is

$$\mathbf{P} = \epsilon_0 \chi^{(1)} \mathbf{E} + \epsilon_0 \chi^{(2)} \mathbf{E}^2 + ... \tag{3.2}$$

Focusing on the second order term with the nonlinear susceptibility tensor, $\chi^{(2)}$, we can rewrite this expression as

$$\chi^{(2)}\mathbf{E}^2 = \sum_j \sum_k X_{ijk} E_j E_k \,. \tag{3.3}$$

If we assume a linearly polarized electric field, $\mathbf{E}_y$, as is the case with our optical rectification set-up, this term can be simplified to

$$\chi^{(2)}\mathbf{E}^2 = \mathbf{u} E_y^2 \tag{3.4}$$

where $\mathbf{u}$ is a vector describing the susceptibility, determined by the nonlinear coefficient of the material.

Let's specify the external electric field to have the form

$$\mathbf{E} = E_0 \sin(\omega_0 t)\, \hat{\mathbf{y}}. \tag{3.5}$$

The asymmetric preference in polarization means that even though the driving field has a symmetrically oscillating electric field amplitude, the crystal polarization does not average to zero over each oscillation. Taking the time average of the polarization, the first order term, which depends on $\sin(\omega_0 t)$, averages to zero, but the second order term, which depends on $\sin^2(\omega_0 t)$, gets a factor of one half, and becomes

$$\langle \mathbf{P} \rangle = \frac{\epsilon_0 E_0^2}{2} \mathbf{u} \,. \tag{3.6}$$

This picture covers just the definition of optical rectification, in which an alternating polarization becomes a "DC" one, and doesn't yet describe the process of THz generation. The mechanism of THz generation requires multiple frequencies and falls into the category of difference-frequency mixing. Before we introduce a quantitative description, it is interesting

to note how the form of Eq. 3.1 foreshadows THz generation from a short, intense laser pulse. If we consider the envelope of the laser pulse, we have a ramping up of the electric field, indicating an increasing polarization, followed by a ramping down of the electric field, in which the polarization returns to zero. The acceleration of the net charge over the course of this perturbation produces radiation, effectively mapping the envelope of the laser pulse. Obviously, a short laser pulse envelope corresponds to a broadband spectral content. To see how the individual frequencies interact to produce a difference-frequency mixed radiation source, we'll now calculate the change in polarization using an example electric field composed of two frequencies.

$$\mathbf{E} = \left(E_0 \sin\left(\omega_0 t\right) + E_1 \sin\left(\omega_1 t\right)\right) \hat{\mathbf{y}} \tag{3.7}$$

Substituting this new 2-frequency form of the electric field into Eq. 3.1, we have

$$\chi^{(2)}\mathbf{E}^2 = \mathbf{u}\left(E_0 \sin\left(\omega_0 t\right) + E_1 \sin\left(\omega_1 t\right)\right)^2 \tag{3.8}$$

Using the trigonometric identity $2 \sin\theta \sin\phi = \cos(\theta - \phi) - \cos(\theta + \phi)$, we can rewrite this expression in terms of a slow and a fast oscillating term

$$\chi^{(2)}\mathbf{E}^2 = \mathbf{u}\left[E_0^2 \sin^2\left(\omega_0 t\right) + E_1^2 \sin^2\left(\omega_1 t\right) + E_0 E_1 \left(\cos\left(\left(\omega_0 - \omega_1\right)t\right) - \cos\left(\left(\omega_0 + \omega_1\right)t\right)\right)\right] . \tag{3.9}$$

Now, to determine the time averaged polarization, we'll once again neglect the first order term in Eq. 3.1. This term averages to zero at a timescale larger than the periods associated with frequencies ω_0 and ω_1. This means the even higher frequency oscillation of the term proportional to $\cos\left(\left(\omega_0 + \omega_1\right)t\right)$ will also average to zero. The remaining expression

$$\langle \mathbf{P} \rangle = \frac{\epsilon_0 E_0^2}{2}\mathbf{u} + \frac{\epsilon_0 E_1^2}{2}\mathbf{u} + \epsilon_0 E_0 E_1 \cos\left(\left(\omega_0 - \omega_1\right)t\right)\mathbf{u} \tag{3.10}$$

includes the two constant terms, in which the high frequency sine-squared dependence has averaged to 1/2, and a time-dependent term with a slowly variation oscillation of frequency $\omega_0 - \omega_1$. This difference frequency mixing moves the bound charges in a beat wave which produces THz radiation.

Fundamentally, the conversion efficiency improves with larger nonlinear coefficients, however, additional mechanisms can limit the effective conversion of laser energy into THz radiation, in particular reabsorption at THz frequencies and velocity mismatch between laser and THz propagation, as well as pump distortion and depletion.

One of the key advantages of lithium niobate (LN) over other nonlinear crystals for the application of optical rectification is its relatively large effective nonlinear coefficient (d_{eff} = 168 pm/V) [68]. It also benefits from a large bandgap compared to other standard nonlinear crystals, like GaP and ZnTe, which reduces the prevalence of other effects, such as multiphoton absorption, which compete with the desired optical rectification mechanism [69].

Unlike GaP and ZnTe, the refractive index of LN at THz frequencies is significantly higher than at the optical frequencies of the driving laser pulse, severely limiting the interaction length that would be possible in a simple collinear geometry. To overcome this challenge, the standard technique, initially proposed in Ref. [21], is to induce a pulse front tilt in the pump laser in order to match the laser group velocity to the THz phase velocity in a non-collinear geometry. We discuss the requirements for this set-up in the following section.

3.1.1 Pulse front tilting for optical rectification

In Fig. 3.1 we show a diagram of the propagation of the laser pump and the outgoing THz pulse within the LN crystal. Because they do not propagate collinearly, the effective group velocity of the laser pulse is just the component of its velocity along the direction of the THz propagation. With the introduction of a tilt in the intensity front of the laser, in the frame of the THz pulse shown in Fig. 3.1, it appears as if the laser moves collinearly. It is the angle of the pulse front tilt that sets the effective "collinear" propagation, establishing

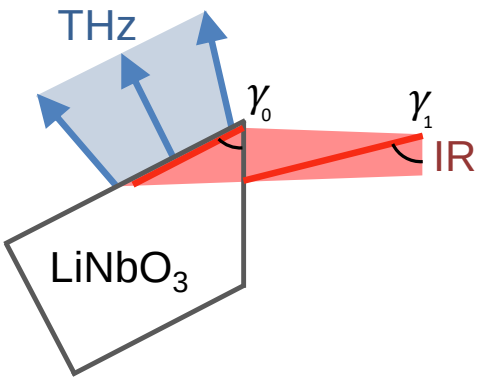

Figure 3.1: Diagram of the laser pulse (IR) propagating in the lithium niobate ($LiNbO_3$) crystal with an intensity front tilted by angle, γ_0, inside the crystal. Because the index of refraction for the THz is over twice as large as that of the laser, this geometry allows velocity matching for the projection of the IR traveling collinearly with the THz produced via optical rectification. The conversion efficiency is significantly enhanced by the extended interaction length. The angle γ_1 of the pulse front tilt outside the crystal must be pre-adjusted to compensate for the change in angle accrued by the pulse while traveling inside the crystal with an index of refraction greater than 1.

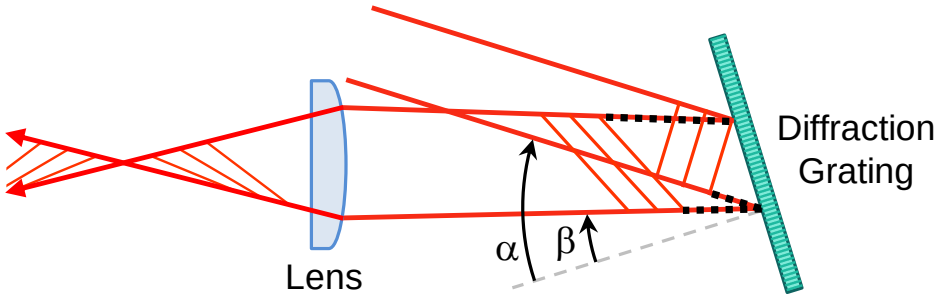

Figure 3.2: This diagram, though not to scale, shows the principles used to tilt the intensity front of the laser pulse before it enters the LN crystal. When the laser is reflected from the diffraction grating, because each transverse component of the laser travels the same total path length, one side of the intensity front ends up ahead of the other. This is illustrated by the slant in the red lines indicating the tilt of the intensity front. The black dotted line shows how each side has traversed the same total distance. The angle, α, at which the laser is incident on the grating is related to the angle, β, at which the laser leaves the surface be the grating equation, Eq. 3.12. A lens is then used to image the pulse-front-tilted laser into the LN crystal. The laser passes through a focus right before the crystal surface.

the appropriate matching conditions for the THz phase velocity. The velocity matching condition, in terms of the pulse front tilt angle γ_0 is [21]

$$v_{laser}^{gr} \cos(\gamma_0) = v_{THz}^{ph} \,. \tag{3.11}$$

The 800 nm Ti:Sapphire laser pulse used to pump the LN crystal in our set-up has a group index of refraction of 2.264 at 300 K, while the THz has a refractive index around 4.96 [69]. The required pulse front tilt angle inside the LN crystal is therefore $\gamma_0 = 63°$.

We'll now describe the steps used to achieve this pulse front tilt, following closely the discussion in Ref. [69]. We use a diffraction grating and a lens to image the laser onto the crystal, as shown in the diagram in Fig. 3.2. When the laser is incident on the grating

surface at an angle, α, from normal, the corresponding angle at which the laser exits the grating surface, β, is given by the grating equation

$$\sin(\alpha) + \sin(\beta) = \frac{n\lambda}{d_{grating}} \,. \tag{3.12}$$

Here d is the spacing between grooves in the grating, λ is the wavelength of the light, and the integer value of n determines the mode propagating off the surface. For our process we use the first order mode, $n = 1$. To determine the pulse-front-tilt angle imparted by reflection off the grating we can look more carefully at the geometry of the problem, as in Fig. 3.3.

After reflection off the grating, one side of the laser pulse lags by a distance of $\ell_1 + \ell_2$ which is determined by the width of the laser projected onto the grating, w, the incident angle α, and the reflected angle β, such that

$$\ell_1 + \ell_2 = w\,\sin(\alpha) + w\,\sin(\beta)\,. \tag{3.13}$$

To determine the pulse front tilt from this expression, we use the relation between the width of the laser pulse, h, and the projected width, w, which is $h = w\,\cos(\beta)$. The result is

$$\tan(\gamma_2) = \frac{\ell_1 + \ell_2}{h} = \frac{\sin(\alpha) + \sin(\beta)}{\cos(\beta)} \,, \tag{3.14}$$

which, using Eq. 3.12, simplifies to

$$\tan(\gamma_2) = \frac{\lambda}{d\,\cos(\beta)} \,. \tag{3.15}$$

To image this pulse-front-tilted laser profile into the few-mm LN crystal, we used a focusing lens, as shown in Fig. 3.2. The LN crystal face is placed at the image plane of the lens. This distance from the lens to the crystal, L_2, is determined using the thin lens

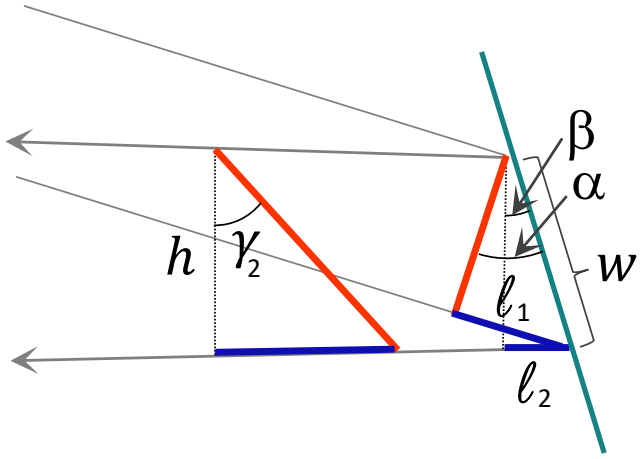

Figure 3.3: Diagram showing the pulse front tilt angle, γ_2, imparted by the grating for a laser arriving with the angle of incidence, α, and reflecting at an angle β relative to the normal vector of the grating as shown in Fig. 3.2. The relation between the pulse front tilt and these angles can be determined from the geometry of the problem, using the arbitrary laser width, h, along with the projected laser width on the grating, w. One end of the laser intensity front (marked in red) has advanced by a distance $\ell_1 + \ell_2$ (marked in blue) relative to the other side.

approximation in terms of a distance L_1 from the grating to the lens and a given focal length f, that is

$$\frac{1}{L_1} + \frac{1}{L_2} = \frac{1}{f}\,. \tag{3.16}$$

The ratio of the distance determines how much the transverse spot size of the laser is reduced, in our case by a factor of about 6, which in turn changes the magnitude of the pulse front tilt. The relation between the initial pulse front tilt, γ_2, and the pulse front tilt of the laser as it reaches the LN crystal surface, γ_1, is

$$\tan(\gamma_1) = \frac{L_1}{L_2}\tan(\gamma_2)\,. \tag{3.17}$$

As indicated in the diagram, the distance from the lens will change the magnitude of the pulse-front-tilt angle. In practice, once the crystal position was fixed in the optical set-up, the placement of the lens was routinely adjusted to maximize the output THz power by fine-tuning the pulse front tilt.

The last step in this pulse front tilt calculation is to characterize the angle inside the crystal. The angle of the pulse front tilt will change when the laser propagates inside the LN crystal because of the change in index of refraction, from 1 in air, to $n_{g,laser}$ in the crystal. This effect compresses the pulse in the propagation direction by a factor equaling the index of refraction ratio and therefore reducing the pulse front tilt angle. The combination of all these effects gives us the relation

$$\tan(\gamma_0) = \frac{L_1}{n_{g,laser}L_2}\tan\gamma_2\,, \tag{3.18}$$

which simplifies to

$$\gamma_0 = \tan^{-1}\left(\frac{L_1\lambda}{n_{g,laser}L_2\,d\,\cos(\beta)}\right)\,. \tag{3.19}$$

With these formulas we can work backwards to determine what incident angle, α, and what lens placement, L_1, we need to achieve the desired pulse front tilt.

3.2 THz source setup

A diagram of the full THz source set-up is shown in Fig. 3.4. For the experimental work presented in this thesis, THz radiation was produced via optical rectification of a Ti:Sapphire laser pulse, peaked at 800 nm with a 30 nm bandwidth, running at a 1 kHz repetition rate. We used a stoichiometric lithium niobate ($LiNbO_3$) crystal, abbreviated as "LN", doped with magnesium oxide (0.67%) to reduce its susceptibility to optical damage. The IR pulse energy entering the table was typically 1-1.4 mJ with a corresponding THz output around 1 μJ.

With phase-matching satisfied, the optical-to-THz energy conversion efficiency is described by [68]

$$\eta_{THz} = \frac{2\omega^2 d_{eff}^2 L^2 I}{\varepsilon_0 n_{IR}^2 n_{THz} c^3} \left(\frac{\sinh\left(\alpha_{THz} L/4\right)}{\alpha_{THz} L/4} \right)^2 e^{-\alpha_{THz} L/2} \tag{3.20}$$

where ω is the THz frequency, d_{eff} is the effective nonlinear coefficient, L is the length of the crystal, I is the intensity of the laser, and α_{THz} is the intensity absorption coefficient for THz radiation in the crystal.

A key improvement to the THz conversion efficiency can be accomplished by reducing the absorption coefficient via cooling of the crystal. This has led to THz conversion efficiencies over 3% in LN [70], an order of magnitude larger than typically produced at room temperature. A cooling technique was previously implemented at UCLA [71] using a stand alone vacuum chamber to house the LN crystal while mounted in indirect contact with a liquid nitrogen reservoir.

The initial design of the THz IFEL experiment presented in this dissertation included the use of this LN cooling chamber to improve our THz conversion efficiency from the room temperature (0.1%) level. However, subsequent measurements did not indicate an

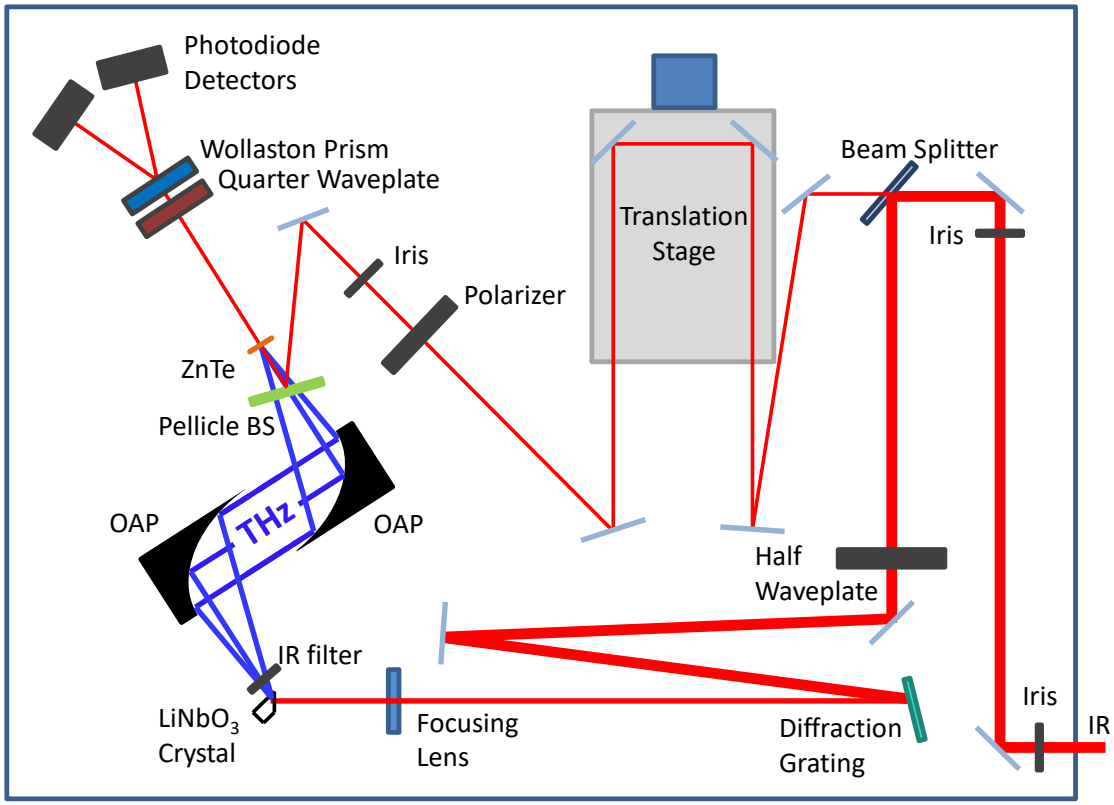

Figure 3.4: Benchtop set-up composing the THz source at UCLA. The IR pump pulse, generated by a Ti:Sapphire laser, enters the set-up at the bottom right. 99% of the laser was directed to the pulse-front-tilted optical rectification set-up, composed of the half waveplage, diffraction grating, lens, and $LiNbO_3$ crystal at the bottom of the diagram. The remaining laser pulse was used for the electro-optic sampling diagnostic, composed of the translation stage, pellicle beam splitter (to bring IR into collinear propagation with the THz), nonlinear ZnTe crystal, quarter waveplate, wollaston prism, and photodiode detectors. The THz produced in the LN crystal was collimated and focused onto the ZnTe crystal using a pair of off-axis parabolic (OAP) mirrors.

improvement in the final THz energy. This is most likely the result of insufficient thermal contact between the crystal and the copper mount, leading measurements performed with a thermocouple attached to the copper mount to underestimate the actual crystal temperature during the cooling process.

The copper mount is expected to contract when cooled, changing the position of the crystal in the process. While this effect could be compensated by adjusting the IR pump alignment on the THz board, during the actual THz IFEL experimental run, such changes to the crystal position could have adversely affected the coupling of the THz into the CPPWG, by introducing aberrations into the carefully aligned THz transport system discussed below.

Another unintended consequence of the LN cooling design was some damage on the crystal surface. While the photorefractive damage threshold is expected to be around MW/cm^2 [72] for our MgO doped crystal, the thermal vacuum gel used to improve contact between the copper mount and crystal was easily burned onto the crystal surface at the intensity level (100 W/cm^2) of our THz source setup.

As shown in Fig. 3.4, a beam splitter directed 99% of the incoming laser to the THz generation optics; the remaining pulse was used as the probe in an electro-optic sampling diagnostic. The polarization of the laser was optimized with a half waveplate before entering the pulse-front-tilt set-up composed of the grating and lens. The primary adjustments performed to maximize the THz output power on a day-to-day basis included optimizing the alignment of the laser onto the grating, the relative distances of the grating-lens-crystal system, and the transverse position of the LN crystal.

3.2.1 THz detection

To characterize the average output power of the THz source, we used a large-aperture pyroelectric detector, i.e. a laser thermal power sensor, calibrated for the THz frequency range. The device reacted to the change in temperature of the sensor area due to THz absorption, but was sensitive to IR absorption as well, so an IR filter was placed between the LN crystal and detector.

A small-area pyroelectic detector was used to measure the relative THz pulse intensity after focusing. The short (sub-μsec for 50 Ω termination [73]) response time provided single shot measurement capability and was used to optimize the alignment of the THz focal point. Because the pyroelectric detector was also sensitive to IR, it provided a convenient method of aligning the IR probe pulse, used for electro-optic sampling, to be spatially overlapped with the THz focus.

For a full description of the THz temporal profile, not just pulse energy, we used electro-optic sampling (EOS), with the relevant optical components also pictured in Fig. 3.4. This technique will be discussed in detail in a subsequent section of this chapter. The EOS measurement was performed using a zinc telluride (ZnTe) crystal placed at the focus of the THz pulse, which would later correspond to the entrance to the THz waveguide.

3.2.2 THz transport

The THz pulse produced via optical rectification diverges as it propagates away from the LN crystal. To collimate the THz pulse, an off-axis parabolic mirror (OAP) is positioned with the crystal at its focus, such that light rays leaving the crystal become parallel after reflection off of the mirror. A second OAP is used to focus the collimated THz beam onto the ZnTe crystal for EOS measurements or into the entrance of the waveguide.

In order to accommodate the LN cooling chamber (ultimately unused), the first collimating OAP needed to be >10 cm away from the crystal, leading to the use of large diameter (101.6 mm), long focal length (152.4 mm) mirrors to maximize THz capture. The reduced THz intensity in this large area transport system made measurements of the spot size during transport prohibitively difficult, but the focus of the second OAP produced a spot size of 2-3 mm. By decreasing the relative focal length of the second OAP, we could produce a tighter focus but also introduce aberrations to the THz profile coupling into the waveguide. In the THz FEL experiment, we switched to a 101.6 mm focal length mirror to couple the THz into the guide. This gave us a little more room to insert optics to pick off the THz pulse at the exit of the guide, and also potentially improve the total power coupled into the guide,

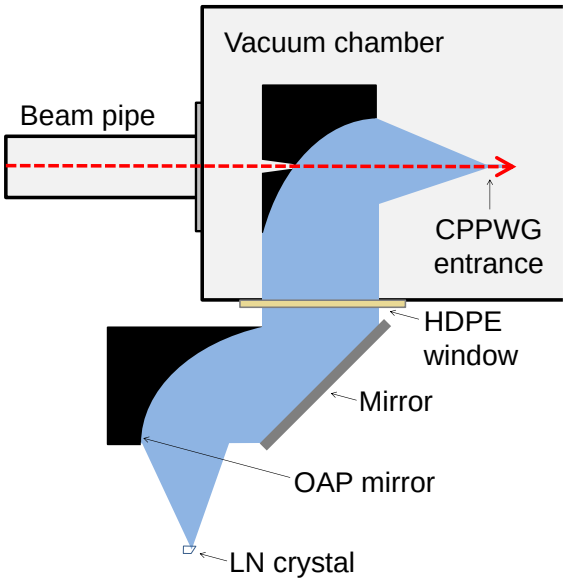

Figure 3.5: Transport of the THz pulse (blue shaded region) into collinear propagation with the electron beam (dashed red) on the beamline was accomplished with a pair of off-axis parabolic (OAP) mirrors.

although this effect was not verified.

For the initial EOS characterization of the source, a pellicle beam splitter was used to bring the IR probe beam and THz pulse into co-propagation. The pellicle was transparent to THz, but partially reflective for the IR, acting as a mirror which controlled the probe beam alignment onto the ZnTe, as in Fig. 3.4.

Eventually, for interaction with the electron beam, the THz pulse and electrons would need to be brought into collinear propagation inside of the waveguide. This was accomplished by a small hole in the middle of the second OAP, allowing transmission of the beam in the geometry shown in Fig. 3.5. On the mirror's front surface this hole is 2 mm in diameter, negligible compared to the 101.6 mm diameter of the mirror itself, so that the THz loss upon reflection from the mirror is minimal. However, the back of the hole, on the side where the beam enters, was counterbored with a 10 mm diameter to reduce the alignment constraint on the electron beam path.

The flat mirror between OAPs ensured a configuration in which any aberrations in the THz profile caused by the first OAP would be compensated by the second, with all light rays traveling an equal distance. Because the position of the THz waveguide and undulator apparatus was fixed on the beamline at PEGASUS, the alignment of the THz beam up to the entrance of the waveguide constrained the position of LN crystal. A single LED was positioned at the waveguide entrance, acting as a point source of light which was back-propagated by the system of OAPs and then focused at the desired location of the LN crystal. Subsequent optimization of the THz output power would be made by adjusting optics upstream of the crystal, rather than moving the crystal position. After the THz transport optics were fixed in position, the THz window, made of high-density polyethylene (HDPE) with a 101.6mm clearance aperture, was mounted to the vacuum chamber.

3.3 Electro-Optic Sampling

The diagnostic technique of electro-optic sampling (EOS) uses the linear electro-optic (Pockels) effect in a nonlinear optical crystal, much like optical rectification. In this case the electric field of the THz pulse changes the polarization of the crystal, which modulates the signal of the coincident IR probe as it passes through the crystal. Specifically, the second order change in the electric susceptibility, χ, as discussed in section 3.1, alters the indices of refraction within the electro-optic crystal, producing a phase difference between the components of the IR probe aligned with the principle axes of the new refractive index ellipse.

We will begin our discussion with a few background definitions. A detailed and comprehensive discussion of electro-optic modulation of optical radiation can be found in the textbook [74] by A. Yariv. The refractive index in a material is given by, $n = \sqrt{\epsilon_r \mu_r}$ where the relative permittivity, ϵ_r, is equal to the electric susceptibility $\chi + 1$, and the relative permeability, μ_r, can typically be approximated as 1. To model the propagation of light through a crystal, it is useful to define the refractive index ellipsoid

$$\frac{x^2}{n_x^2} + \frac{y^2}{n_y^2} + \frac{z^2}{n_z^2} = 1 \tag{3.21}$$

If the magnitude of the indices of refraction differ between the different components defining the ellipse axes, this corresponds to a birefringence in the crystal, with the disparate components denoted as the "ordinary" and "extraordinary" ray. The linear electro-optic effect describes the case in which the magnitude of the ordinary and extraordinary rays change by an amount proportional to an applied electric field, $\mathbf{E}$, such that the new refractive index ellipsoid is given by

$$\sum_{i,j} \left(\frac{\delta_{ij}}{n_{i,0}^2} + \sum_k r_{ijk} E_k \right) u_i u_j = 1 \ . \tag{3.22}$$

Because the second term is symmetric (i.e. $r_{ijk} = r_{jik}$), the conventional notation describing the material's electro-optic tensor, $\mathbf{r}$, replaces the ij index with a single index i over the six unique combinations, such that the electro-optic tensor takes the form

$$\mathbf{r} = \begin{bmatrix} r_{11} & r_{12} & r_{13} \\ r_{21} & r_{22} & r_{23} \\ r_{31} & r_{32} & r_{33} \\ r_{41} & r_{42} & r_{43} \\ r_{51} & r_{52} & r_{53} \\ r_{61} & r_{62} & r_{63} \end{bmatrix} \tag{3.23}$$

and the second term in the index ellipsoid equation becomes

$$\Delta \left(\frac{1}{n^2} \right)_i = \sum_j r_{ij} E_j \qquad i = 1, .., 6 \ . \tag{3.24}$$

To calculate the new indices of refraction, we'll need to know the electro-optic tensor of the material we are using, in our case zinc telluride (ZnTe), and the polarization angle of

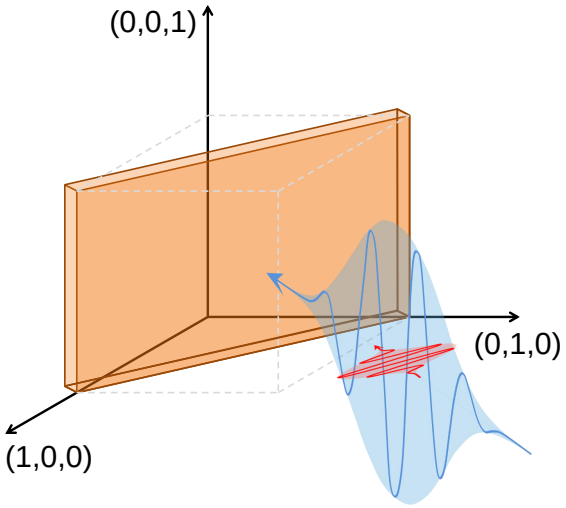

Figure 3.6: The THz pulse (blue shading) is incident normally onto the ZnTe crystal surface which is cut in the (110) plane relative to the cubic lattice. The IR probe pulse, shown in red (not-to-scale, actually 2 orders of magnitude shorter), is spatially overlapped at normal incidence, sampling different regions in the THz temporal profile depending on the time of arrival.

the applied electrical field. Zinc telluride (ZnTe) is optically isotropic for negligible applied field, such that $n_{x,0} = n_{y,0} = n_{z,0} = n_0$. The only non-zero values of the electro-optic tensor are r_{41}, r_{52}, and r_{63}. These are all equivalent in magnitude, so the value r_{41} will now be used to refer to any of these three components.

With this information, the equation for the refractive index ellipse reduces to

$$\frac{x^2}{n_0^2} + \frac{y^2}{n_0^2} + \frac{z^2}{n_0^2} + 2r_{41}\left(E_x yz + E_y zx + E_z xy\right) = 1. \tag{3.25}$$

We'll adopt the conventions defined in Ref. [75] to describe the crystal coordinate system and incident THz polarization. In terms of the cubic lattice structure of the crystal, the crystal surface is in the (110) plane as shown in Fig. 3.6 with the THz pulse arriving at normal incidence.

Assuming the electric field of the THz pulse is polarized at an angle α with respect to the

[(1,0,0);(0,1,0)] crystal axis, we'll now determine the new indices of refraction. The electric field vector is given by

$$\mathbf{E}_{THz} = E_{THz} \begin{bmatrix} -\cos(\alpha)/\sqrt{(}2) \\ \cos(\alpha)/\sqrt{(}2) \\ \sin(\alpha) \end{bmatrix} \tag{3.26}$$

in the coordinate system of the crystal cubic lattice. To calculate the eigenvalues of Eq. 3.25 which will determine the new indices of refraction, it is helpful to reformulate in terms of matrix notation. By writing Eq. 3.25 in the form $\mathbf{u} \cdot \hat{\eta} \cdot \mathbf{u} = 1$, we construct the so-called impermeability tensor of the crystal, as reported in Ref. [75]:

$$\hat{\eta} = \frac{1}{n_0^2} \begin{bmatrix} 1 & 0 & 0 \\ 0 & 1 & 0 \\ 0 & 0 & 1 \end{bmatrix} + r_{41} E_{THz} \begin{bmatrix} 0 & \sin(\alpha) & \cos(\alpha)/\sqrt{(}2) \\ \sin(\alpha) & 0 & -\cos(\alpha)/\sqrt{(}2) \\ \cos(\alpha)/\sqrt{(}2) & -\cos(\alpha)/\sqrt{(}2) & 0 \end{bmatrix} \tag{3.27}$$

with normalized eigenvectors

$$\mathbf{u}_1 = \frac{1}{2}\sqrt{1 + \frac{\sin(\alpha)}{\sqrt{1+3\cos^2(\alpha)}}} \begin{pmatrix} -1 \\ 1 \\ \frac{2\sqrt{2}\cos(\alpha)}{\sqrt{1+3\cos^2(\alpha)}+\sin(\alpha)} \end{pmatrix} \tag{3.28}$$

$$\mathbf{u}_2 = \frac{1}{2}\sqrt{1 - \frac{\sin(\alpha)}{\sqrt{1+3\cos^2(\alpha)}}} \begin{pmatrix} 1 \\ -1 \\ \frac{2\sqrt{2}\cos(\alpha)}{\sqrt{1+3\cos^2(\alpha)}-\sin(\alpha)} \end{pmatrix} \tag{3.29}$$

$$\mathbf{u}_3 = \frac{1}{\sqrt{2}} \begin{pmatrix} -1 \\ -1 \\ 0 \end{pmatrix} \tag{3.30}$$

$$\tag{3.31}$$

and eigenvalues

$$\lambda_{1,2} = \frac{1}{n_0^2} - \frac{r_{41}E_{THz}}{2}\left(\sin(\alpha) \pm \sqrt{1+3\cos^2(\alpha)}\right), \quad \lambda_3 = \frac{1}{n_0^2} + r_{41}E_{THz}\sin(\alpha) \tag{3.32}$$

using the reasonable assumption that $r_{41}E_{THz} \ll \frac{1}{n_0^2}$. The new indices of refraction, given by the relation $n_i = \frac{1}{\sqrt{\lambda_i}}$, are then

$$n_{1,2} = n_0 + \frac{n_0^3 r_{41}E_{THz}}{4}\left(\sin(\alpha) \pm \sqrt{1+3\cos^2(\alpha)}\right), \quad n_3 = n_0 - \frac{n_0^3 r_{41}E_{THz}}{2}\sin(\alpha). \tag{3.33}$$

The phase difference, Γ, accumulated by the components of the IR probe with frequency, ω, passing through a crystal of thickness d, is

$$\Gamma = (n_1 - n_2)\omega\frac{d}{c}. \tag{3.34}$$

Substituting in our new indices of refraction, this becomes

$$\Gamma = \frac{\pi d}{\lambda}n_0^3 r_{41}E_{THz}\sqrt{1+3\cos^2(\alpha)}. \tag{3.35}$$

This phase shift between the components of the IR probe parallel to the slow and fast axes effectively rotates the polarization of the IR pulse after traversing the crystal, with the magnitude of that rotation dependent upon the sign and magnitude of the THz electric field. To measure the change in the polarization, we used the well-established method of balanced diode detection.

In this set-up, as shown in Fig. 3.4, the IR probe passes through a quarter ($\lambda/4$) waveplate after leaving the ZnTe. The waveplate is oriented such that, if the IR probe is unmodulated in the ZnTe, the linear polarization is converted into a circular polarization. The orthogonal components of the IR probe, equal in magnitude in this circularly polarized case, are then spatially separated by a Wollaston prism. Two photodiodes are placed in the diverging paths

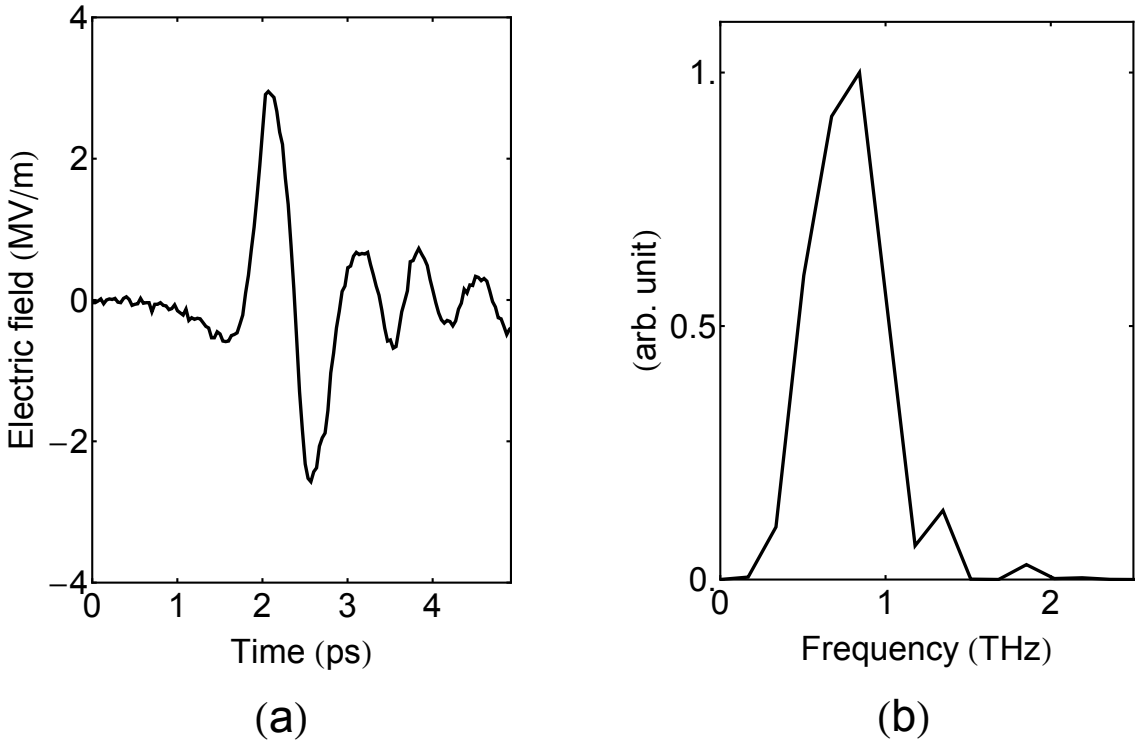

Figure 3.7: (a) EOS measurement of the temporal profile of the THz pulse using balanced diode detection to determine sign and magnitude of the electric field. The time of arrival of the IR probe was adjusted with a delay stage upstream. (b) Corresponding spectrum of the THz pulse.

of the now separated polarization components. The difference in their measured intensities is zero, corresponding to zero electric field magnitude.

Now, if the IR probe polarization is modulated in the ZnTe, when it passes through the waveplate, the resulting polarization will be elliptical. The orthogonal components that are separated in the Wollaston prism are therefore not equal in magnitude and the two photodiodes read different intensities. The sign of the THz electric field determines the sign of the initial rotation of the IR polarization in the ZnTe; this in turn determines which photodiode reads a larger signal. The difference in the photodiode signal therefore indicates both the sign and the magnitude of the electric field.

The magnitude of the electric field can be determined from the phase shift, Γ, using the

relation in Eq. 3.35, since the difference in signal between the two photodiodes is proportional to $\sin(\Gamma)$. A detailed calculation of how the magnitude of the two signals is determined by the modulation in the ZnTe and subsequent optical components is given in Appendix A.

Using this EOS technique in the arrangement shown in Fig. 3.4, the temporal field profile of the THz pulse was measured by scanning the arrival time of the IR probe pulse. An example of the measured waveform is shown in Fig. 3.7a with the corresponding spectrum (Fig. 3.7b) peaked near 0.8 THz.

3.4 Curved Parallel Plate Waveguide

To control the THz propagation during the IFEL interaction, we chose a curved parallel plate waveguide (CPPWG), shown in Fig. 3.8. This selection was based on previous studies of THz waveguides, particularly the investigation of guiding structures for a THz FEL oscillator in Refs. [56] and [76]. The results of these studies highlight that both the parallel plate structure and a dielectric lined waveguide have the advantage of small ohmic losses relative to more conventional waveguides for THz control, but the CPPWG offers the unique capability of variable plate spacing as well as easy fabrication.

The dynamic control of the waveguide aperture facilitates tuning of the guide's dispersive properties. We saw in our earlier discussion of the "zero-slippage" phenomenon that only a single combination of THz frequency, beam energy and plate spacing will allow simultaneous phase and group velocity matching. The adjustable plate spacing enables us to optimize the group velocity of the THz pulse for our given THz frequency. Alternatively, if the beam energy is fixed by some other experimental constraint, changing the plate spacing can maintain phase velocity matching for a resonant interaction even if the duration of the interaction is limited by poor group velocity matching.

One of the key reasons that the waveguide comparison study in Ref. [56] promoted the CPPWG design for FEL interaction was because of the ideal spatial overlap between the TE_{01} mode profile and the wiggling of an electron beam in a planar undulator. As we see in Fig. 3.9 showing the transverse profile of the TE_{01} mode, for an electron beam with average

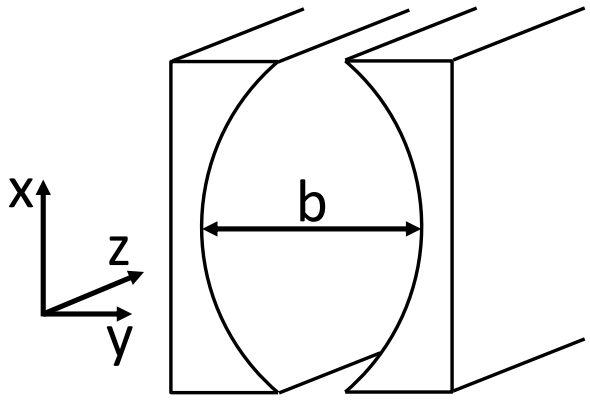

Figure 3.8: Diagram of the curved parallel plate waveguide (CPPWG) cross section. The plate spacing, b, is measured at the widest point between plates. For a confocal setting of the plates, the radius of curvature equals the separation, b. This configuration reduces the attenuation due to diffraction out of the gap between plates.

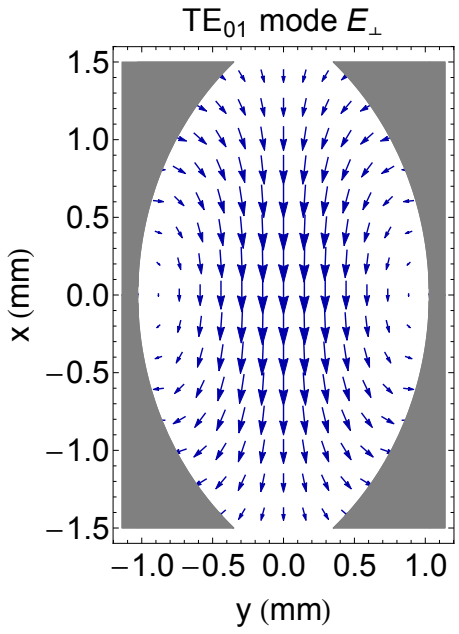

Figure 3.9: Vector plot showing the transverse profile of the electric field of the THz pulse in the TE_{01} mode of the CPPWG. An electron beam wiggling about the central axis in the x-z plane sees an electric field that is linearly polarized parallel to the direction of transverse motion and nearly constant in magnitude.

longitudinal motion parallel to the z-axis and a small transverse wiggle in the x-z plane centered within the cross-section of the plates, the THz electric field will appear linearly polarized with near constant magnitude in the vicinity of the beam.

The THz propagation in the CPPWG is determined by the dispersion relation giving the transverse wavenumber, k_{mn}, and longitudinal wavenumber, k_z,

$$\begin{aligned} k_{mn} &= \frac{1}{b}\left(n\pi + (2m+1)\tan^{-1}\frac{b}{\sqrt{2Rb-b^2}}\right) \\ k_z &= \sqrt{k_0^2 - k_{mn}^2}\ . \end{aligned} \tag{3.36}$$

The form of the longitudinal field, Φ_{mn}, corresponding to H_z for TE modes and E_z for TM modes, can be written in terms of the Hermite polynomials, He_m, as follows [62]

$$\Phi_{mn} = \frac{e^{\frac{-\beta_{mn}^2 x^2}{\alpha_{mn}(y)}}}{\sqrt[4]{\alpha_{mn}(y)}}\,\mathrm{He}_m\left(\frac{2\beta_{mn}x}{\sqrt{\alpha_{mn}(y)}}\right)\begin{pmatrix}\cos\\ \sin\end{pmatrix}\left[k_{mn}y + \frac{2\beta_{mn}^4 y x^2}{k_{mn}\alpha_{mn}(y)} - \left(m+\frac{1}{2}\right)\tan^{-1}\frac{2\beta_{mn}^2 y}{k_{mn}}\right]e^{\pm ik_z z} \tag{3.37}$$

where

$$\begin{aligned} \alpha_{mn}(y) &= 1 + 4\frac{\beta_{mn}^4 y^2}{k_{mn}^2} \\ \beta_{mn} &= \sqrt{\frac{k_{mn}}{\sqrt{2Rb-b^2}}} \end{aligned} \tag{3.38}$$

and R and b are the plate curvature and spacing of the CPPWG. The transverse E-field components are then given by

$$\begin{aligned} E_x &= \frac{-i}{k_{mn}^2}\left(k_z\frac{\partial E_z}{\partial x} - \omega\mu_0\frac{\partial H_z}{\partial y}\right) \\ E_y &= \frac{-i}{k_{mn}^2}\left(k_z\frac{\partial E_z}{\partial y} + \omega\mu_0\frac{\partial H_z}{\partial x}\right) \end{aligned} \tag{3.39}$$

The gap between plates does allow some attenuation of the THz pulse due to diffraction, as noted in the original proposal for this waveguide design [62]. The curvature of the plates

is fabricated specifically to combat this effect, making the plate surfaces function as curved mirrors which focus the THz within the waveguide channel. Because diffraction losses are minimized for a confocal setting (radius of curvature equal to plate spacing) [62], our CPPWG parameters were chosen for a near-confocal setting over the range of spacings we anticipated using during experiments.

Attenuation due to diffraction in the CPPWG diminishes with increasing frequency, i.e. decreasing wavelength, like [56]

$$\alpha_{diff} = \frac{\lambda_0 k_{mn}}{\sqrt{2\pi^3} ab \beta_{mn}} e^{-\frac{1}{2}a^2\beta_{mn}^2}. \tag{3.40}$$

As a result, the total attenuation, including losses due to the finite resistivity of the walls, decreases with increasing frequency, unlike conventional waveguides. Another consideration when choosing waveguide parameters is that decreasing the plate spacing increases the cut-off frequency within the waveguide and increases the rate of pulse broadening within the guide.

3.4.1 EOS measurements of tunable group velocity

One of the early measurements performed during this thesis work was a characterization of the THz propagation in a test CPPWG structure. The measurements formed the experimental results section of Ref. [55], in which we proposed the zero-slippage IFEL technique for THz-driven beam manipulation. The test structure was fabricated out of aluminum using conventional machining techniques at the UCLA Physical Sciences Machine Shop. The CPPWG plates were 15 cm long with a 3 mm radius of curvature and 4.25 mm thickness. To couple the THz into the waveguide, the plates were positioned on the optical breadboard of the THz source such that the THz focus was longitudinally aligned with the leading edge of the plates and transversely aligned in the middle of the gap between plates.

To determine this alignment, we used the IR probe that had been brought into co-propagation with the THz pulse using the pellicle as shown in Fig. 3.10. In this configuration,

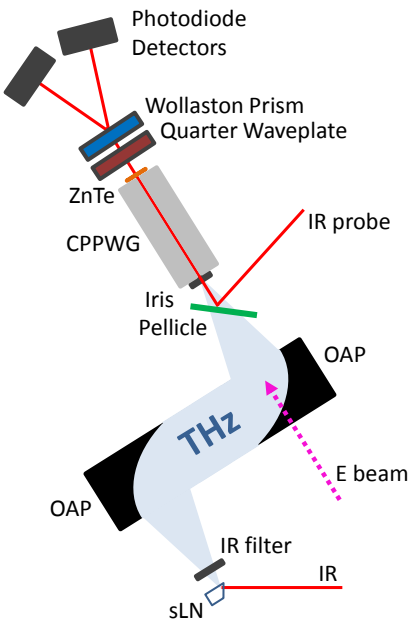

Figure 3.10: Diagram of EOS setup used to characterize THz dispersion in the CPPWG. The future trajectory of the electron beam is shown with a dashed pink line. This figure is reproduced from our publication, Ref. [55].

the IR pulse does traverse the length of the CPPWG with the THz, but the wavelength is small enough relative to the waveguide dimensions, that it passes through undistorted. With the plates aligned on either side of this IR probe, the ZnTe crystal for EOS measurements was placed flush against the end of the CPPWG. The results of the EOS timing scans performed for three different plate spacings are shown in Fig. 3.11.

These measurements were compared to a predicted pulse profile (dashed red line in Fig. 3.11), calculated using the initial pulse waveform measured at the entrance to the guide and the CPPWG parameters and dispersion for the given plate spacing. The calculation for these predicted waveforms did not include loss due to diffraction, but did account for coupling efficiency by scaling the magnitude of the initial field, matching the 1.5 mm spacing measurement.

The temporal profile of the measured and predicted waveforms for the 1.5 mm plate spacing are in good agreement, likely because diffraction out of the narrow gap is minimal. In contrast, for larger plate spacings there is a greater discrepancy between the measured

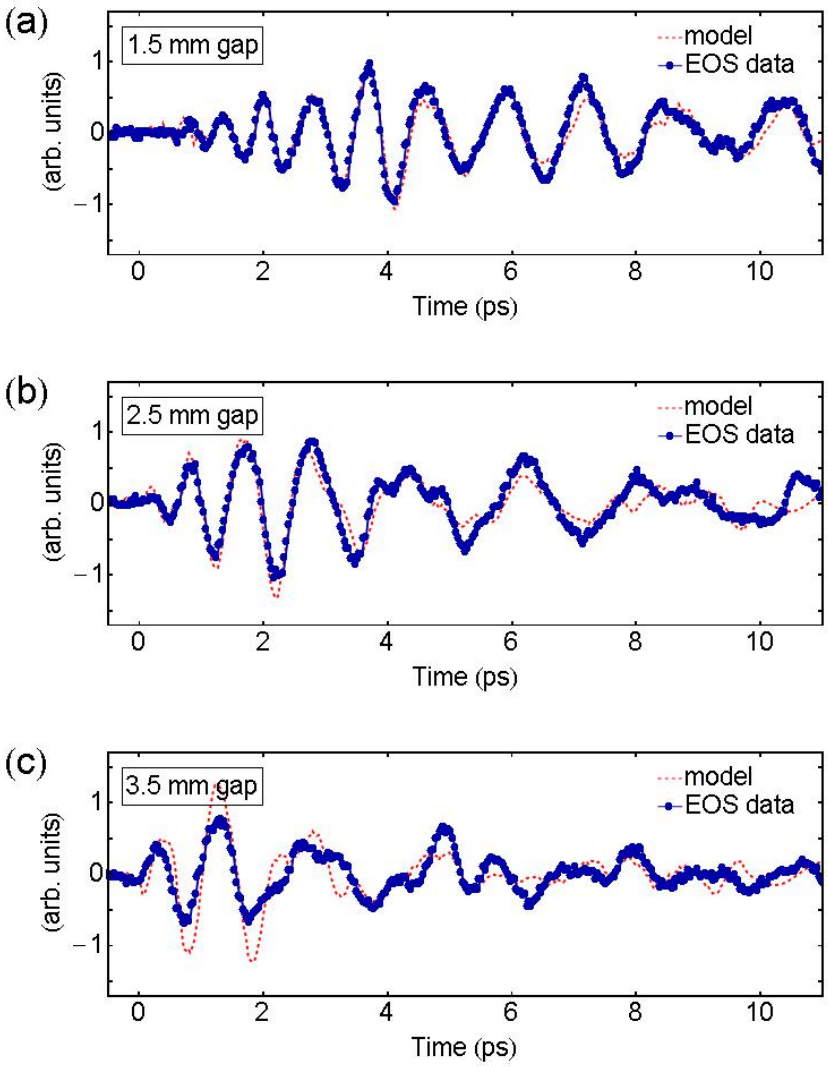

Figure 3.11: EOS measurements performed at CPPWG spacings of (a) 1.5 mm, (b) 2.5 mm, and (c) 3.5 mm. The "model" waveform shown by the dashed red line was determined in each case by evolving the THz waveform measured at the entrance to the guide using the dispersion for the given plate spacing. Diffraction plays a larger role in the distortion of the measured waveform at wider plate spacings. For narrower plate spacings, the group velocity is lower so the final THz pulse arrives at a greater time delay. These figures are reproduced from our publication, Ref. [55].

and predicted field magnitudes and waveforms, because of the larger impact of diffraction losses.

A relative timestamping of these measurements was made using an EOS measurement taken at the entrance to the guide. The first peak in the THz waveform was identified, then the delay stage scan was paused, the ZnTe was moved to the end of the waveguide, and the scan resumed. Starting the post-waveguide EOS scan immediately after the first peak in the pre-waveguide scan did not truncate any region of the final measured THz waveform, because the arrival time of the THz pulse was delayed by the guide, i.e. exactly the quantity we'd like to measure. This technique minimized timing errors caused by translation stage recoil, as would occur when reversing direction to return the stage to a previously identified position.

If Fig. 3.11, we see that the THz pulse experiences a longer time delay as the plate spacing decreases, corresponding to a slower group velocity, as expected. The time delay between the peak of the THz pulse envelope measured before and after the waveguide provides a means of directly estimating the THz pulse group velocity. The shape of the THz envelope is extracted from the raw measurement by factoring out the THz-frequency sinusoidal carrier wave, determined by a least-squares fit in the region of the peak field. The group velocities calculated from the time difference between envelope peaks, for both measured and predicted final THz waveforms, are shown in Fig. 3.12.

3.4.2 CPPWG modes for THz streaking diagnostic

Another beam manipulation application that could benefit from the "zero-slippage" technique is a longitudinal beam diagnostic using a THz-driven transverse deflection. This diagnostic is particularly attractive for a side-by-side study with the THz driven IFEL because both processes can utilize the same CPPWG-undulator apparatus, leaving the manipulation of the beam to be determined by which mode is excited in the waveguide. We considered this application using a simple analytical model in Ref. [55] and more thoroughly with 3-dimensional simulations using GPT in Ref. [57].

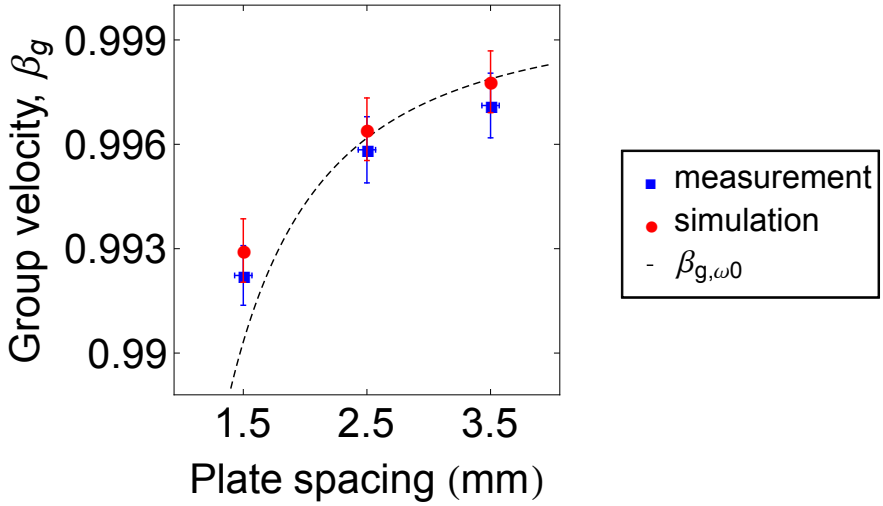

Figure 3.12: Group velocity estimates for three plate spacings determined from EOS measurements before and after the waveguide (blue squares) and simulated propagation of the initial pulse profile (red circles). The theoretical group velocity at the peak frequency of the pulse, .84 THz, is shown by the black dashed line. For the 1.5 mm plate spacing, both measurement and simulation deviate from the group velocity at the peak frequency. This behavior may be explained by the highly nonlinear dispersion at low frequencies which causes a frequency chirp that reduces the contribution of the low frequency components to the pulse envelope peak. The speed of the envelope peak is then determined by the high frequency components, with their correspondingly high group velocities. This figure was reproduced from Ref. [55].

One of the most important practical considerations for this application is the coupling of the THz pulse into one of the necessary higher order modes. In Chapter 2, we discussed in more detail the mechanisms by which the higher order modes in the waveguide could be used to produce a transverse deflection of the electron beam. For our purposes here, we can simplify the scheme to two types of deflection: 1) using a mode with peak longitudinal magnetic field on axis, orthogonal to the transverse motion of the electrons or 2) using an antisymmetric mode profile with an electric field gradient parallel to the transverse motion of the beam.

Ideally, we would use the lowest order mode which achieves the desired profile on axis, because the manipulation necessary to match the incoming THz pulse profile to the mode should be simpler than for higher order modes. Because this allows better coupling efficiency and because lower order modes have larger transverse regions with the same sign of the field, these modes typically have larger peak fields or field gradients available to manipulate the beam. With this in mind, we'll focus on the TE_{11} mode, which provides an antisymmetric mode profile, and the TE_{20}, which provides a longitudinal B-field, peaked on-axis.

In order to match to the TE_{11} and TE_{20} modes, we need regions of the field profile to have opposite sign. To achieve this we proposed inducing a $\lambda/2$ phase shift in the THz field using mirror sections shifted relative to each other by an offset of $\lambda/4$, similar to the method employed by Andonian et al. in the CO_2 streaking experiment [64]. Alternatively, a segmented THz waveplate could be used to approximate the asymmetric orthogonally polarized regions of the TE_{11} mode.

Table 3.1: CPPWG coupling efficiency for THz streaking

	TE_{11} mode	**TE_{11} mode**	**TE_{20} mode**
Coupling technique	waveplate	offset mirror	offset mirror
Coupling efficiency	0.552	0.278	0.638
Resonant plate-spacing	2.65 mm	2.65 mm	1.95 mm
Resonant energy	7.703 MeV	7.703 MeV	6.225 MeV

In Fig. 3.13, we show the set of relevant mode profiles, along with the incident THz electric field profile offering the maximum coupling efficiency based on the manipulation techniques discussed. For each case, the theoretical coupling efficiency and the corresponding beam energy required for resonant interaction is given in Table 3.1. All calculations are based on the undulator parameters fixed by the compression experiment, taking advantage of the same structures used for an alternative application. The incoming THz profiles were simulated using a combination of THz waveplate, mirror offset, or non-reflective coating.

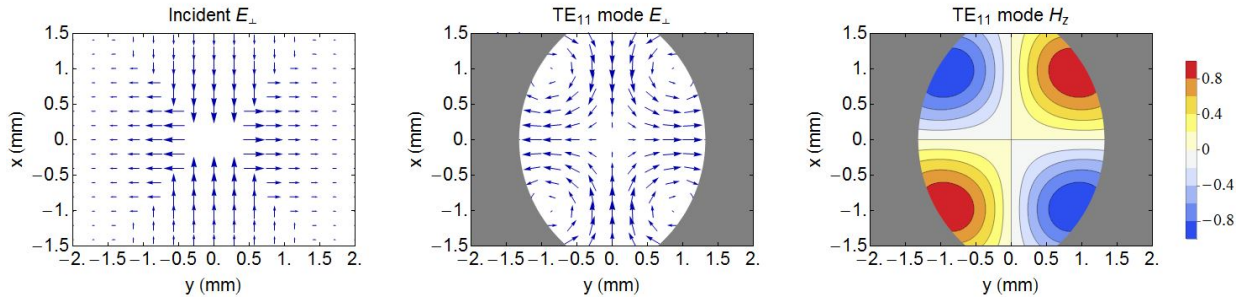

(a)

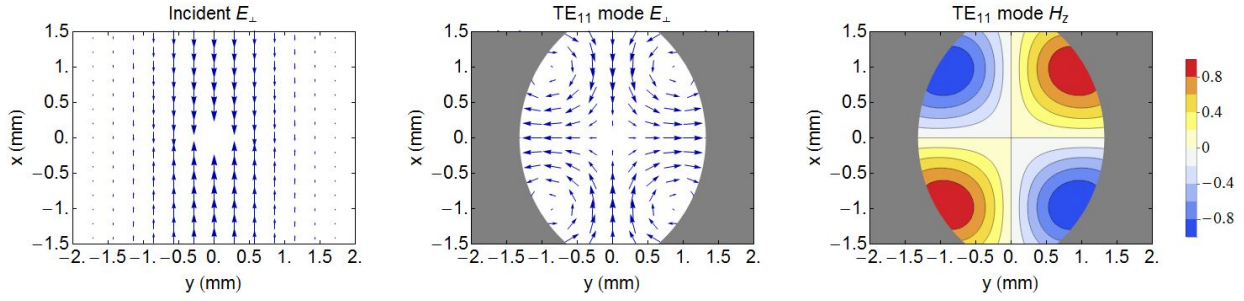

(b)

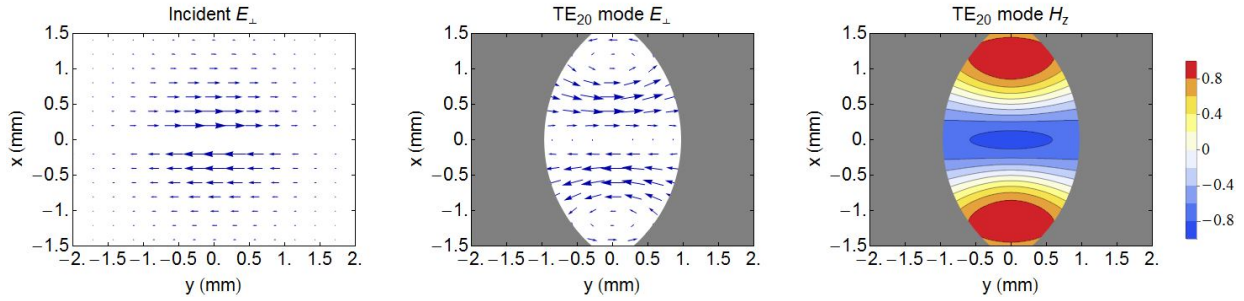

(c)

Figure 3.13: Plots of the transverse mode profile for the (a) TE_{11} mode, coupled using a waveplate, (b) TE_{11} mode, coupled using displaced mirror halves, and (d) TE_{20} mode, showing, from left to right, the incident THz pulse, electric field of the excited mode, and magnetic field of the excited mode.

Work on this project did not advance to the stage of experimental verification of the coupling efficiency. Simulation results discussed in Chapter 2 showed that additional factors may limit the viability of this technique as a THz driven deflection mechanism. At the same time, ground-breaking work has been performed using the field enhancement in split ring resonators to enable an alternative technique for THz-driven beam deflection [25, 26].

3.5 THz detection using photoconductive antennas

Historically, photoconductive antennas (PCA) have provided a valuable tool for both generation and detection in the "THz gap" [18, 77], but the detection capability of these devices has only recently been applied to electron beam diagnostics [78, 79], and the experimental work presented here is the first demonstration of PCA-based direct detection of the transient field produced by a passing electron beam.

The project was initiated by RadiaBeam technologies [80] to develop a user-friendly sub-picosecond beam timing diagnostic, able to meet the synchronization requirements of a laser driven plasma wakefield acceleration scheme [81]. Initial testing was performed using a commercially available PCA to measure the THz field produced by the UCLA benchtop optical rectification source, but this device was deemed unsuitable for the application given its challenging alignment constraints, poor sensitivity, and high noise susceptibility.

The research group led by Prof. Jarrahi in the UCLA Electrical Engineering Department has made pioneering advances in PCA technology, using plasmonics-enhanced large area devices to greatly improve their emission capabilities and detection sensitivity [82, 83], and inspiring our interdisciplinary collaboration at UCLA to develop a plasmonics-enhanced PCA-based electron beam timing diagnostic [84].

PCAs are composed of a metallic antenna deposited on a layer of photoconductive semiconductor that becomes optically activated by a sub-picosecond laser, generating a large carrier population. When operating as a detector, the presence of the THz field on the device drives a current between the arms of the antenna. The large-area (1 mm^2) plasmonics enhanced PCA developed by Yardimci et al [82] incorporates plasmonic contact electrode

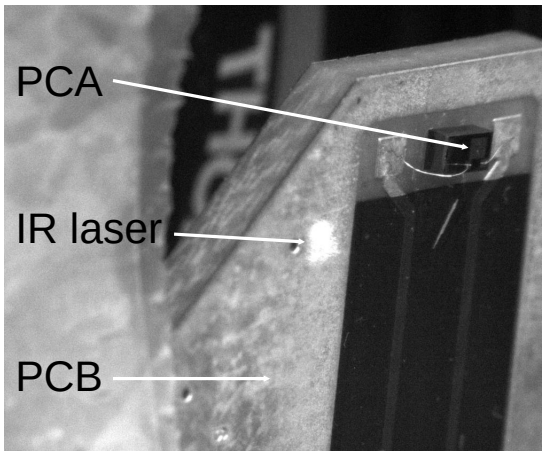

Figure 3.14: Photograph of the PCA mounted on a printed circuit board (PCB), in which the IR laser used to optically excite the photoconductive semiconductor has not yet been aligned onto the antenna.

gratings throughout the active area to improve the device performance by minimizing the path length required for photocarriers to drift to the electrodes, reducing the travel time to a sub-picosecond timescale.

The large area device drastically simplifies the alignment process, and in fact the laser spot size can be even larger than the antenna area, as shown in Fig. 3.14. In addition, the final signal is a sum of the contributions from all regions of the large area device, improving its sensitivity to low intensity THz fields, unlike alternative detection schemes such as EOS. Conventional beam timing diagnostics like button and stripline beam position monitors and RF cavity based schemes have achieved sub-10 fs precision, but the measurements generally require integration over many beam shots and significant bunch charge (hundreds of pC) [85, 86, 87, 88]. Even EOS techniques, which have acheived single-shot measurements down to the 10 fs resolution level [89, 90, 91, 92], still require >10 pC.

In a comparison of THz pulse measurements performed using the PCA and EOS in Fig. 3.15, the PCA demonstrates superior sensitivity, necessary given the low field (few kV/m) expected during beam measurements. The THz source for these measurement is the benchtop optical rectification setup discussed earlier in this chapter. The THz pulse is focused onto the surface of the PCA using an off-axis parabolic mirror (OAP) as shown in Fig. 3.16a.

The IR pulse used to drive the THz source is also used to optically excite the PCA, or probe the ZnTe during the EOS measurements, providing the timing reference that can be adjusted using a delay stage. Ideally, the IR is incident normal to the surface of the PCA with horizontal polarization, but in practice, the IR path had to accommodate the OAP (see Fig. 3.16a). With the IR and THz field coincident on the device, the resulting current is converted to a voltage using a transimpedance amplifier (gain 10^7 and 500 kHz bandwidth) and monitored on a sampling oscilloscope.

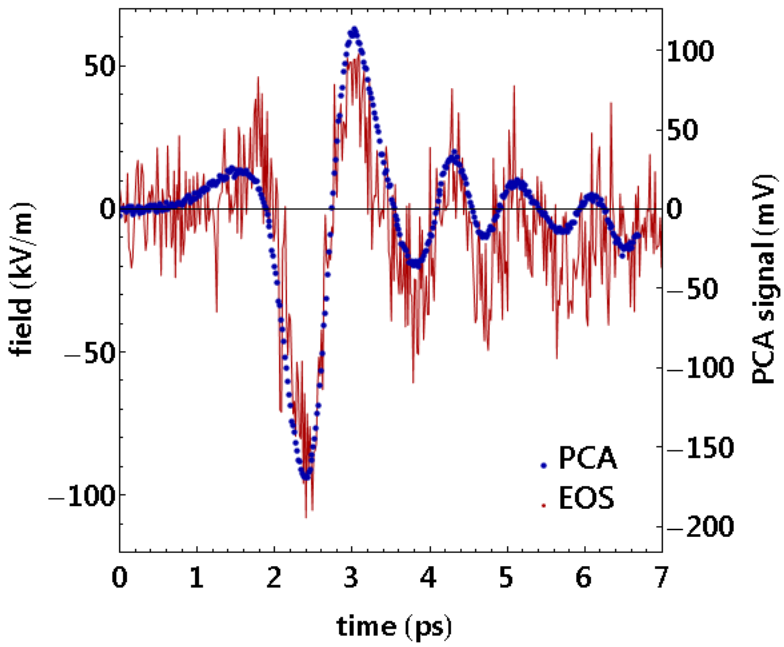

Figure 3.15: A comparison of THz pulse measurements performed with the PCA and with electro-optic sampling (EOS), using the benchtop THz source based on optical rectification.

The version of the PCA geometry used in our timing experiment was designed for a vertically polarized THz field propagating normal to the device surface. The field produced by the relativistic beam has a radially polarized distribution that is compressed in the direction of the beam propagation, forming a "pancake." In order to detect the field of the passing beam in a non-invasive measurement, we position the PCA as shown in Figs. 3.16b and 3.17 with the beam passing above the antenna so that it samples the vertical component of the radial field. Key parameters describing the electron beam and the laser used to optically

excite the PCA are given in Table 3.2.

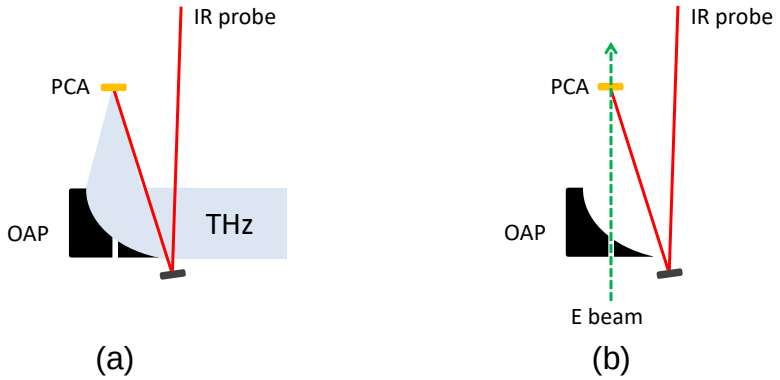

Figure 3.16: Viewed from above in the lab frame, (a) the off axis parabolic mirror (OAP) focuses a THz pulse produced via optical rectification onto the PCA active area, incident normal to the surface. (b) The electron beam passes above the PCA, producing a radial field as shown in Fig. 3.17.

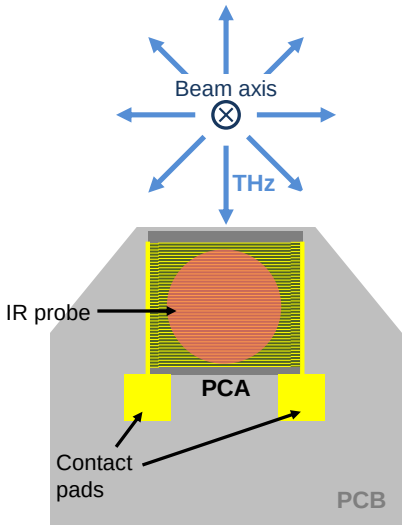

Figure 3.17: Diagram of the photoconductive antenna (PCA). The electron beam passing above (into the page) produces a radially polarized field. The PCA samples the vertical component of the field. The incident IR used to optically excite the semiconductor is horizontally polarized.

During this experiment the PCA was mounted within the vacuum pipe of the beamline

Table 3.2: Experimental Parameters

Electron beam energy	3.3 MeV
Bunch length (RMS)	1 ps
Charge	2-24 pC
Laser spot size	1 mm
Optical pulse wavelength	800 nm
Pulse duration	50 fs
Pulse energy	5 μJ

with the current carried out by a triaxial feedthrough for enhanced shielding from the electromagnetic noise produced by the PEGASUS RF system. Despite our shielding precautions, we still see significant noise in the signal, producing a background level of 200 mV spanning several μs, with the IR pulse alone adding a 50 mV signal on top. The benchtop THz source provided a known reference that we used to optimize our procedure for identifying the detected THz pulse within this signal. We recorded the average of the oscilloscope trace gated with a 1 μs window positioned around the peak of the IR signal alone. At each time step, we collected multiple measurements, which we then averaged, in order to account for fluctuations in the noise as well as timing jitter of the electron beam. (In reality, the PCA could provide a single-shot diagnostic.) We also periodically took measurements with the beam off to establish the background, and then subtracted that value from measurements with the beam on.

In Fig. 3.18, we show a timing scan of PCA measurements of the field produced by the electron beam, in which the timestamp is determined by the IR pulse arrival time relative to the electron beam. We estimate the diagnostic accuracy of this time-dependent response at 0.7 ps, from the ratio of the signal noise, σ_V, to the slope of the leading edge, dV/dt. We expect the field produced by the beam to appear as a single pulse, at a time-of-arrival (TOA) near zero in Fig. 3.18. The source of the prolonged ringing at around 34 GHz is as-yet unidentified, although we believe it is most likely due to reflections of the electromagnetic field within the PCB. Measurements using the interchangeable benchtop THz source also

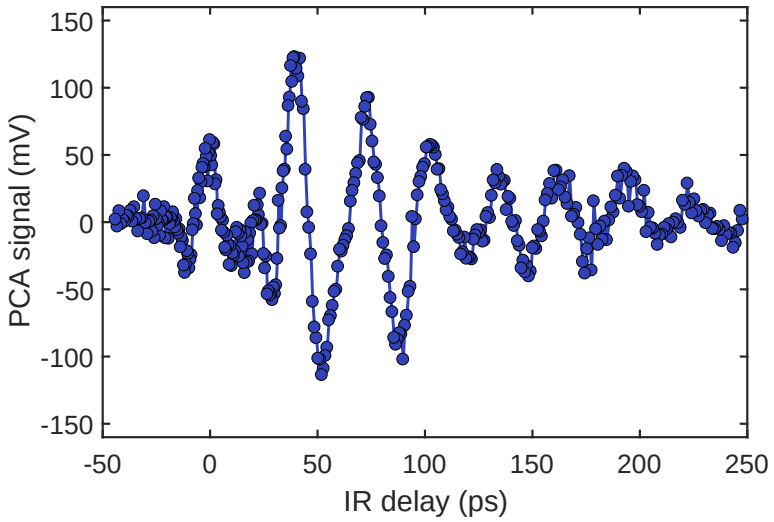

Figure 3.18: PCA signal as a function of IR pulse arrival time, measuring the field produced by a 24 pC electron beam passing about 3.6 mm above the antenna.

indicate significant ringing after the initial peak (not pictured here), which are inconsistent with the known profile of the THz pulse determined from EOS measurements.

To better characterize the capabilities of this PCA-based electron beam diagnostic, we performed additional measurements of the time-dependent signal as a function of both beam charge (Fig. 3.19) and distance between beam axis and antenna (Fig. 3.20). In each case, the peak signal shows the expected scaling with the predicted field. These measurements indicate that the PCA is already sensitive down to very low charge (2 pC), despite being unoptimized for this application, and easily capable of non-invasive measurements with the antenna several millimeters from the beam axis.

The PCA demonstrated this impressive sensitivity while operating in conditions that differ significantly from the original design application. Not only was the THz field radially polarized and incident parallel, rather than normal, to the surface of the device, but the particular PCA we used was originally intended to operate as a THz emitter. These features suggest there is significant room for improvement in the design of the PCA for this application, from simple changes like increasing the area of the device, to more drastic changes like altering the geometry of the nanoantenna array. The PCA could even be designed for sensi-

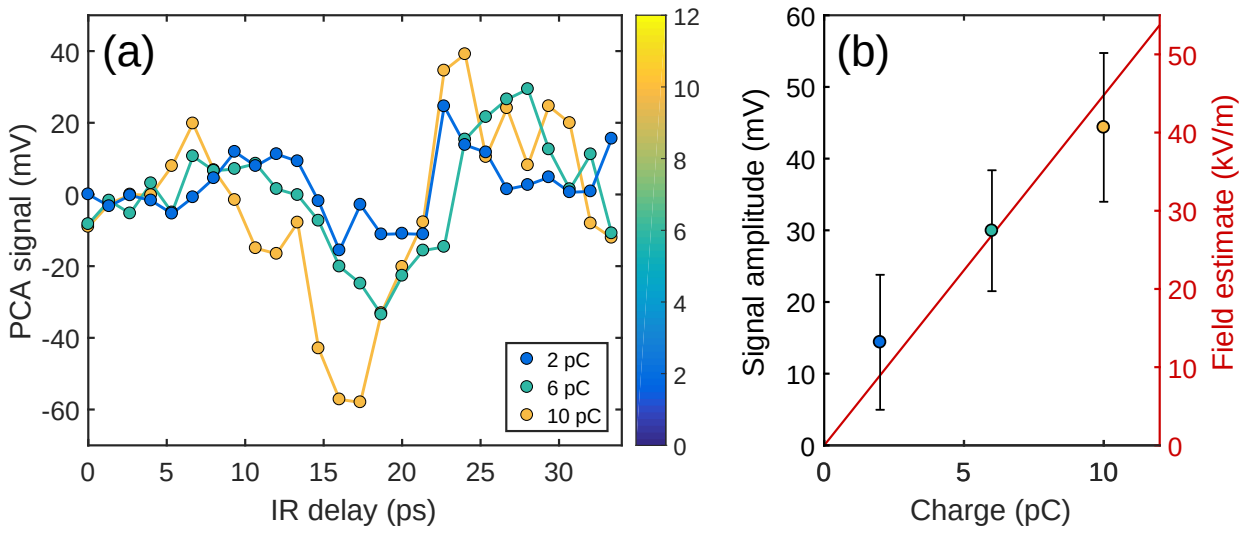

Figure 3.19: (a) The PCA signal as a function of IR pulse arrival time was recorded for varying beam charge, producing (b) a plot of peak signal magnitude as a function of beam charge.

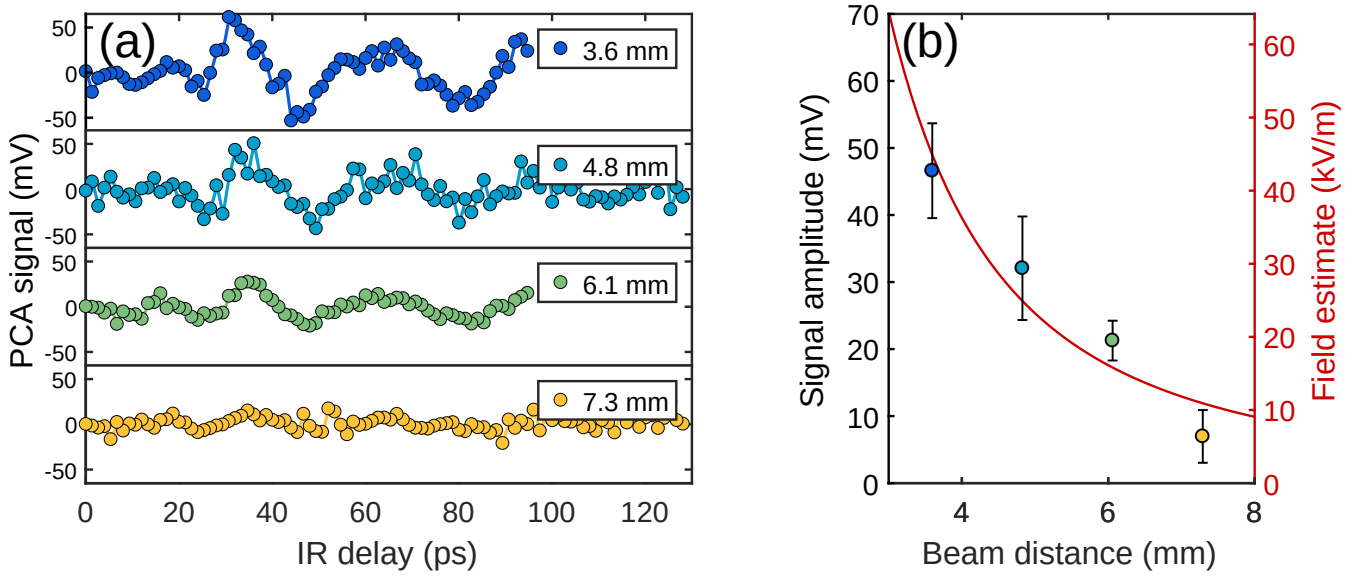

Figure 3.20: (a) The PCA signal as a function of IR pulse arrival time was recorded with the beam passing at different distances from the antenna, producing (b) a plot of peak signal magnitude as a function of beam offset position.

tivity to the radially polarized field, as already demonstrated for non-plasmonics-enhanced devices [94, 95].

With these enhancements, in combination with improvements to the device packaging, the PCA-based beam diagnostic has the potential to achieve sensitivity down to the few 100 fC level, making it a viable timing diagnostic for applications like sub-picosecond resolution ultrafast electron diffraction (UED) experiments [96, 97]. Further applications could incorporate an array of discrete antennas, aligned, for example, transversely to create a beam position monitor, or longitudinally for a single shot measurement of the temporal bunch profile.

CHAPTER 4

THz IFEL Experiment

To test the "zero-slippage" IFEL technique for THz based beam manipulation, we designed an experiment to be performed on the PEGASUS beamline. The beam parameters at PEGASUS are well-suited for IFEL interaction in the THz frequency range. As shown in Fig. 4.1, the resonance condition (Eq. 2.28: $\frac{\omega}{c\beta_z} = k_z + k_u$) dictates that an IFEL operating at 0.8 THz with a few centimeter period requires only a few MeV beam, readily available at PEGASUS, and, as previously discussed, the guiding technique required for "zero-slippage" operation is also well-suited for an IFEL in the THz regime. The length scale of the guiding structure can be large enough to accommodate an electron beam while small enough to fit between undulator magnets with a reasonable magnet gap, factors critical to the design of the undulator and waveguide apparatus.

We will begin our discussion of the THz IFEL experiment with a description of the equipment and setup, including the undulator design and construction process, the beamline, and available diagnostics. We will then review the experimental results (published in Ref. [98]) including a demonstration of the tunable IFEL resonance dictated by the waveguide aperture, as well as the application of the "zero-slippage" IFEL for THz-driven bunch compression. The peak energy modulation recorded during the THz IFEL experiment, 150 keV, includes symmetric energy gain and loss from different regions of the beam interacting with the dispersed THz pulse. The corresponding acceleration (75 keV) is the largest THz-driven energy gain demonstrated to date [23, 27], accomplished with only a 1 μJ THz source.

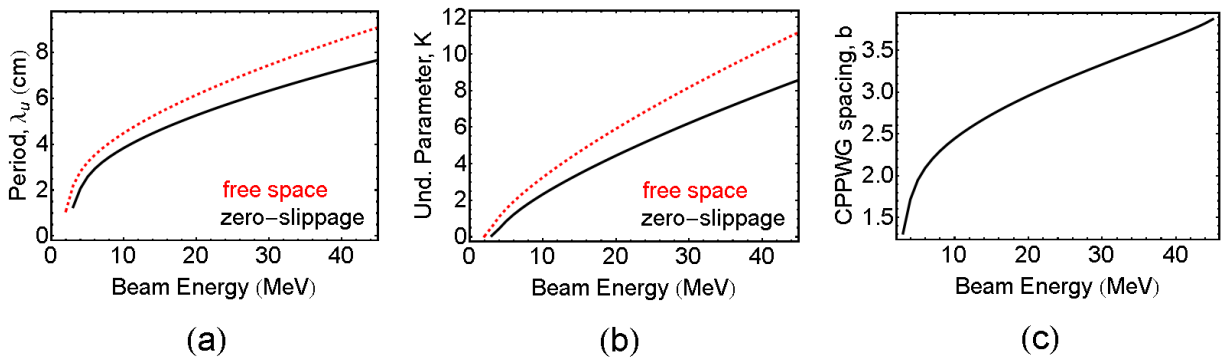

Figure 4.1: (a) The beam energy and corresponding undulator period required for resonant interaction in a planar undulator operating at 0.8 THz, for a free space plane wave (dashed red) and "zero-slippage" (solid black) conditions, assuming a constant 15 mm magnet gap. (b) The corresponding undulator parameter, K, predicted using Eq. 4.1 according to the period and 15 mm magnet gap. (c) The CPPWG spacing required for the "zero-slippage" propagation.

4.1 Guided IFEL design and construction

Figure 4.1 compares the parameters required for IFEL interaction with 0.8 THz in a planar undulator for the free-space case, allowing resonance at a single frequency, and the exact "zero-slippage" velocity matching case. In practice, the addition of the waveguide introduces flexibility in the phase velocity matching condition, such that even once the undulator period is fixed, a range of beam energies can achieve resonant IFEL interaction given the correct waveguide spacing, see Fig. 2.4, but only one of these will be group velocity matched.

In choosing the parameters for the undulator and waveguide construction, we sought to preserve the flexibility of our operating conditions. For example, increasing the maximum range of the CPPWG spacing (we're interested in 1.5-4 mm) requires a compromise with the magnet gap determining the peak magnetic field of the undulator. We used the known quantities, like the frequency of the THz source, the range of accessible beam energies (see Table 4.2), and the amount of space available on the beamline, to narrow in on the optimal parameters.

4.1.1 Undulator design

As discussed in Chapter 2, the wiggling trajectory of the electron beam in the undulator is determined by the undulator parameter, $K = \frac{eB_u}{k_u mc}$, where B_u is the magnetic field amplitude with undulator period $\frac{2\pi}{k_u}$. We limited our design considerations to a planar undulator, as opposed to helical [34], because of the linear polarization of the THz source, and the readily achievable coupling into the TE_{01} mode, which preserves a linear polarization in the vicinity of the beamline axis.

Each period of the undulator is composed of four magnets, arranged in a linear Halbach array, with a complimentary ordering on the opposing side, as shown in Fig. 4.2. The Halbach arrangement minimizes the magnetic field outside the undulator while increasing the amplitude of the near-sinusoidal field on the beamline axis. The undulator builders equation (simplified for a permanent magnet, 4-per-period, planar Halbach array [99]) can help us approximate the magnet gap, g, that will be required to achieve a peak on-axis field of B_u

$$B_u = -1.8 B_r e^{-\pi g/\lambda_u}, \tag{4.1}$$

given an undulator period λ_u and magnet remanence B_r. The period was chosen to be 3 cm with a peak on-axis field, $B_u = .45$ T, requiring a gap of around 15 mm using neodymium magnets (NdFeB) [100] with parameters specified in Table 4.1.

Table 4.1: Undulator magnet specifications

Material	NdFeB	Dimensions:	
Grade	N38UH	Entrance Thickness	3, 3.75 mm
Remanence, B_r	1.23-1.26 T	Regular $\lambda_u/4$ Thickness	7.5 mm
Intrinsic Coercivity, H_{ci}	1592 kA/m	Exit Thickness	7.5, 3.75, 3 mm
Surface processing	Passivation	Cross section	33 × 25 mm
Polarization Tolerance	±5°	Tolerance	±0.07 mm

Once the target field strength and periodicity were determined analytically from Eq. (2.28), the simulation software Radia [101], interfaced with Mathematica, was used to design the

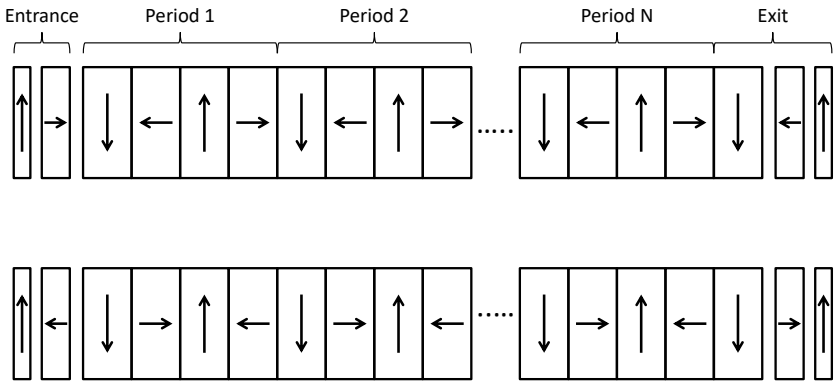

Figure 4.2: The combined linear Halbach arrays enhance the sinusoidal field on-axis, between the arrays of magnets, while the field outside of the arrays is canceled. Specialized entrance and exit sections help the beam transition from a linear to a wiggling trajectory and back, while maintaining an average transverse position still centered on the beam pipe axis [99].

magnetic field map of the undulator. The basic design of the planar undulator used the standard construction of a two-magnet entrance section and three-magnet exit section, with the first magnet of the exit section simply continuing the repeated pattern of the Halbach array (see Fig. 4.2), to force the beam to oscillate about the magnetic axis [99]. To model the undulator in Radia, the size and position of each magnetic block was specified, as shown in Fig. 4.3a, along with the polarization of its magnetic field. Radia used the defined remenance of the magnetic material to then generate a 3-dimensional field map. The model field on-axis is shown in green in Fig. 4.3b with the corresponding electron beam trajectory in Fig. 4.3c.

4.1.1.1 Undulator tuning

To ensure that the magnetic field of the actual constructed undulator could be tuned to match the model generated in Radia, the magnet mounting system required the capability to make fine adjustments to the insertion depth of each magnet. The individual magnets were glued into holders using vacuum-compatible adhesive, with an additional piece of aluminum used as a retaining cap partially covering the end of the magnet. A cross section of the

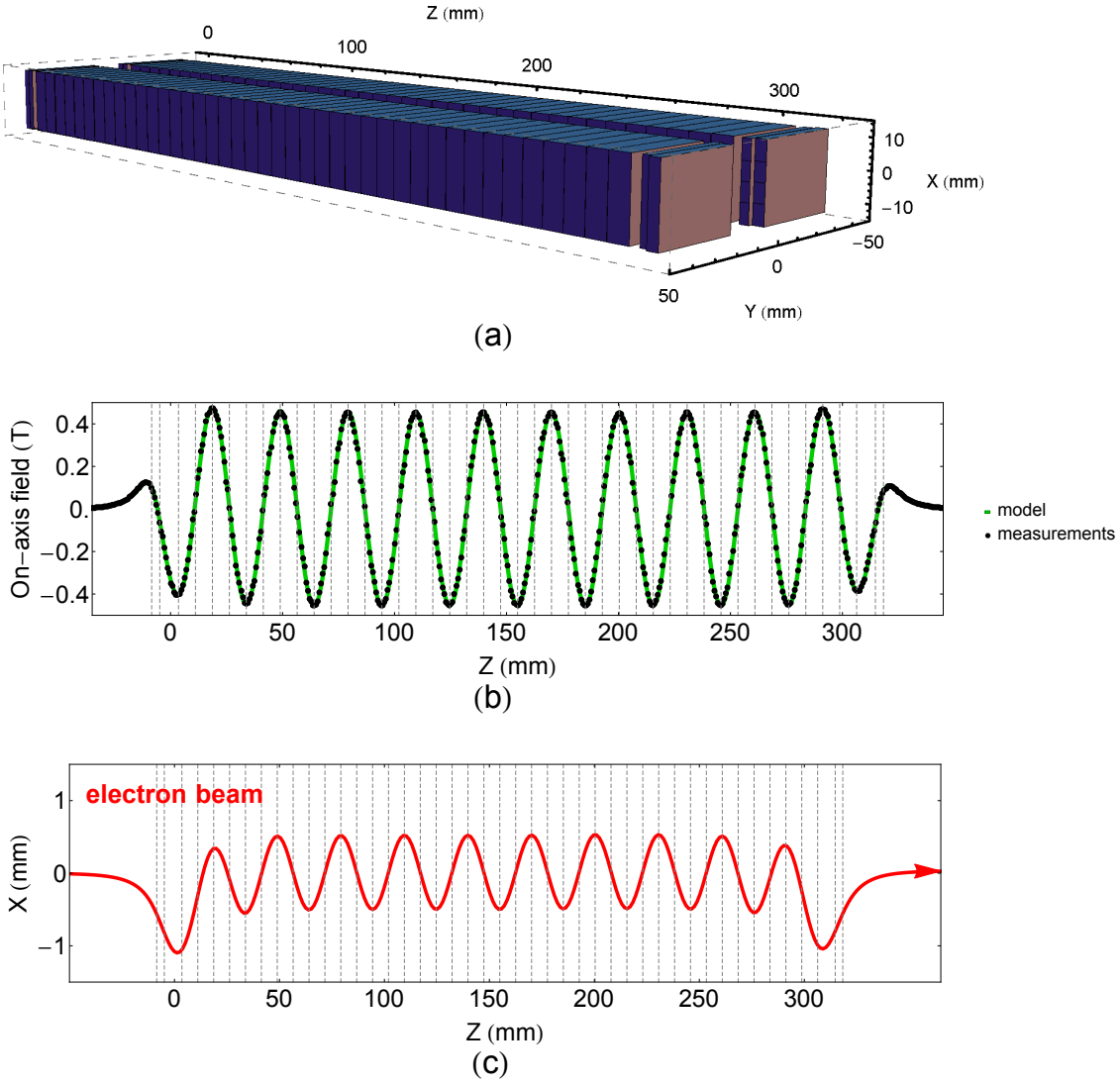

Figure 4.3: (a) 3-dimensional model of the undulator with magnetic block position and size (and polarization not shown) specified. (b) The corresponding on-axis magnetic field map (green) generated in Radia was used to tune the undulator with Hall probe measurements (black) of the on-axis field. (c) The electron beam trajectory predicted by Radia for the given field map.

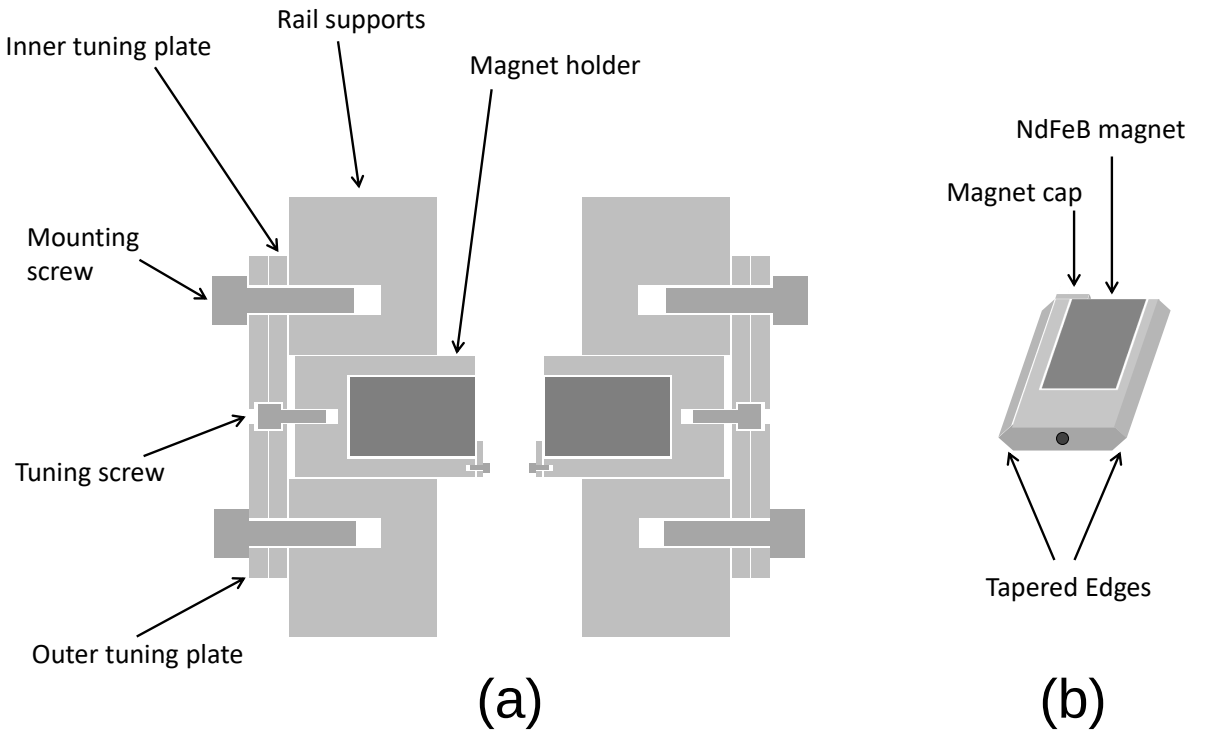

Figure 4.4: (a) Diagram of the undulator cross section showing tuning plates and magnet holders. Teeth in the rail supports (not shown) separate individual magnet holders, holding them in place such that a turn of the tuning screw forces a change in the insertion depth of the magnet holder. Except for the entrance and exit section, each set of (inner and outer) tuning plates supports 4 magnets on each side, making up a full period. (b) 3-D illustration of a single magnet in its holder.

magnet mounting design is shown in Fig. 4.4 along with a 3-D rendering of a single magnet holder.

The on-axis magnetic field profile was optimized by iterative adjustments to the gap between individual magnets, guided by the field map modeled in Radia. Between each round of tuning, a Hall probe measured the transverse magnetic field between magnets as a function of longitudinal position, see Fig. 4.5. The final round of on-axis Hall probe measurements are shown overlaid on the Radia field map in Fig. 4.3b.

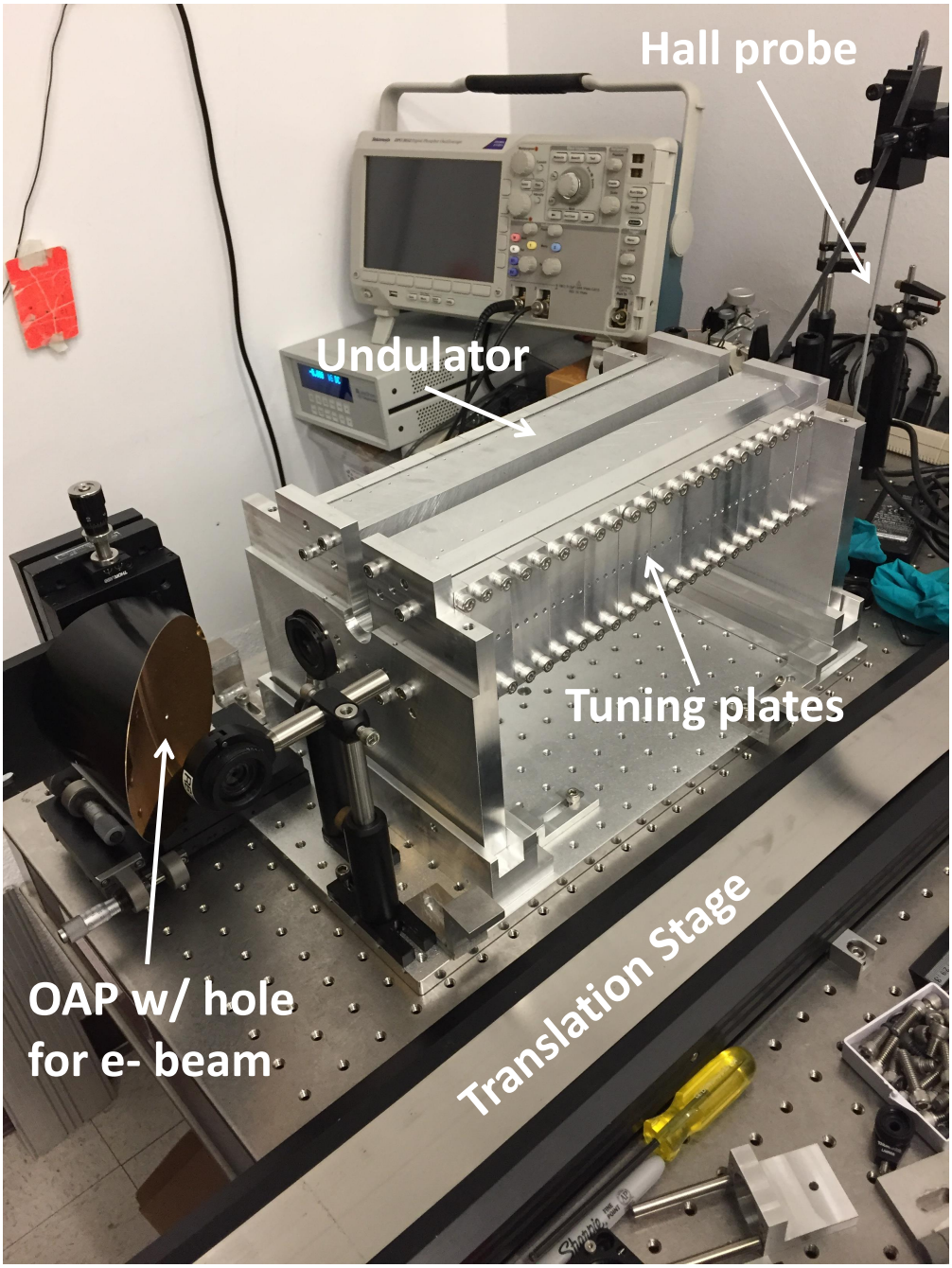

Figure 4.5: Photograph taken during the process of undulator tuning. The Hall probe was mounted to a large translation stage with the probe tip accessing the beam-axis from above. The transverse alignment was controlled by a smaller stage with manual micrometer adjustment which measured displacement from the beam axis. A series of scans measured the transverse magnetic field as a function of longitudinal position within the undulator, followed by iterative adjustment of the tuning plates.

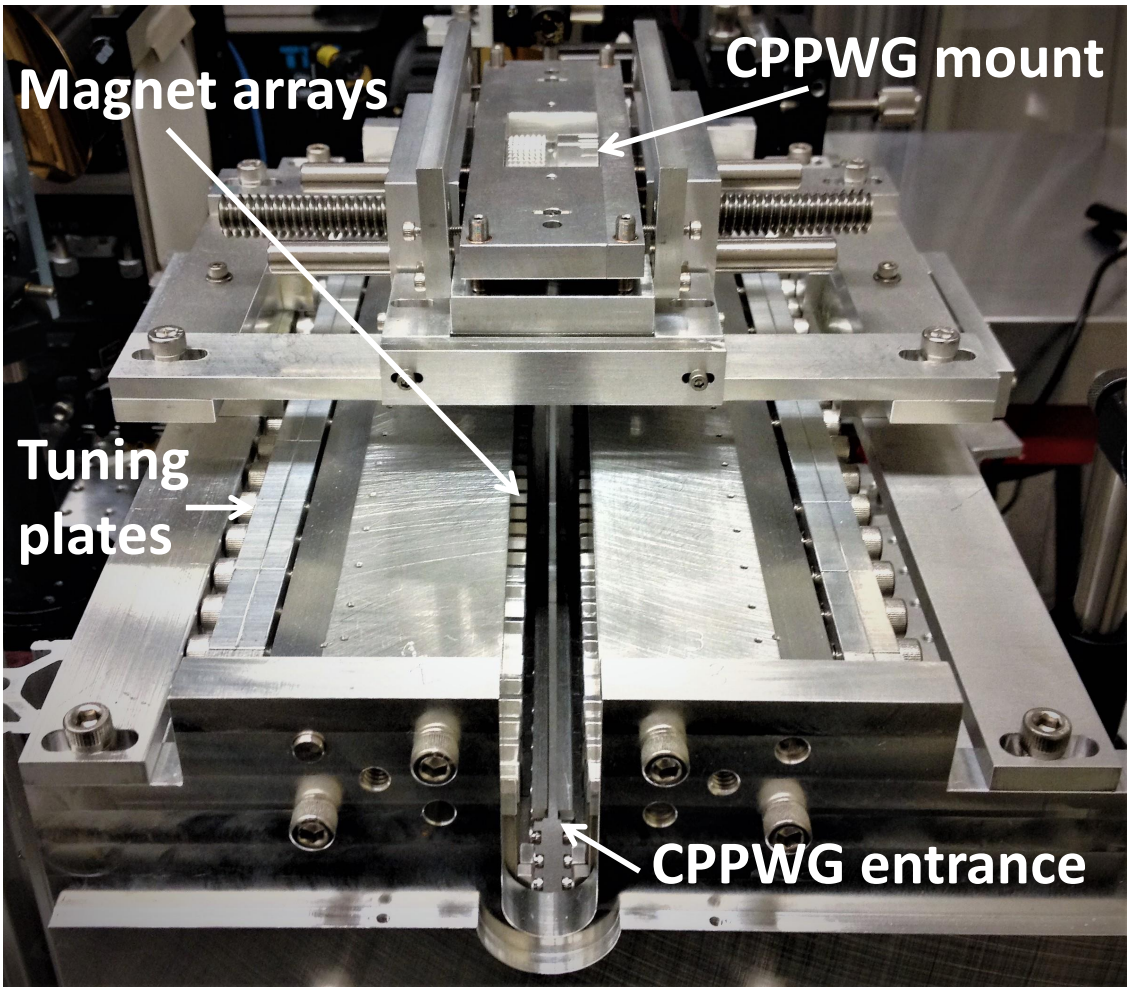

Figure 4.6: Photograph of the undulator with CPPWG plates suspended in the magnet gap by the self-centering mount.

4.1.2 CPPWG and mount design

After the Hall probe measurements requiring vertical access to the beam axis were complete, a laser pointer was aligned onto the Hall probe tip parallel to the longitudinal axis to provide an alignment reference. The CPPWG mount, including pre-attached plates, was then fixed to the top of the undulator, as shown in Fig. 4.6. The CPPWG plates were connected to a specially designed, self-centering mount with built-in adjustments enabling control of 3-D translation, pitch, yaw, and roll. With these controls, the CPPWG position was adjusted until the alignment laser was centered between plates at both the entrance and exit of the waveguide. Dynamic tuning of the plate spacing was then accomplished using a single knob in the center of the mount.

Once the combined undulator-CPPWG apparatus was moved into the vacuum box on the PEGASUS beamline, a HeNe reference laser passing through the waveguide axis was used to assure alignment with the beam axis.

4.2 PEGASUS Beamline: Experimental setup

At PEGASUS, the same Ti:Sapphire laser pulse (>2 mJ) is used to produce both the THz pulse and the UV pulse for electron beam generation in the photogun, facilitating inherent synchronization between the THz pulse and electron beam in subsequent interactions. This advantageous feature comes with the caveat that electron beam time-of-arrival (TOA) suffers from timing jitter due to the RF system, as we will see in our experimental results.

4.2.1 THz generation

The components of the THz source itself were discussed in detail in Chapter 3. For the THz-IFEL experiment, the footprint of the optical breadboard holding the THz optics needed to be decreased and moved into the small space available next to the vacuum chamber in which the interaction would occur, as shown in Fig. 4.7, posing new challenges for the IR path leading up to the THz source. In particular, because the path length was significantly

longer (>10 m) and included several more reflections off of intermediary mirrors, the IR pulse reaching the THz source suffered from pulse energy attenuation and the formation of hot spots in the intensity profile which could have damaged the THz optics. To prevent the formation of hot spots in the beam profile, we reduced the local intensity of the laser by transporting the IR pulse to the THz source in an under-compressed state.

The Ti:Sapphire laser system at PEGASUS uses the technique of chirped pulse amplification exactly because of the destructive self-focusing that occurs at high intensities. The components of the Legend-F laser amplifier include an optical pulse stretcher, a regenerative amplifier, and an optical pulse compressor. The IR pulse entering the system becomes positively chirped in the stretcher, increasing the beam length and thereby decreasing the beam brightness. After amplification, the compressor is used to reduce the IR pulse length, counteracting the positive chirp imparted by the stretcher to achieve nearly the same short beam duration as the original seed.

With our modified scheme, we adjusted the compressor setting to only partially compress the amplified pulse, resulting in a lower-brightness output retaining a slightly positive chirp that did not exhibit self-focusing. The frequency chirp of the IR pulse changed the pulse-front-tilt angle coming off the grating in the THz source set-up, potentially reducing the conversion efficiency, but this effect could be compensated by adjusting the grating angle, along with the routine steps of optimization used for the THz source optical alignment.

We consistently measured >1 mJ of IR reaching the THz source, despite splitting the laser for simultaneous UV generation, ensuring a 1 μJ THz pulse given our $\sim 0.1\%$ conversion efficiency. For the IFEL configuration, only a small bunch charge (few 100 fC) was necessary to demonstrate the effect on the beam phase space, so the UV pulse energy could be reduced in favor of more IR driving the THz source.

4.2.1.1 THz alignment

Since the pyroelectric detectors previously used to identify the THz focal point were too large to fit at the entrance to the waveguide, EOS measurements with the ZnTe crystal at

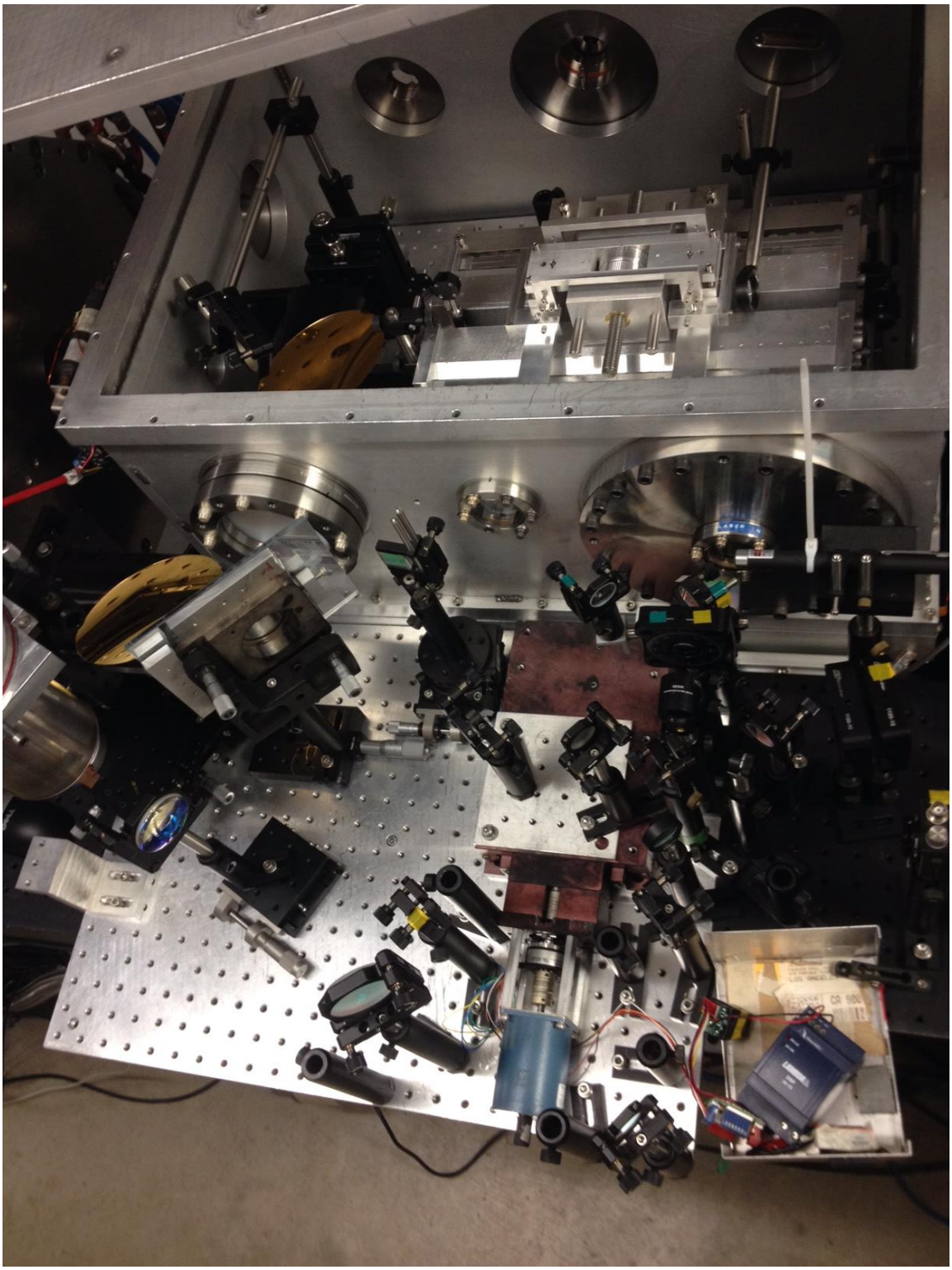

Figure 4.7: Photograph of THz source next to the vacuum box, with the undulator inside.

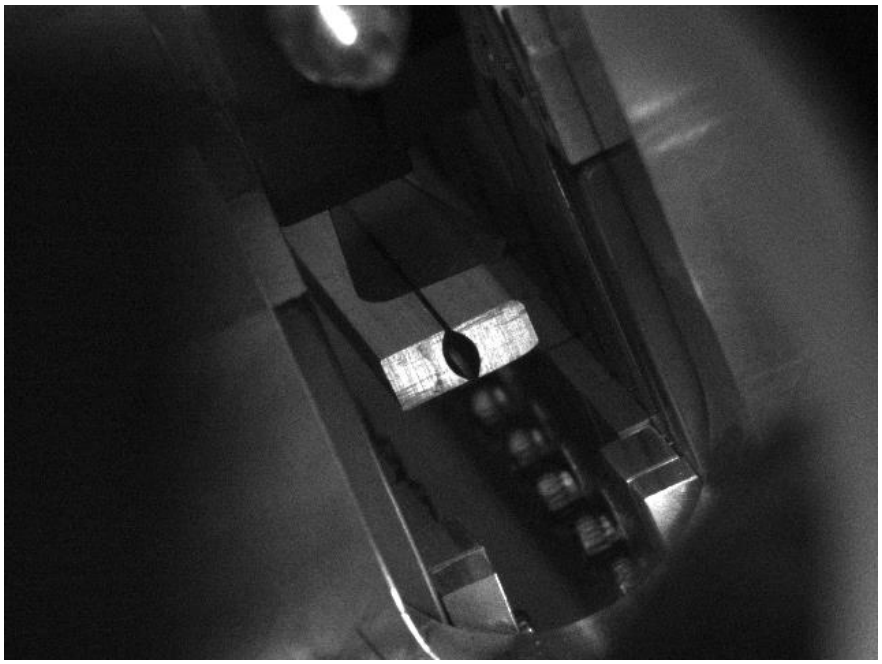

Figure 4.8: Photograph of the entrance to the CPPWG and undulator. The ZnTe crystal used for EOS measurements to optimize THz alignment into the waveguide is currently withdrawn above the beam axis, so that the beam can be transmitted through the waveguide.

the entrance to the waveguide (see Fig. 4.8) provided a check on the THz alignment into the CPPWG. The IR probe line already built into the THz source setup was extended into the vacuum box where a removable mirror behind the OAP, aligned the IR through the hole and on through the waveguide.

Unfortunately, any mirror adjustment that brought the THz into better spatial alignment could simultaneously change the path length and therefore the temporal alignment which reduced the apparent signal. To account for this effect, any change to mirror alignment was followed by a manual scan of the temporal overlap to find the local maximum in THz signal.

4.2.2 UV generation

To produce the UV used on the photocathode in the RF gun, the initial Ti:Sapphire laser pulse undergoes a cascaded process beginning with frequency doubling of the input 800 nm light in a nonlinear crystal. The resulting output of 400 nm light and unconverted 800 nm

light is split and then recombined for sum frequency generation in a second nonlinear crystal to produce a pulse at 266 nm.

The slight positive frequency chirp that was left on the initial laser pulse in order to help with self-focusing during the transport to the THz source was detrimental to the UV conversion efficiency. The chirp was corrected using a dispersive medium placed upstream of the first frequency doubling stage. For this application, we chose a relatively long (75 mm) fused silica light pipe, with the greater distance able to compensate for a larger positive chirp.

The length of the UV pulse plays an important role in determining the length of the electron beam produced by the RF gun. At the exit of the the gun, the bunch length is proportional to the laser pulse length, along with the compression factor of the gun determined by injection phase (typically of order unity for our operating regime). In the initial phase of the THz IFEL experiment, we chose to stretch the UV pulse (from <100 fs rms to >1 ps rms) in order to obtain a long electron beam. This increased the window of timing overlap in which we would be able to see some IFEL interaction and greatly reduced the significance of electron beam TOA jitter. The UV pulse was stretched using multiple passes through a prism-retroreflector system which dramatically increased (>7 m) the pathlength traveled by the UV pulse to reach the cathode in the RF gun.

4.2.2.1 Timing

In order to achieve the appropriate timing for IFEL interaction, we need the UV path length to be just enough shorter than the THz path length in order to account for the electron beam travel time from the gun to the undulator, so that electron beam and THz arrive at the device simultaneously. To check the relative pathlength of the UV and the THz, we used one photodiode to measure the UV where it entered the photogun, and a second photodiode to measure the IR probe before it entered the ZnTe (placed at the entrance to the CPPWG for EOS alignment measurements). Simultaneously viewing both signals on an oscilloscope provided a relative timing measurement that included the signal propagation time in the

coaxial cables used. To identify and cancel out that contribution, the measurement was repeated with the coaxial cables leading to each photodiode swapped. Using this method, we matched our estimated travel time, for the subsequent UV path to first reach the cathode and then the generated electron beam to reach the undulator, to within a fraction of a nanosecond.

4.2.3 Electron beam

Much of the ground-breaking research at PEGASUS laboratory has centered on the creation of high-brightness electron beams, exploring the frontier of ultrashort, ultralow emittance, low charge electron beams [102, 103, 104, 105, 65] and applying those beams towards experiments in ultrafast electron diffraction and microscopy [106, 107, 108]. The high field gradient of the UCLA/BNL/SLAC type 1.6 cell S-band (2.856 GHz) photoinjector design [44] quickly brings the beam up to relativistic energies, reducing the effects of space charge repulsion (force decreases $\propto 1/\gamma^2$), and in combination with the solenoid field used for emittance compensation and focusing, produces a high peak current, low transverse emittance electron bunch at energies up to 4 MeV. With the additional 11 cell S-band booster linac, the beam energy can be brought up to 10 MeV. A simple diagram of components on the PEGASUS beamline, preceding the THz IFEL interaction point is shown in Fig. 4.9. Table 4.2 gives the range of typical beam parameters used during operation of the THz IFEL.

Table 4.2: PEGASUS beam parameters

Beam energy	3-10 MeV
Charge	10 fC-10 pC
Energy spread	0.5 %
Transverse emittance ε_n	100 nm·rad
Bunch length	100 fs-2 ps

For IFEL and FEL interaction in the THz frequency regime, the requirements for transverse beam emittance are relatively lenient compared to typical FEL parameters, because

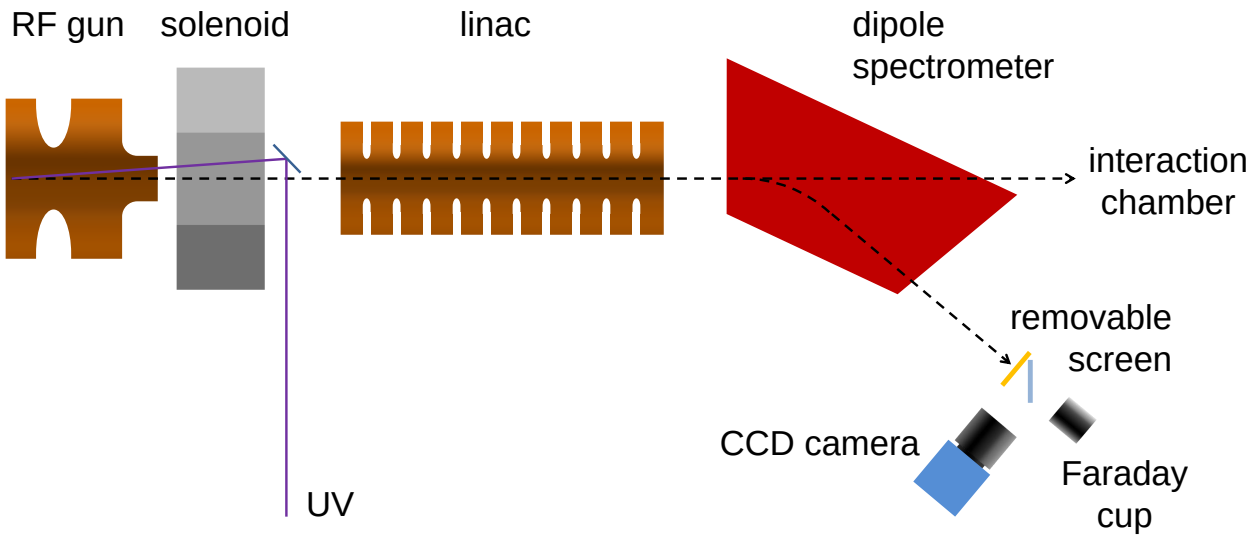

Figure 4.9: Diagram showing the primary components of the PEGASUS beamline, not to scale, leading up to the THz IFEL interaction. Depending on the current in the dipole spectrometer, the beam can continue straight for further interaction, or be bent onto a trajectory for energy and charge measurements.

the resonant wavelength is larger by more than an order of magnitude, i.e. when operating at laser frequencies, the waist size is much smaller than in the THz regime. The need for spatial overlap in an IFEL constrains the transverse emittance of the electron beam. If the beam size becomes comparable to the laser waist, there may be significant particle detrapping. For our simulation work, however, this was not the case and the transverse emittance could be reasonably neglected, justifying the use of a 1 dimensional simulation model.

In the long beam configuration used for the first stage of the THz IFEL experiment we expect to see nonlinear longitudinal phase space correlations, referred to as RF curvature, in the electron beam as the bunch length is not negligible compared to the length scale of the RF wave used to accelerate the beam.

4.2.3.1 Alignment and transport

During the course of daily operation, we control the amount of charge produced at the photocathode by remotely adjusting the UV pulse energy. To monitor the beam position, YAG:Ce screens are inserted into the beam pipe and viewed with CCD cameras placed at windows located at strategic positions along the beamline. Steering magnets along with focusing by the first solenoid ensure that the beam does not clip on the linac.

The beam energy after acceleration in the linac but before interaction with the THz pulse is determined using a magnetic spectrometer which bends the beam path, as shown in Fig. 4.9, dispersing the electrons according to their energy. The electron energies can be determined from the knowledge of the magnetic field and their trajectories [49]. The calibration for this particular spectrometer at PEGASUS relates the current, I (amps), used in the electromagnetic dipole to bend the beam to the beam energy via the formula $\beta\gamma = -5.4I$.

The profile of the beam at the spectrometer can also be used to retrieve the energy spread of the beam. For this spectrometer (upstream of the interaction chamber), 100 pixels corresponds to 1% relative energy spread. The conditions for maximum energy and minimum relative energy spread can be used to verify the linac phase. Running on-crest in

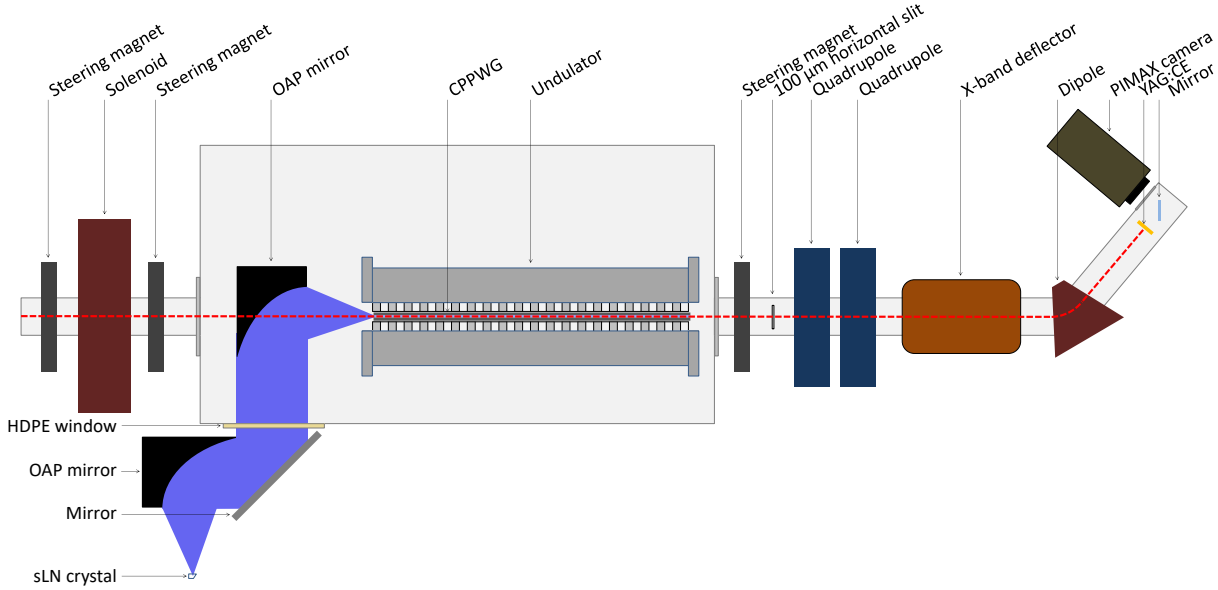

Figure 4.10: Diagram of the interaction chamber and subsequent beam diagnostics for the THz IFEL experiment at PEGASUS. This figure is reproduced from our publication, Ref. [98].

the linac should give the maximum acceleration, resulting in the largest beam energy on the spectrometer. Due to the rf curvature in the LPS of the beam coming out of the gun, the minimum energy spread is obtained when the linac is run at a phase slightly off-crest, such that it imparts a small energy chirp, in addition to the acceleration, which counteracts the initial LPS curvature. To use the linac as a bunching cavity, the phase can be tuned to a zero-crossing which imparts a large energy chirp resulting in subsequent velocity bunching [65]. This feature was essential to the THz FEL experiment discussed in the next chapter.

The redirection of the beam path caused by the spectrometer allows beam charge measurements using a Faraday cup placed behind the removable spectrometer screen. For interaction in the THz IFEL, the spectrometer current is reduced to nearly zero, such that the beam bypasses the initial set of diagnostics.

A diagram of the THz IFEL set-up and subsequent beam diagnostics is shown in Fig. 4.10. Steering magnets and a second solenoid were used to focus and align the beam through the hole in the OAP and into the entrance of the CPPWG. To monitor the beam position, a

Figure 4.11: Photograph of the entrance to the CPPWG and undulator. The pieces of DRZ attached to the end fluoresce when exposed to the electron beam, providing a reference when focusing and steering the beam into the CPPWG aperture.

small scintillating "DRZ" screen was attached to the end of the CPPWG, as shown in Fig. 4.11, which fluoresced when exposed to the beam.

4.2.3.2 Diagnostics

After the beam exits the undulator, there are a series of diagnostics available on the PEGASUS beamline. To simply confirm that the beam has passed through the undulator, an insertable YAG screen is placed at a cross after the box for viewing the beam. The primary measurement used to identify and characterize the IFEL interaction was the relative energy spread in the beam. This measurement was performed using a second spectrometer dipole at the end of the beamline, pictured in the foreground of Fig. 4.12. The dispersed beam was viewed on a YAG screen using a PI-MAX intensified CCD camera, with an energy resolution of about 0.6 keV per pixel.

To improve the resolution of our measurements a pair of quadrupoles minimize the betatron beam size on the final screen. For the energy measurement alone, the vertical beam size is irrelevant and focusing is only necessary in the horizontal direction, i.e. the plane in which

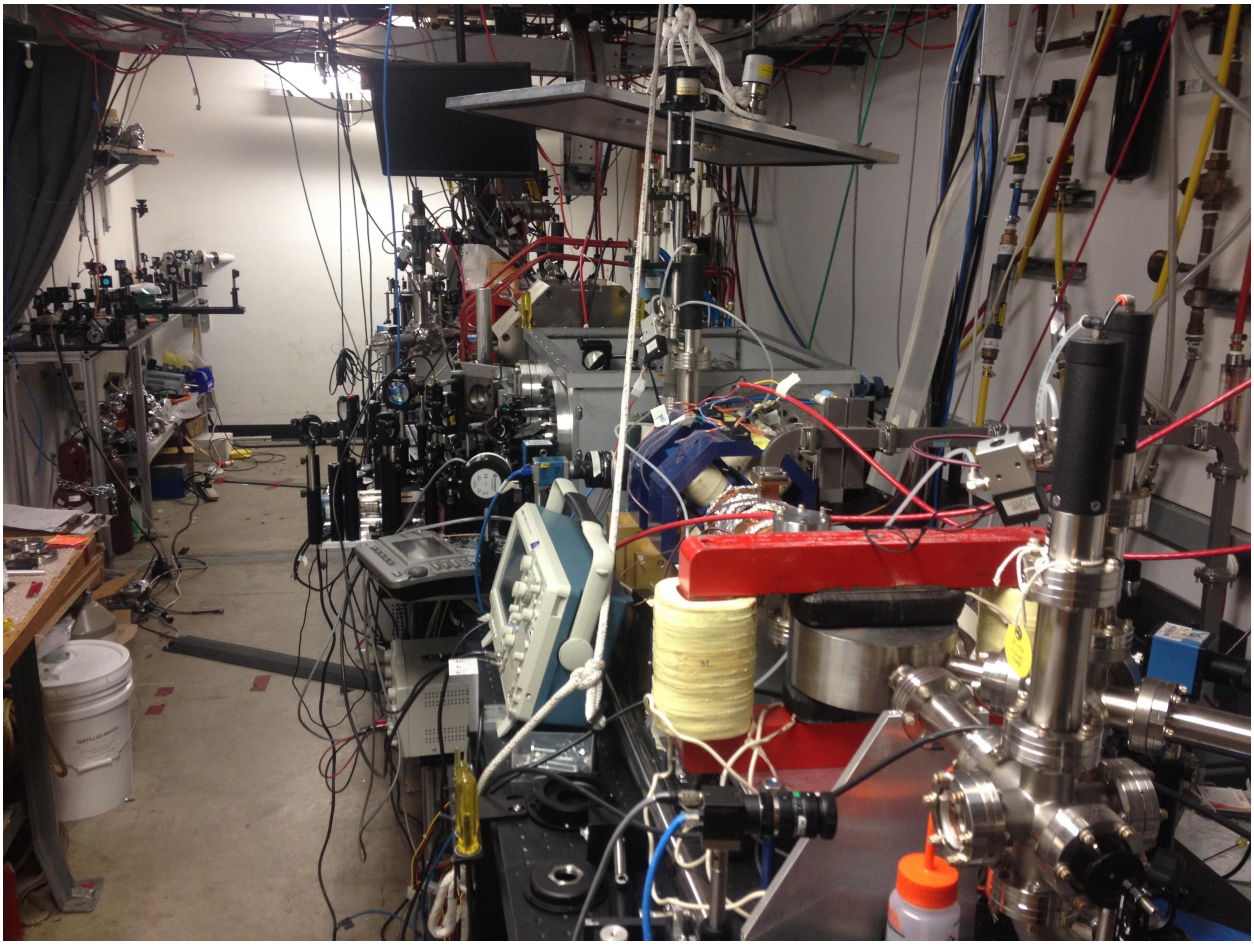

Figure 4.12: Photograph of the PEGASUS beamline. The large vacuum box in which THz IFEL interactions takes place is shown with the lid open. Post-interaction diagnostics including X-band deflector and dipole spectrometer are visible in the foreground.

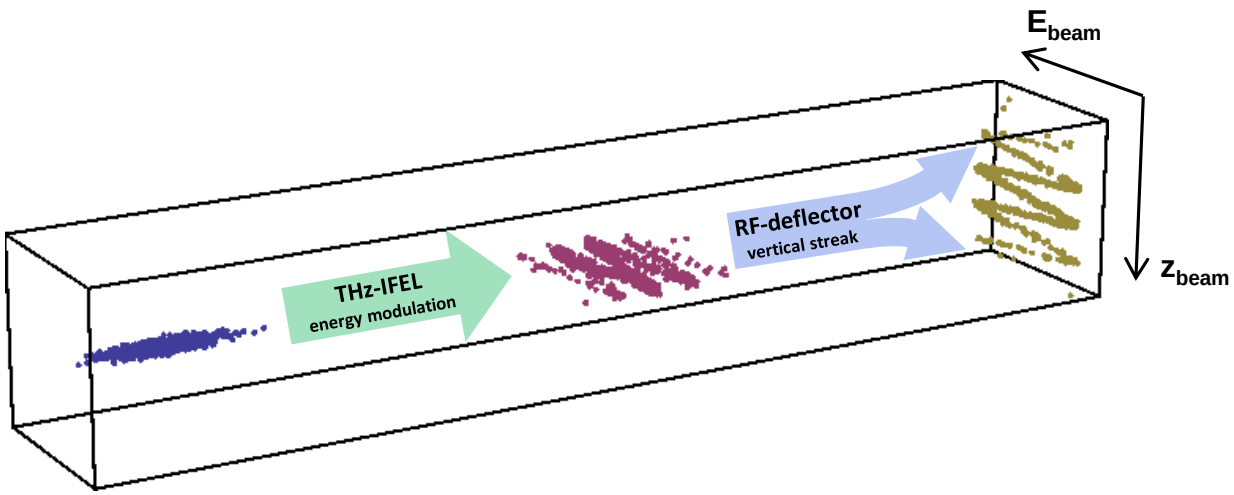

Figure 4.13: 3 visualization of the streaking diagnostic.

the bending magnet disperses the beam. However, in addition to the dipole spectrometer, an X-band deflecting cavity can be used to streak the beam longitudinal profile onto the vertical axis, as illustrated in Fig. 4.13.

The vertical kick imparted to the beam as it traverses the 9 cell 9.6 GHz deflector cavity is accompanied by an increase in the energy spread. This effect is described by the Panofsky-Wenzel theorem

$$\frac{\partial \Delta \mathbf{p}_\perp}{\partial z} = \nabla_\perp \Delta \mathrm{p}_z \tag{4.2}$$

which states that the longitudinal gradient of the transverse force, giving the longitudinal-position-dependent momentum kick, is proportional to the transverse gradient of the longitudinal force which results in a transverse-position-dependent energy change. To minimize this effect we use a 100 μm horizontal slit before the cavity, which limits the vertical size of the beam as it passes through the deflector, such that the induced energy spread is < 10 keV. The cavity is powered with a 50 kW klystron and can impart a transverse deflecting voltage of up to 500 keV. With the deflector on, the quadrupole doublet is used to focus both the vertical and horizontal beam size on the final screen.

4.3 THz IFEL measurements

The initial goals of the THz IFEL experiment included both proof-of-principle measurements showing a "zero-slippage" interaction and demonstration of the practical application for electron bunch compression. The experimental run progressed in the corresponding order, beginning with a focus on the primary indication of IFEL interaction, that is, the increase in beam energy spread caused by the IFEL induced energy chirp on the beam.

To identify the timing overlap, the beam energy distribution was initially monitored while scanning the THz pulse arrival time, with beamline operators looking for changes to the energy spread, i.e. increase in the horizontal width of the beam, to indicate interaction. The change in energy spread was easily recognizable once the timing overlap was established. The example images in Fig. 4.14 show consecutive shots with THz off and THz on while synchronized with the beam.

The "THz off" distribution in Fig. 4.14b shows a slight correlation between horizontal and vertical position, most likely due to the steering of the beam through the quadrupoles. In some images, this effect can be quite pronounced, resulting in an overestimate of the beam energy spread, if we simply projected the beam distribution onto the energy axis. Instead, when analyzing the images we look at thin horizontal slices at different vertical positions along the beam, as shown in Fig. 4.15.

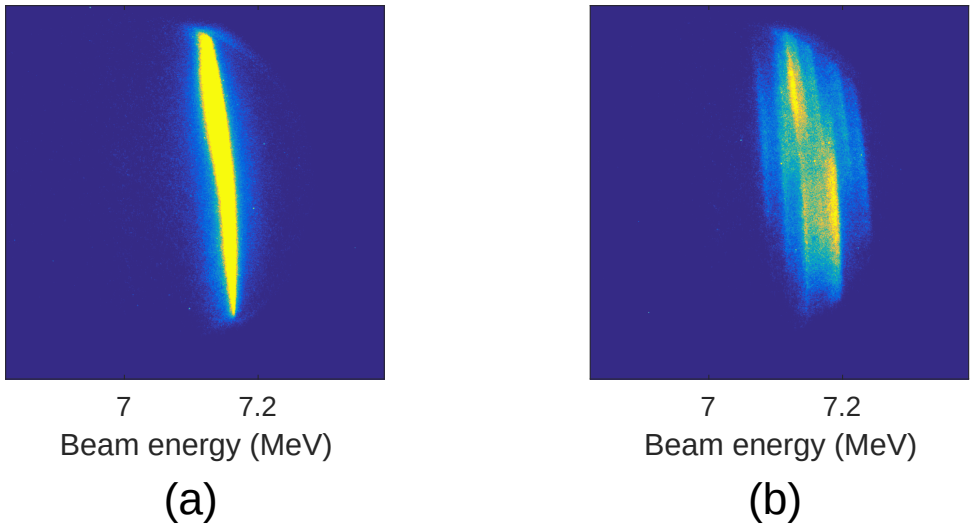

Figure 4.14: Consecutive beam images with (a) THz off and (b) THz on, showing the change in energy spread after IFEL interaction. The beam distribution along the x-axis corresponds to energy after horizontal deflection in a dipole spectrometer. These figures are reproduced from our publication, Ref. [98].

Within these slices the energy distribution indicated by the pixel sum was projected onto the horizontal energy axis, producing plots like those shown in Fig. 4.16b and c. The energy spread was then quantified by the full width at full maximum (FWFM), which in practice we defined as the width at 10% of the peak value.

At each step of the translation stage used to control the path length of the IR driving the THz source, several images were taken with the THz blocked from entering the waveguide, followed by several images in which the THz was present for interaction. This continuous monitoring of the electron beam energy distribution was necessary because factors like pointing fluctuations and RF phase drift could change the apparent background energy spread over time. These measurements, recorded as a function of THz arrival time, produce a timing scan as shown in Fig. 4.16a, identifying the optimal THz and electron beam synchronization.

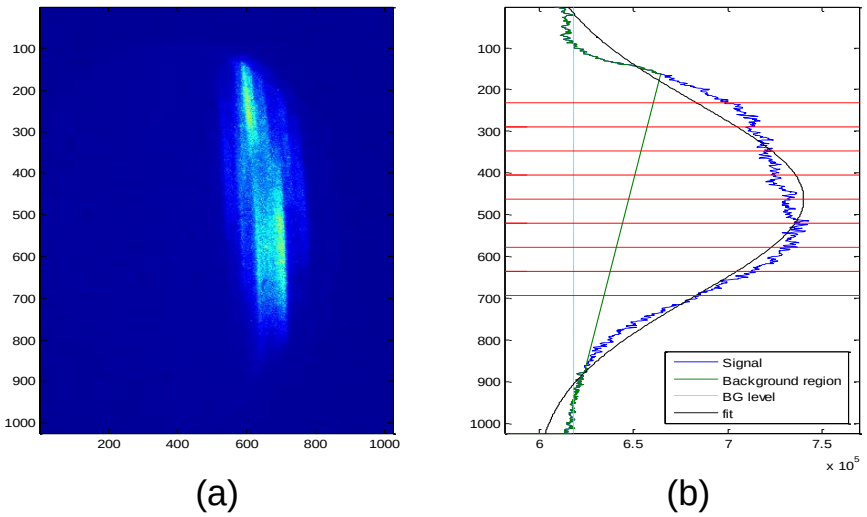

Figure 4.15: The beam distribution shown in (a) is projected onto the vertical axis in (b) in terms of the vertical pixel number, with the pixel sum on the x-axis. The green line indicates the "background region" of pixel sums used to determine the background threshold (light blue). A Gaussian fit of the vertical beam distribution then establishes the vertical position and thickness of the slices ($\sigma/4$ pixels, red dividing lines) used when calculating the full width at full maximum (FWFM) of the beam distribution.

In Fig. 4.16a, we see the window of timing overlap is quite large, with a FWHM of nearly 4 ps and evidence of interaction over a full 20 ps range. This result is consistent with our expectation that the initial near-single cycle THz pulse is dispersed into a multicycle waveform, approaching 20 ps long by the end of the CPPWG. This "long" THz pulse is only available for a short interaction distance however, since it required propagation through most of the waveguide to develop, resulting in significantly smaller energy modulation.

The choice of FWFM characterization stems from the structure of the energy distribution produced by IFEL interaction with the long beam. Two key features visible in the "THz on" shot in Fig. 4.14 are 1) the symmetrical increase in the energy spread and 2) the vertical streaks within the beam distribution that look like bands in the energy distribution. This produces the sort of stepped energy distribution that we see in Fig. 4.16b, that remains centered at the same energy as the "THz off" distribution shown in Fig. 4.16c.

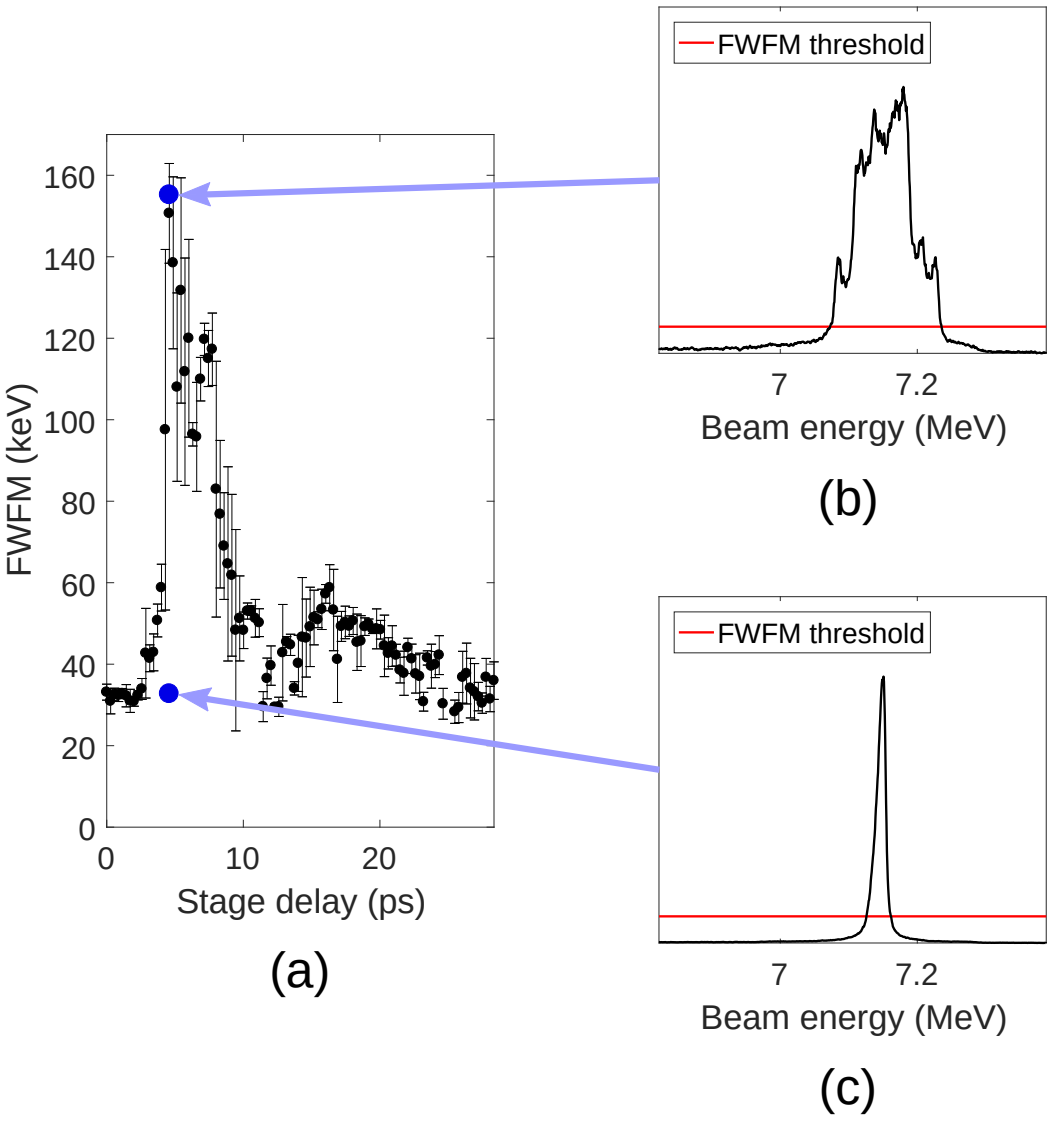

Figure 4.16: (a) Plot of beam energy spread as a function of THz arrival time. The energy spread is quantified by the FWFM identified in the energy distribution determined for thin slices of the overall beam image. Example energy distributions with (a) THz on and (b) THz off are taken from the images shown in Fig. 4.14. The relative locations of these measurements in the timing scan are marked with blue dots and corresponding arrows. These figures are reproduced from our publication, Ref. [98].

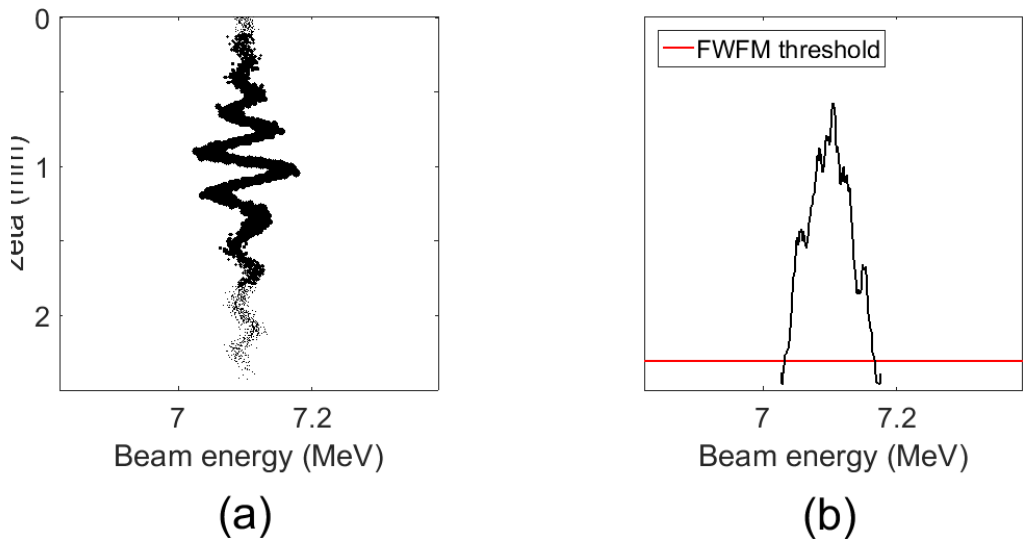

Figure 4.17: (a) 1-dimensional simulation of electron beam longitudinal phase space distribution after THz IFEL interaction under zero-slippage conditions and (b) the projected energy distribution. These figures are reproduced from our publication, Ref. [98].

To understand where these features come from it is useful to look at longitudinal phase space (LPS) simulations of the beam, like the example shown in Fig. 4.17. A multicycle energy modulation is produced in the long electron beam as the THz pulse is dispersed in the waveguide. The THz pulse envelope dictates the amplitude of the energy modulation along the beam. Assuming optimal timing overlap, electrons near the head and tail of the THz pulse experience only a small modulation, while near the peak of the THz envelope, electrons experience a larger change in energy.

Fig. 4.17b shows the projected energy distribution of the whole beam, since for the 1-dimensional simulation, vertical "slices" are meaningless. As with the experimental data, the energy distribution shows bumps, or steps, in energy, now identifiable as corresponding to the peaks in energy modulation at different parts of the beam. By taking the FWFM of the distribution, we are quantifying the range of the peak energy modulation in the multicycle LPS distribution.

The peak measured energy modulation proved to be 150 keV, as shown in Fig. 4.16a, corresponding to a maximum acceleration and deceleration of 75 keV. At the time, this

acceleration was an order of magnitude larger than had been previously demonstrated (7 keV) in a novel THz-linac structure [23] and is still twice as large as the recent results (>30 keV) using the segmented terahertz electron accelerator and manipulator (STEAM) device [27]. This record is even more dramatic given that the IFEL acceleration was accomplished using only a 1 μJ THz source, an order of magnitude smaller than in these experiments.

The key advantage leading to this high-efficiency performance of the THz IFEL is the "zero-slippage" scheme, enabling sustained the interaction for 30 cm. While the THz acceleration schemes in Refs. [27] and [23] achieved substantially larger acceleration gradients than the 0.25 MV/m of the IFEL, the energy exchange occurred over only a short distance (>30 MV/m over 1 mm and 2.5 MV/m peak over 3mm, respectively).

4.3.1 Tunable IFEL resonance condition

With evidence of the IFEL interaction established via measurements of the induced energy spread, the next stage in the proof-of-principle experiment was to verify characteristics of the interaction unique to the "zero-slippage" scheme. One of the particular advantages of the "zero-slippage" technique is the flexibility that the waveguide dispersion adds to the IFEL resonance condition. By tuning the waveguide aperture, we expect to change the phase velocity of the THz pulse as it propagates in the CPPWG, leading to a shift in the optimal beam energy for resonant interaction.

To confirm this tunable resonance condition, we sought to measure the magnitude of the IFEL induced energy modulation as a function of beam energy for different spacings of the CPPWG. To change the beam energy, we adjusted the amplitude of the field in the RF cavities. In principle, the change in energy could also have been accomplished by tuning the linac phase. However, throughout the IFEL experiment, we chose to operate the linac at the phase that minimized the beam energy spread in order to reduce the background energy spread present for the IFEL induced energy spread measurements, and generally maintain consistent operating conditions for the IFEL interaction.

At each beam energy, with the beam once more steered through the undulator to the final

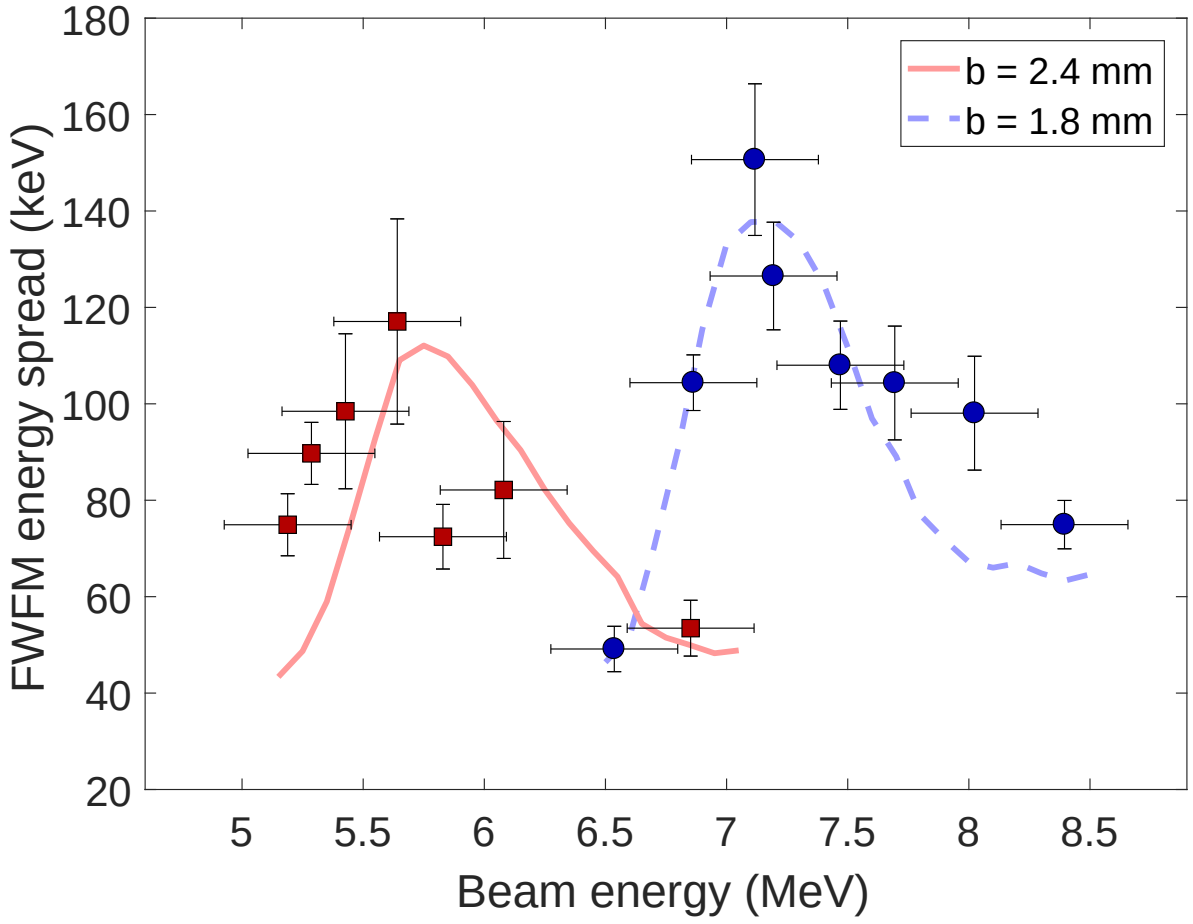

Figure 4.18: Measurements of the IFEL induced energy modulation as a function of beam energy show the shift in resonant interaction corresponding to the change in CPPWG plate spacing. This figure is reproduced from our publication, Ref. [98].

spectrometer screen, we performed a timing scan to identify the peak energy modulation. In Fig. 4.18, we show the results of the peak energy modulation as a function of beam energy for two plate spacings of the CPPWG. We expect to see the resonant energy of the interaction shift down as the plate spacing is increased. This may seem counterintuitive, because the group velocity increases at larger plate spacings. However, the key feature for resonant energy exchange is the phase velocity matching, and since the phase velocity decreases for wider plate spacings, we need a slower beam.

The simulation curves shown in Fig. 4.18 are generated by the WAFFEL simulation code with the frozen field approximation turned on, because the beam charge was too low (<1 pC) to significantly deplete or add energy to the THz pulse. To calculate the THz field, we assume 25% power coupling of the 1 μJ THz pulse, yielding an estimate of 4-8 MV/m for the maximum THz field propagating in the TE_{01} mode of the CPPWG. The coupling efficiency of the THz pulse into the waveguide is calculated using the transverse profile overlap integral of the free-space and waveguide modes.

We attribute the differences between predicted energy curves and actual energy spread measurements to experimental uncertainties like the coupling of the THz pulse into the guide and the alignment of the electron beam within the guide. In addition, images of the waveguide entrance, like those shown in Figs. 4.8 and 4.11, indicate some misalignment between the CPPWG plates after installation. This change to the CPPWG geometry, as well as potential misalignment in the longitudinal direction, equivalent to a taper of the waveguide, may have altered the interaction dynamics in ways outside the scope of the 1-D WAFFEL code.

With the only dynamically adjustable parameters being the CPPWG spacing and the beam energy, we know that we can only have one combination in which simultaneous phase and group velocity matching is achieved. This means that even as we demonstrate a shift in the resonant beam energy, we can expect to see the magnitude of the induced energy spread decrease as the group velocity mismatch increases. In addition to showing the expected shift in resonant beam energy, the measurements in Fig. 4.18 suggest that the 1.8 mm plate spacing was closer to the "zero-slippage" set point. From our earlier measurements indicating

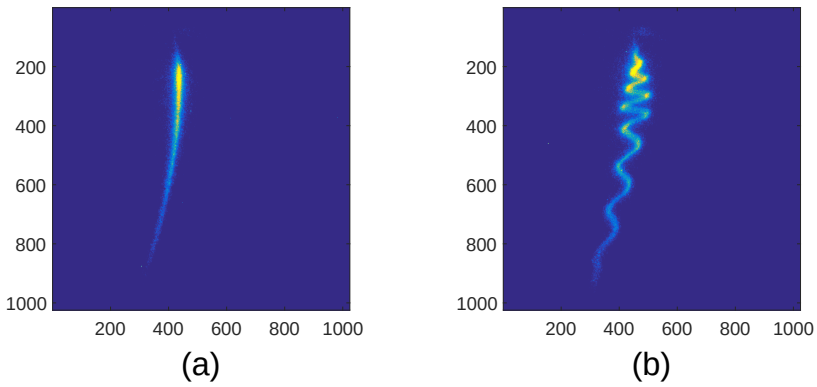

Figure 4.19: Raw LPS images with (a) THz off and (b) THz on.

a peak THz frequency at 0.84 THz, we expected "zero-slippage" interaction to occur near 2 mm plate spacing and 6.3 MeV beam energy.

Through measurements of the tunable resonance condition, we definitively show that the IFEL mechanism is occurring in a regime of dispersion dependent interaction. The waveguide serves not only to maintain the radiation intensity in the vicinity of the electron beam, but to match the phase velocity of the radiation for resonant interaction, and ideally, match the group velocity of the THz pulse to the average longitudinal propagation of the beam. For a more complete picture of this THz IFEL interaction we move on to longitudinal phase space measurements.

4.3.2 Longitudinal phase space measurements

Using the X-band deflector on the PEGASUS beamline, we impart a transverse momentum kick to the beam which streaks the longitudinal profile onto the vertical axis. In combination with the dipole spectrometer dispersing the beam energy onto the horizontal axis, the resulting distribution on the final YAG screen shows the longitudinal phase space of the beam. Before decreasing the bunch length to demonstrate bunch compression using the THz IFEL, we decided to look at the longitudinal phase space while the beam was still long enough to show the multicycle energy modulation. Examples of the raw LPS images are shown in Fig. 4.19, with (a) THz off and (b) THz on.

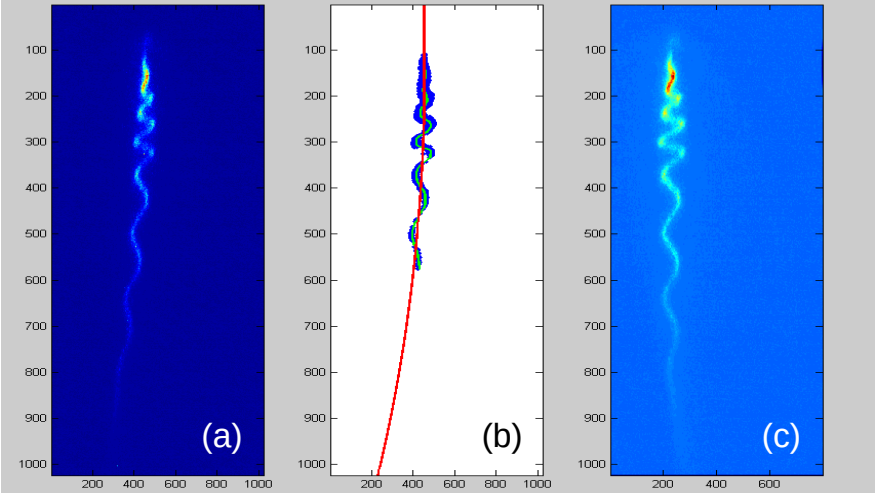

Figure 4.20: (a) Original raw beam image. (b) By filtering, cutting, and finally fitting the pixel data from (a), we establish a curve (red line) on which to transform the image to compensate for the overall shape determined by RF curvature during initial acceleration. The processed image, shown in (c), can then be used to characterize the beam quantitatively.

Once again, we'll begin by discussing some of the features that immediately stand out in these images. With THz off in Fig. 4.19a, there is a curvature to the beam distribution that is caused by the RF wave manipulation during the initial bunch generation and acceleration. This feature is obviously present in the case of THz on, Fig. 4.19b, as well, although it may be less noticeable compared to the higher frequency modulation caused by interaction with the higher frequency THz pulse.

This feature affects the accuracy of our energy spread measurements and the interpretation of the LPS distribution in general, so we'd like to remove it. This can be accomplished through an image transform defined by the conversion of the curve in Fig. 4.19a to a straight line. Alternatively, a moving average of the wiggling beam pattern can be used to identify the underlying RF curvature, as shown in the example images in Fig. 4.20. We used this latter method, because it enabled image transformation based on the analysis of each image individually and thereby reduced our run time, making frequent "THz off" background images unnecessary.

Fig. 4.21a shows the beam image from Fig. 4.19b after the residual RF curvature has been

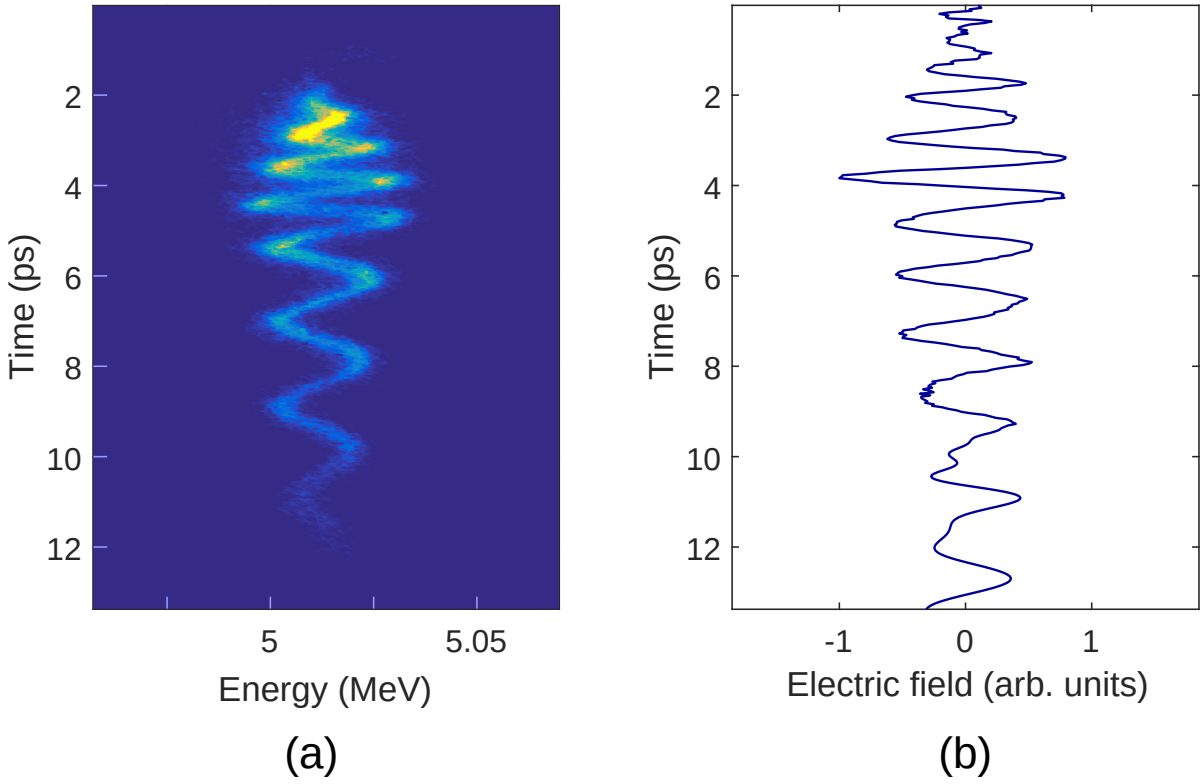

Figure 4.21: A corresponding frequency chirp is visible in (a) the processed LPS image from the raw image in Fig. 4.19 and (b) the model of the dispersed THz profile. These figures are reproduced from our publication, Ref. [98].

removed by the image transform. For an IFEL-induced energy modulation on an electron bunch which is long relative to the radiation wavelength, we expect to see a multicycle energy distribution. The non-standard feature here is the frequency chirp in the energy modulation, that is, the period of the energy modulation increases towards the tail of the beam at the bottom of the image. This frequency chirp is the result of dispersion of the THz pulse in the CPPWG. As the THz pulse propagates in the waveguide, the initially near single cycle pulse is elongated into a multicycle waveform as frequency components travel at different speeds, resulting in spatial separation.

A comparison of the modulated beam LPS to the simulated dispersed THz profile shown in Fig. 4.21b reveals the same frequency chirp and same overall envelope of the modulation range, or wave amplitude, respectively. The multicycle THz profile was calculated from

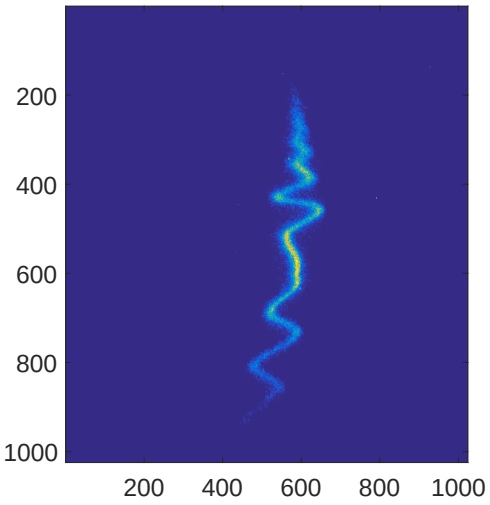

Figure 4.22: Example LPS image with irregular energy modulation

the initial measured waveform evolved over the length of the waveguide according to the CPPWG dispersion parameters.

In general, the shape of the energy modulation does not always reflect the shape of the dispersed THz profile, limiting the viability of using this technique as a "THz oscilloscope," particularly when the interaction occurs over a long enough distance that a velocity mismatch causes different regions of the THz pulse to interact with the same portion of the electron beam. An example of this effect for different CPPWG settings is shown in Fig. 4.22, in which the residual RF curvature and the overall frequency chirp of the energy modulation are visible, but the oscillations are irregular in period around what would be the peak of the energy modulation.

One of the features that we expect to see in Fig. 4.21, but that is not definitively present is a "sheering" effect in which the higher energy electrons on the right side out-pace the lower energy electrons on the left. This saw-toothed LPS distribution that would develop from velocity bunching indicates density modulations or "microbunching" characteristic of an IFEL. The fact that this asymmetry is not particularly visible in the LPS images of the beam indicates that the density modulation has not had enough time to develop during the drift section and foreshadows difficulty in the subsequent experimental demonstration of

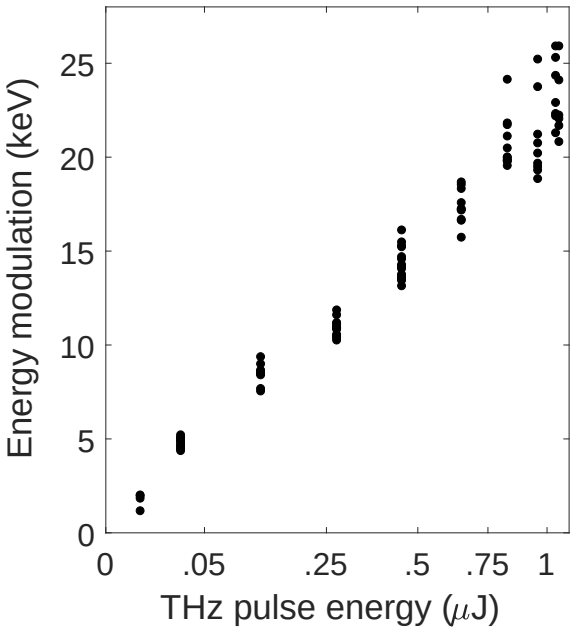

Figure 4.23: The magnitude of the IFEL induced energy modulation is plotted as a function of measured THz pulse energy. To show the linear relationship expected between modulation amplitude and THz field, the horizontal axis is plotted with a quadratic scale, such that the corresponding THz field increases linearly. This figure is reproduced from our publication, Ref. [98].

bunch compression via THz IFEL interaction.

With the full LPS information about the shape of the energy modulation, we were able to track the changes in the amplitude of the peak modulation as we adjusted the THz pulse energy. We expect the magnitude of the energy modulation to scale linearly with the THz electric field, but we were not able to measure that field directly. Instead, using measurements of the THz pulse energy taken outside of the in-vacuum interaction chamber, plotted on a quadratically scaled axis such that the corresponding electric field increases linearly, we see the expected relationship between THz field and energy modulation, shown in Fig. 4.23.

The LPS images of the long beam were also able to provide useful information about beam timing. The region of the electron beam that would interact with the THz pulse moved according to the time of arrival (TOA) of the beam, which could vary significantly,

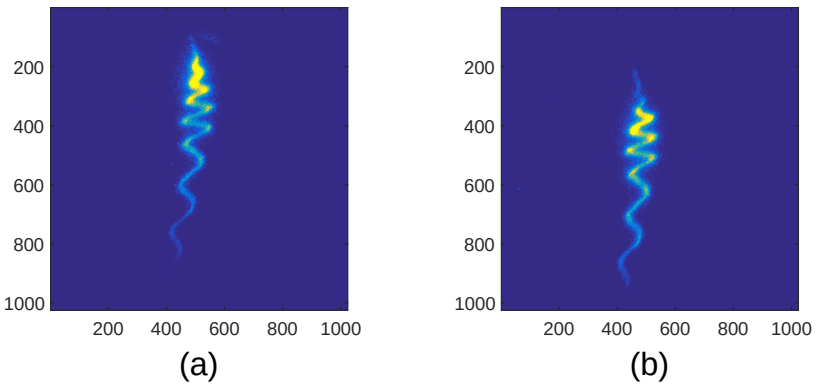

Figure 4.24: Raw LPS images with (a) the beam arriving early, so the energy modulation is closer to the tail of the beam, and (b) the beam arriving later, so the energy modulation is closer to the middle of the beam.

while the TOA of the THz pulse did not suffer from the RF induced timing jitter. If the beam showed up early, the tail of the beam would interact with the THz pulse; if the beam arrived late, the head of the beam would interact. This effect is shown in the example images of Fig. 4.24.

The shape of the energy modulation imprinted on the beam was consistent shot to shot, allowing us to identify and fit key features in each image, as shown in Fig. 4.25. With this energy modulation "stamp" on the beam, we could look at the vertical displacement, corresponding to time difference, between the beam centroid and the "stamp" to track the TOA jitter. Using this method we estimated the electron beam timing jitter for our experiment to be 400 fs rms.

4.3.3 THz-driven bunch compression

The bunch compression technique demonstrated in the last stage of our IFEL experiment imparts an energy chirp to the electron beam that is intended to ensure that the tail of the beam has higher energy than the head of the beam and therefore catches up over the course of a drift section. One of the primary characteristics that limits the compression factor achievable via this velocity bunching method is the linearity of the energy chirp. The

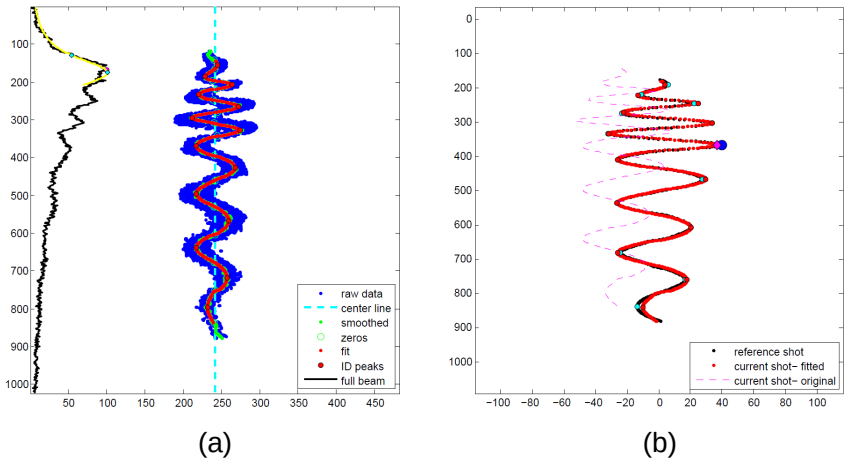

Figure 4.25: (a) Key features are identified in the LPS image of the beam and then (b) matched against a reference energy modulation.

shorter the beam is relative to the resonant wavelength of the interaction that modulates the beam energy, the more linear the energy chirp can be, particularly near the zero-crossing of the waveform. This is an advantage of RF-based compression schemes, as used in Ref. [65] and the THz FEL experiment, both performed at PEGASUS, in which the linac acted as a bunching cavity.

At higher frequencies, however, the beam can be chirped more efficiently, i.e. it requires less peak field amplitude to provide a similar field gradient for chirping the beam energy. Beyond the THz regime, it can be prohibitively difficult to get the full bunch length short enough to fit within the region of near-linear energy chirp. This leaves the THz regime as one of the best candidate for exploring efficient bunch compression techniques, as tested, for example, in Refs. [28, 109].

To demonstrate the application of bunch compression via THz IFEL interaction, we decreased the electron bunch length by changing the UV path such that the pulse bypassed the stretcher section before being used to generate the beam. In addition, we reduced the bunch charge by decreasing the UV pulse energy in order to minimize the bunch lengthening due to space charge repulsion. Ideally, the resulting beam would fit within a single ponderomotive bucket of the interaction.

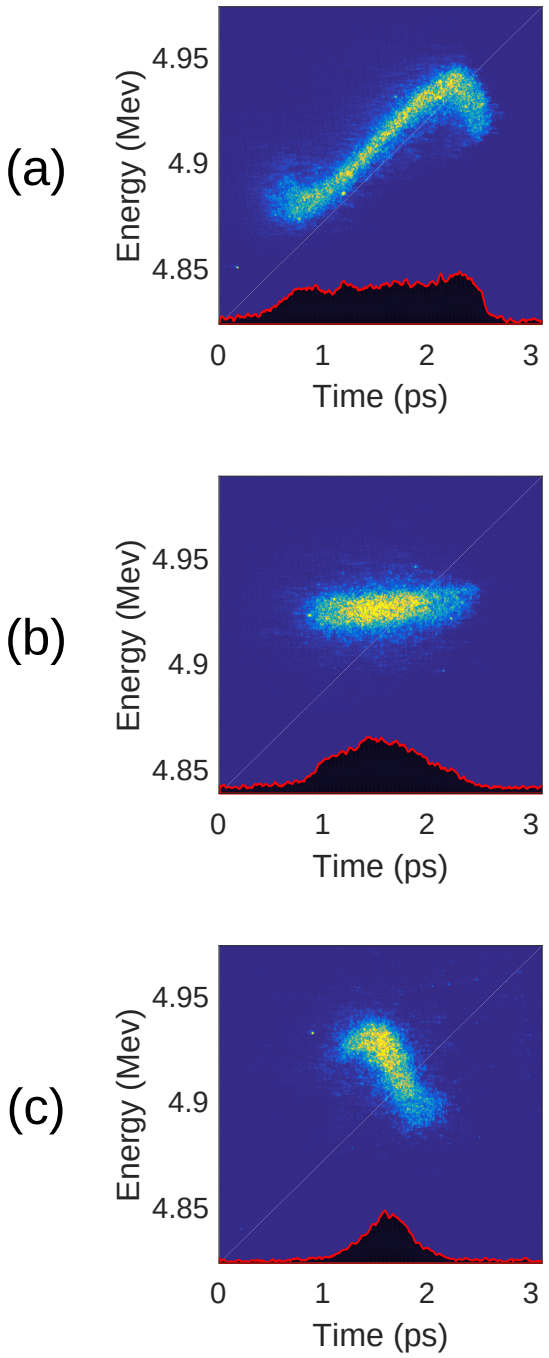

Figure 4.26: LPS images of a (a) decompressed beam, (b) beam with THz off, and (c) compressed beam, with the longitdudinal distribution projected onto the horizontal axis. These figures are reproduced from our publication, Ref. [98].

From our LPS measurements taken with the long electron beam, we know to expect significant timing jitter. This means we cannot control the injection phase of the electron beam, i.e. where the beam enters the bucket, or even which bucket it's in. Some shots will receive an energy chirp with the correct sign, resulting in bunch compression by the time the LPS measurement is performed downstream. Other shots will receive an energy chirp with the opposite sign, resulting in decompression of the beam. Fig. 4.26 shows example LPS images for the case of decompression and compression, as well as "THz off," with their respective longitudinal distributions projected onto the horizontal axis.

No image transform was performed on these measurements to remove residual RF curvature, because the bunch length was short enough relative to the RF wave so as to have negligible LPS distortion. However, the bunch length was not short enough to fit within the half cycle of the THz waveform. This is evidenced by the turnover in the LPS energy chirp on either end of the beam in Figs. 4.26a and c.

The positive energy chirp of the decompressed beam in Fig. 4.26a is still readily observable in the energy-position correlation of the LPS distribution at the time of measurement. Unfortunately, the negative energy chirp imparted to the compressed beam in Fig. 4.26c is also observable in the energy-position correlation of that image as well, indicating that the beam had not achieved full compression by the time of the measurement. This is not entirely unexpected given what we saw with the long beam measurements in which the beam did not achieve a significant density modulation by the time it reached the X-band deflector.

To characterize the set of measurements taken in the short beam configuration, we have plotted the measured energy spread and bunch length for each shot in Fig. 4.27. The points are color coded according to the energy-position correlation determined by the LPS distribution. This allows us to see the transition from increased energy spread due to chirp with the wrong sign, resulting in longer bunchlength, down to increased energy spread due to chirp with the correct sign, resulting in shorter bunchlength.

Gray lines are used in Fig. 4.27 to indicate the energy spread and bunch length when the THz pulse is off. With these markers, we see that in the vicinity of the baseline bunch

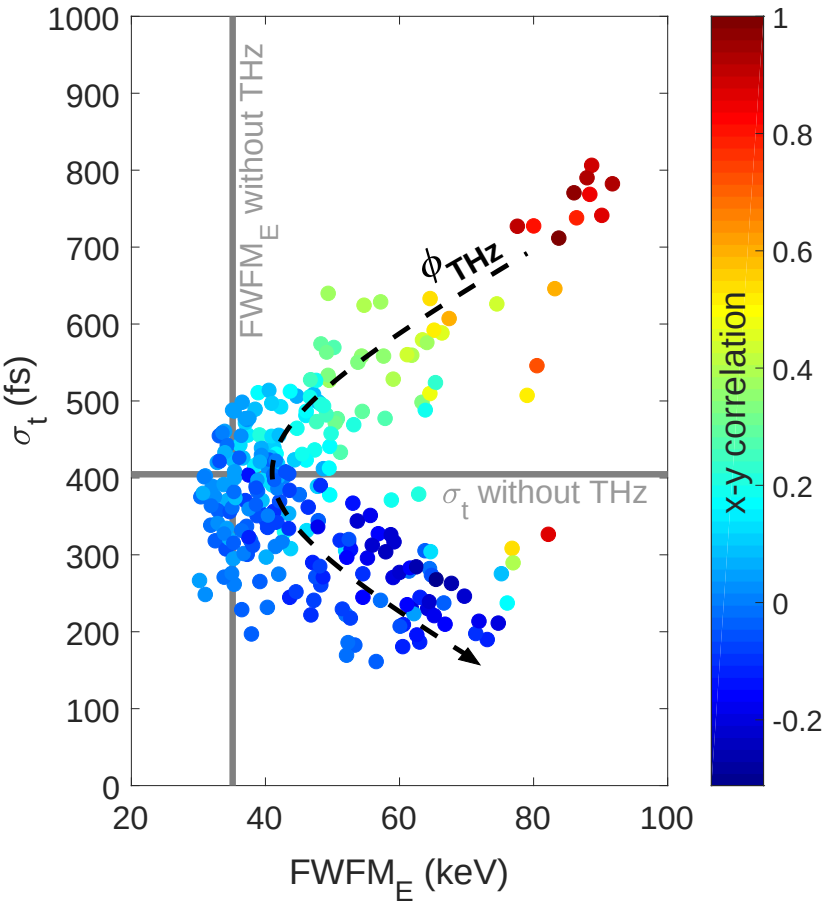

Figure 4.27: Plot of the bunch length vs. energy spread from LPS measurements of the short beam. Color indicates energy-position correlation in the LPS image. This figure is reproduced from our publication, Ref. [98].

length there are many examples of LPS measurements showing increased energy spread, but no significant energy-position correlation. These points most likely correspond to cases in which the beam interacted near the crest of the THz wave, resulting in a highly nonlinear energy chirp with both the head and tail of the beam ending up with nearly the same energy but differing from the middle of the beam.

These LPS measurements show that, using the THz IFEL as a compressor, we were able to reduce the bunch length by a factor of two, from a baseline of 400 fs rms to around 200 fs rms. The latent energy-position correlation in the LPS images of the compressed beams indicate further compression could have been measured after an additional drift distance. Because the distance between the interaction chamber and the deflecting cavity is fixed on the beamline, the amplitude of the energy chirp would ideally be increased to achieve faster compression, minimizing the bunch length in the deflector. However, the available THz field was already limited by the driving IR pulse energy and THz conversion efficiency.

The measurements presented here provide a wealth of information on the "zero-slippage" IFEL technique and its applications. However, the results up to this point have shed little light on the energy exchange that could be achieved with the THz pulse, particularly since the beam charge was kept small during the course of this experiment. To learn more about the effect of the "zero-slippage" interaction on the THz pulse, and its potential applications, we now turn to the THz FEL experiment and the related simulation results, which we'll discuss in the next chapter.

CHAPTER 5

THz FEL Experiment

The THz FEL experiment performed on the PEGASUS beamline used the same undulator and CPPWG apparatus that supported the IFEL interaction discussed in the previous chapter. The focus of the FEL experiment was on measurements of the THz pulse after "zero-slippage" interaction with the electron beam, providing a valuable compliment to the results of the THz IFEL experiment. Where before we saw THz-induced modulation of the beam energy, here we identified beam-induced changes to the THz energy.

The goals of the THz FEL experiment went beyond completing the picture of conserved energy exchange, however. With this new round of measurements, we sought to demonstrate the capabilities, and expose the potential limitations, of a THz source based on the "zero-slippage" FEL technique. While the proof-of-principle results presented here are as-yet negligible compared to the realm of THz production seen at dedicated THz FEL user facilities around the world, both measurement and simulation suggest the "zero-slippage" FEL technique may be a competitive THz source, able to produce pulse energies at the hundreds of μJ level, despite operating with only a 100 to 200 pC beam at a few MeV, as could be provided at an accelerator facility like PEGASUS.

We'll begin this chapter with a discussion of the THz diagnostics, i.e. what quantities we were interested in and what we were actually able to measure, then discuss the changes to the beam operation that were required to achieve a short bunch length. We'll then present measurements of the THz pulse energy after interaction and conclude with a discussion of simulation results that provide an exciting outlook on the application of the "zero-slippage" FEL technique as a THz source and amplifier.

5.0.1 THz diagnostics

One of the key features of the "zero-slippage" interaction is the broadband coupling enabled by the waveguide dispersion. Measurements of the spectral content of the THz pulse before and after interaction could show that near resonant energy exchange can take place over a range of frequencies, providing means of verifying the predicted bandwidth of interaction.

Throughout this thesis work, measurements of the THz spectrum were performed via Fourier analysis of an EOS trace which was generated over many different shots using an IR probe with a variable delay. However, this type of multi-shot time-sensitive measurement is not a viable diagnostic for a THz signal that is influenced by the timing jitter of the electron beam, measured during the IFEL experiment to be as large as 400 fs rms.

One solution to this problem would be to make the beam long enough (> 1 ps) that despite timing jitter, there is always a region of the beam interacting with the THz pulse. Assuming the beam parameters are uniform across the longitudinal profile, i.e. negligible energy chirp, etc., the beam will interact with the THz pulse in the same way shot-to-shot, producing a consistent output spectrum, that could be measured using an EOS technique.

Another solution to the timing jitter problem would be to make a single-shot measurement of the output THz spectrum, using for example a spatial autocorrelation interferometer [110] or grating-based spectrometer [111, 112] typically employed for bunch length measurements. The real-time interferometer (RTI) developed by Fermilab and Radiabeam Technologies [113] using a pyroelectric detector array provides a promising candidate for performing this measurement.

Unfortunately, the final energy of the THz pulse (< 0.2 μJ) meant that the intensity on each detector in the RTI array would be insufficient to distinguish signal from noise. The effective pulse energy is halved when the RTI splits the THz pulse, and then recombining the components on the 32-element array requires additional defocusing of the pulse. The THz source at UCLA starts out with only 1 μJ and given subsequent attenuation with each reflection on transport optics and diffraction losses in the CPPWG, the amount of radiation coupled into the waveguide and then transported to the detector could show reduction by

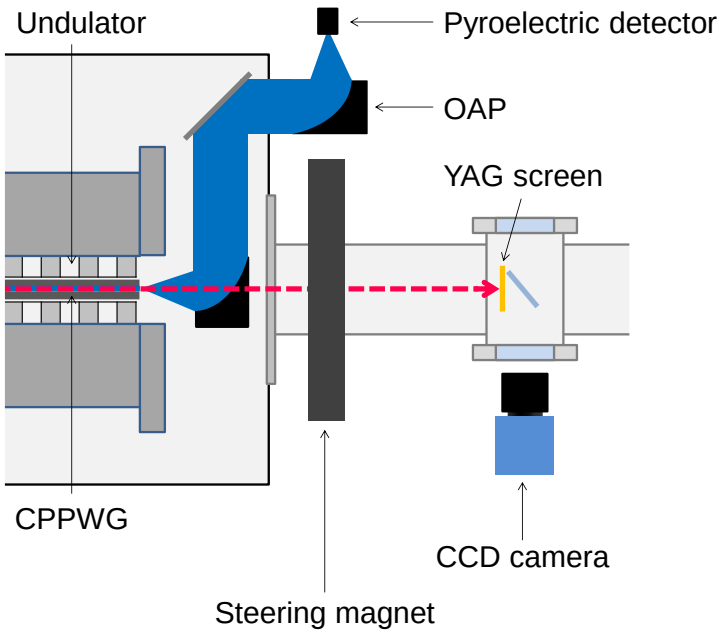

Figure 5.1: Diagram of the beamline set up for the THz FEL experiment

up to a factor of 10.

With the possibility of spectral measurements ruled out by the low THz pulse energy, we were limited to measurements of the output intensity for this round of THz FEL testing, using the single pyroelectric detector previously employed for alignment measurements. The THz pulse is collected at the exit of the CPPWG using an OAP mirror, with a small hole for beam transmission, and then redirected out of the vacuum chamber before a second OAP focuses it onto the pyroelectric detector, as shown in Fig. 5.1.

After completion of the THz-IFEL experiment, the pyroelectric detector was calibrated using adjustments to the THz power at the source and corresponding change in pyro signal, giving 7 mV/μJ. A comparison of the actual measurements and the expected scaling determined by simulation suggests an effective relationship closer to 1 mV/μJ. The significant difference between these results can be explained by misalignment and transport losses. In any event, for the sake of clarity when presenting our measurement we show both the detector measurements (mV) and simulated values (μJ) on separate axes, with a consistent scaling factor across all plots.

5.0.2 Electron bunch compression

Because our measurements of the THz pulse only characterize the overall pulse energy, we need to ensure that there is net energy exchange between the electron beam and THz pulse. This requires a very short beam ($< \lambda_{THz}/4$), such that the whole beam can interact at a phase that increases the beam energy or decreases the beam energy. Since the beam does not interact long enough to microbunch in our undulator, the beam must be "pre-bunched" before entering the undulator. In addition, to see an appreciable change in the energy, we need sufficient beam charge ($>$ few pC) to contribute to this overall exchange. Taken together these factors mean we need a high current beam, as expected given that the gain in an FEL is proportional to beam current.

We saw in the demonstration of THz-IFEL compression that by using the unstretched UV pulse and reducing the charge we could get the bunch length down to 400 fs rms. However, this was still too long for the whole beam to interact with the THz pulse at nearly the same phase, as shown by the roll-over in the modulated LPS distribution (see Fig. 4.26). Even more importantly, this required reducing the bunch charge to the point where net energy exchange with the THz pulse would be undetectable, thus an alternate method of reducing the electron bunch length while preserving as high charge as possible was required for the THz FEL experiment.

Recent work performed at PEGASUS by Maxson et al. [65], in which record-breaking ultrashort (<10 fs rms) bunch lengths were measured, provided an ideal blueprint for utilizing the linac as a bunching cavity to compress the beam for our experiment. Using GPT simulations, we determined the linac phase necessary for the beam to acquire an energy chirp with a gradient producing maximum compression at a distance in or near the undulator. In our case, this placed the beam off-crest by about 80°. A plot of the bunch length simulated in GPT as a function of distance along the beamline is shown in Fig. 5.2 along with snapshots of the evolving beam LPS.

The primary drawback to this technique was the larger energy spread which pushed some electrons outside of the range in which resonant interaction would occur. This effect initially

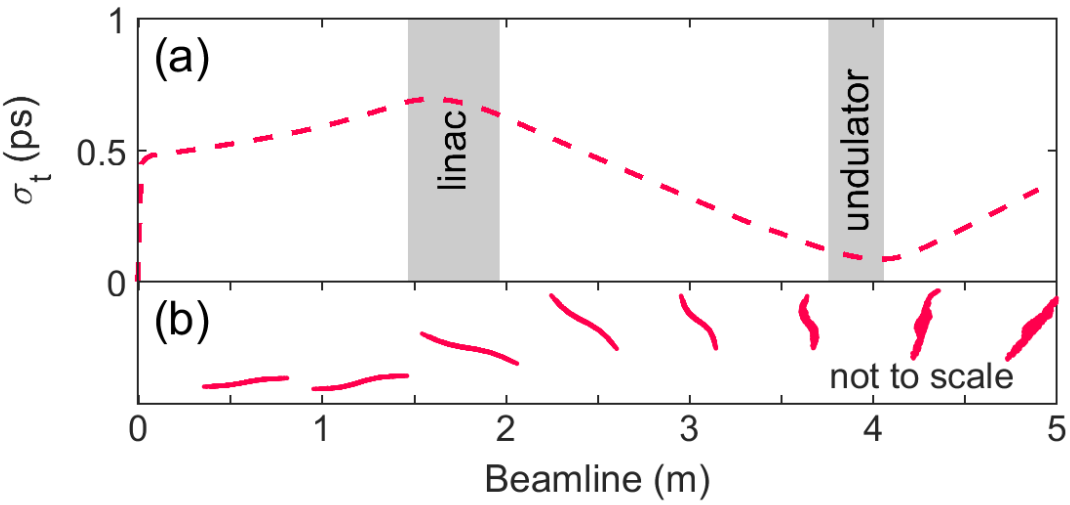

Figure 5.2: (a) GPT simulation of the electron bunch length as a function of distance along the beamline with the linac used as a bunching cavity. (b) Snapshots of the beam LPS as it undergoes compression.

cast doubts on whether the portion of the beam undergoing resonant interaction would be large enough to produce a non-negligible change in the THz pulse energy. However, WAFFEL simulations performed after-the-fact, using the beam energy spread determined by the spectrometer before the interaction chamber, indicate that the interaction can be sustained for all injected energies in the undulator, see Fig. 5.3. One factor in the success of the interaction despite the large energy spread may be the enhanced coupling enabled by the "zero-slippage" technique in which the tangential dispersion curves facilitate broadband near-resonant interaction in the waveguide.

The energy spread of the beam increased dramatically in the THz FEL experiment. Not only was there an increase due to the linac-induced energy chirp, but the spontaneous superradiant interaction of the beam in the undulator dramatically increased the energy spread of the beam, as suggested by the simulation in Fig. 5.3. Initially, we hoped to be able to correlate shot-to-shot THz energy measurements taken with the pyroelectric detector to beam images from the dipole spectrometer, allowing us to see the conserved energy exchange between THz pulse and electron beam. However, with the large energy spread, resulting in over-filling of the final spectrometer screen, energy measurements proved to be prohibitively

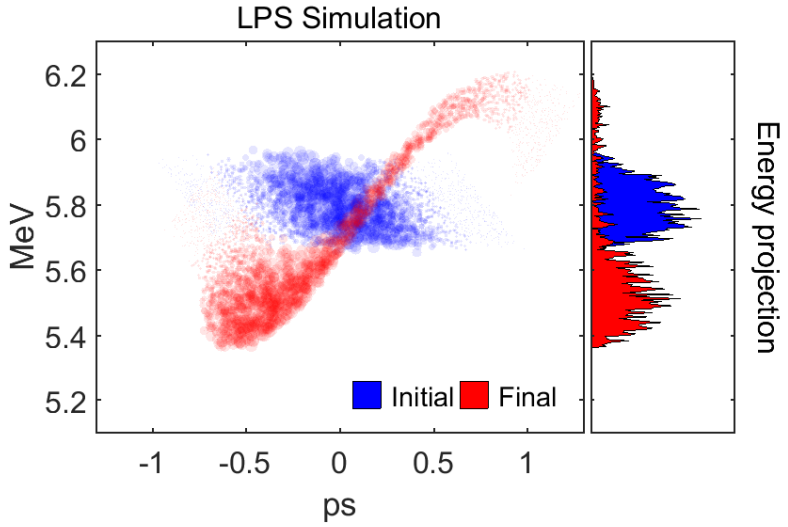

Figure 5.3: WAFFEL simulation of beam LPS in the THz FEL experiment. The initial beam distribution has not quite reached full compression, still showing the energy chirp imparted by the linac.

difficult. This effect was also detrimental to charge measurements taken with the Faraday cup placed at the end of the beamline, behind the spectrometer screen. Instead, measurements of the bunch charge were performed using the calibrated pixel sum on the YAG screen placed after the vacuum box, as indicated in Fig. 5.1.

5.1 THz FEL measurements

With the linac acting as a bunching cavity, the range in final beam energy was restricted to what could be achieved by the RF gun with only a marginal boost from the linac. To maintain resonance at this low beam energy (around 5.8 MeV), the CPPWG spacing was set to 2.6 mm. Using our experimental parameters in the WAFFEL simulation code, we can predict what the output THz pulse energy would be after interaction with the short beam without any beam timing jitter. By scanning the THz arrival time relative to the beam, we should see an oscillatory change in output energy, as in the simulated trace shown in Fig. 5.4. This matches our expectation given the oscillatory change in beam energy that we saw

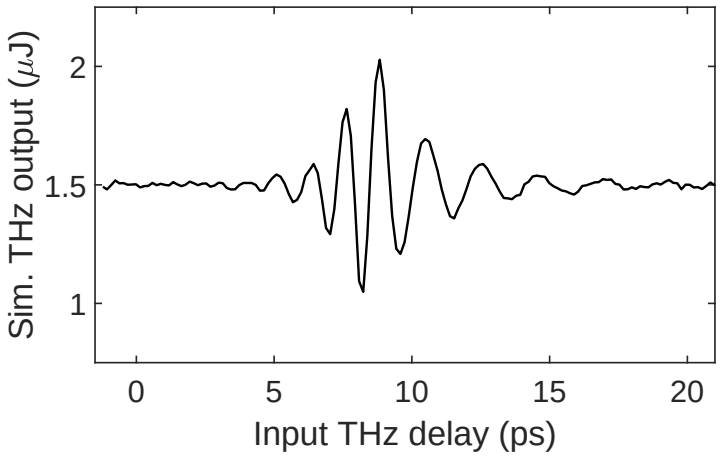

Figure 5.4: Simulated output THz energy as a function of input THz arrival time assuming no electron beam timing jitter. The simulation uses a THz seed with a peak field of 12 MV/m, but the primary contribution to the final THz energy is the spontaneous superradiance of the beam in the undulator.

in the long beam LPS measurements of the IFEL experiment. However, with timing jitter, the oscillatory pattern is smeared out, as we will see in the measurements of THz intensity vs. arrival time.

Finding the timing synchronization between the THz pulse and electron beam was less straightforward in this short bunch, large energy spread configuration. The eye-catching "bands" or "streaks" that were previously visible in the energy distribution of the long beam (see Fig. 4.14a) where not present in this case, because they were caused by the multicycle energy modulation in the beam that was long relative to the THz wavelength. In addition, the large energy spread of the beam meant that the dispersed beam distribution typically filled the final sprectrometer screen, making overall shifts in energy or energy spread indistinguishable. While changes to the general output energy of the THz pulse were detectable by eye, the primary change was an increase in fluctuations, which required confirmation via analysis of the recorded measurements (see Fig. 5.5) to be certain of the timing overlap.

The beam timing jitter prevented a consistent increase or decrease in average output energy as a function of THz arrival time. Consecutive shots sampled very different interaction

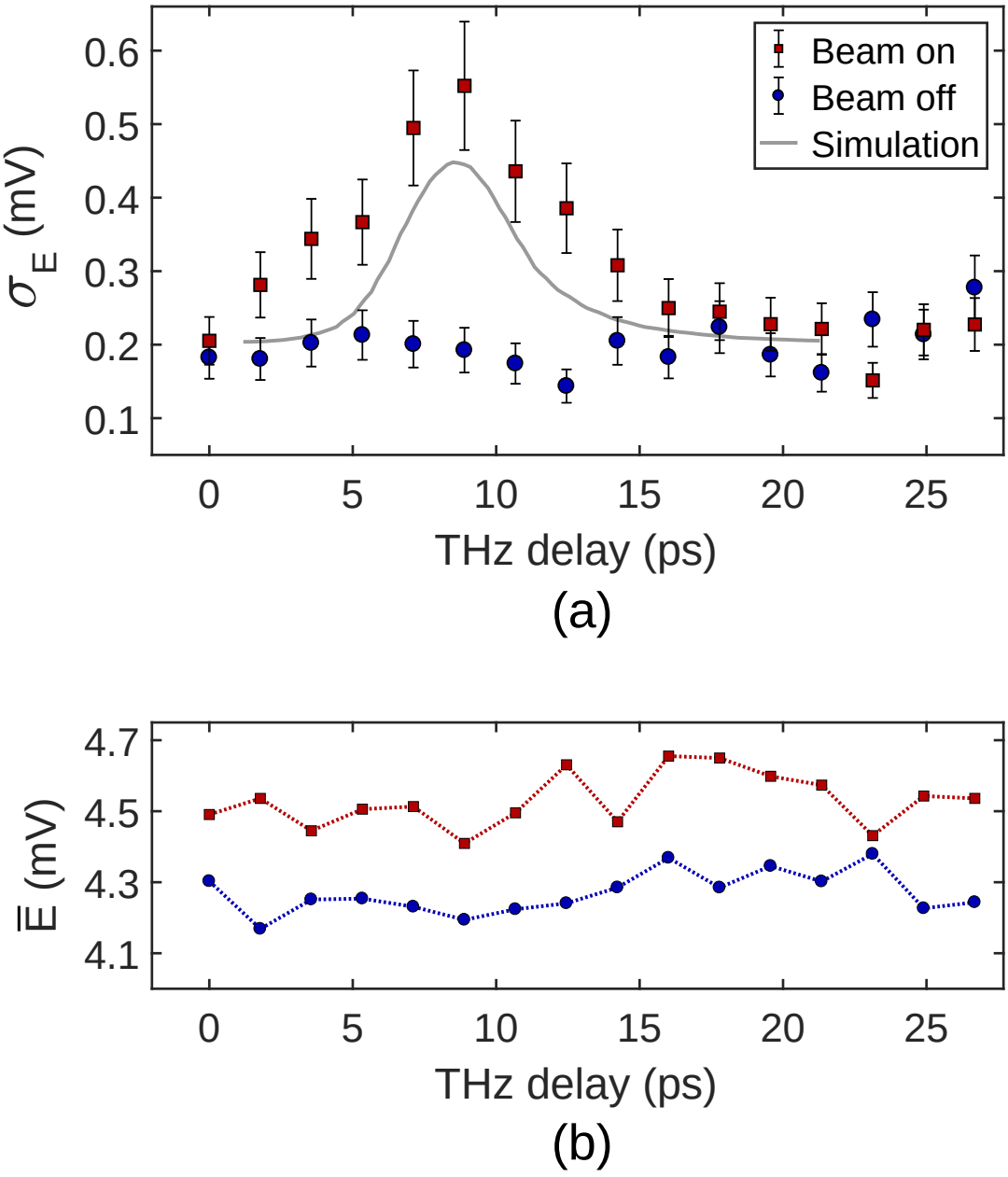

Figure 5.5: (a) Standard deviation of the output THz signal measured via pyroelectric detector as a function of input THz arrival time. (b) Average output THz signal as a function of input THz arrival time.

phases. This effect led to a clear time-dependent increase in the fluctuation of output THz energy, as well as an increase in the range of maximum and minimum output energy, and is captured by the standard deviation of the measured intensity, as shown in Fig. 5.5a, in which the standard deviation of the pyroelectric detector signal is plotted as a function of THz arrival time.

In Fig. 5.5b, we show the average pyroelectric detector signal as a function of THz arrival time. There is no visible time-dependent change reflecting the oscillatory output energy that we saw in the simulation case without timing jitter. However, there is a time-independent increase in output energy from the measurements taken without the beam present in the undulator. This indicates that the electron beam is producing THz radiation via spontaneous superradiance, when the seed THz pulse is not even present in the waveguide, because the bunch is short enough to radiate coherently as it oscillates in the undulator. This effect is an exciting new application of the "zero-slippage" FEL process which we will explore further in a subsequent measurement and WAFFEL simulations.

The gray curve in Fig. 5.5a corresponds to WAFFEL simulation results. This curve was produced by convolving the simulated output energy for the case of no timing jitter shown in Fig. 5.4, with a (1 ps rms) gaussian beam TOA distribution. This is not inconsistent with the initial timing jitter estimate given by the THz IFEL measurements (400 fs) due to the different operating conditions in the linac.

The TOA jitter of the beam entering the linac influences the beam energy coming out of the linac. This effect is smaller for a linac phase where the beam is near-crest (accelerating while minimizing energy spread) than when the beam is near the zero-crossing phase of the linac (imparting an energy chirp for bunch compression), since the steeper field gradient results in larger disparities in output energy, that subsequently cause larger timing jitter downstream.

One of the features of the THz FEL interaction that we can verify against predictions is how the energy exchange scales with bunch charge. From our timing measurement, we saw two processes at work in the interaction, stimulated amplification and spontaneous

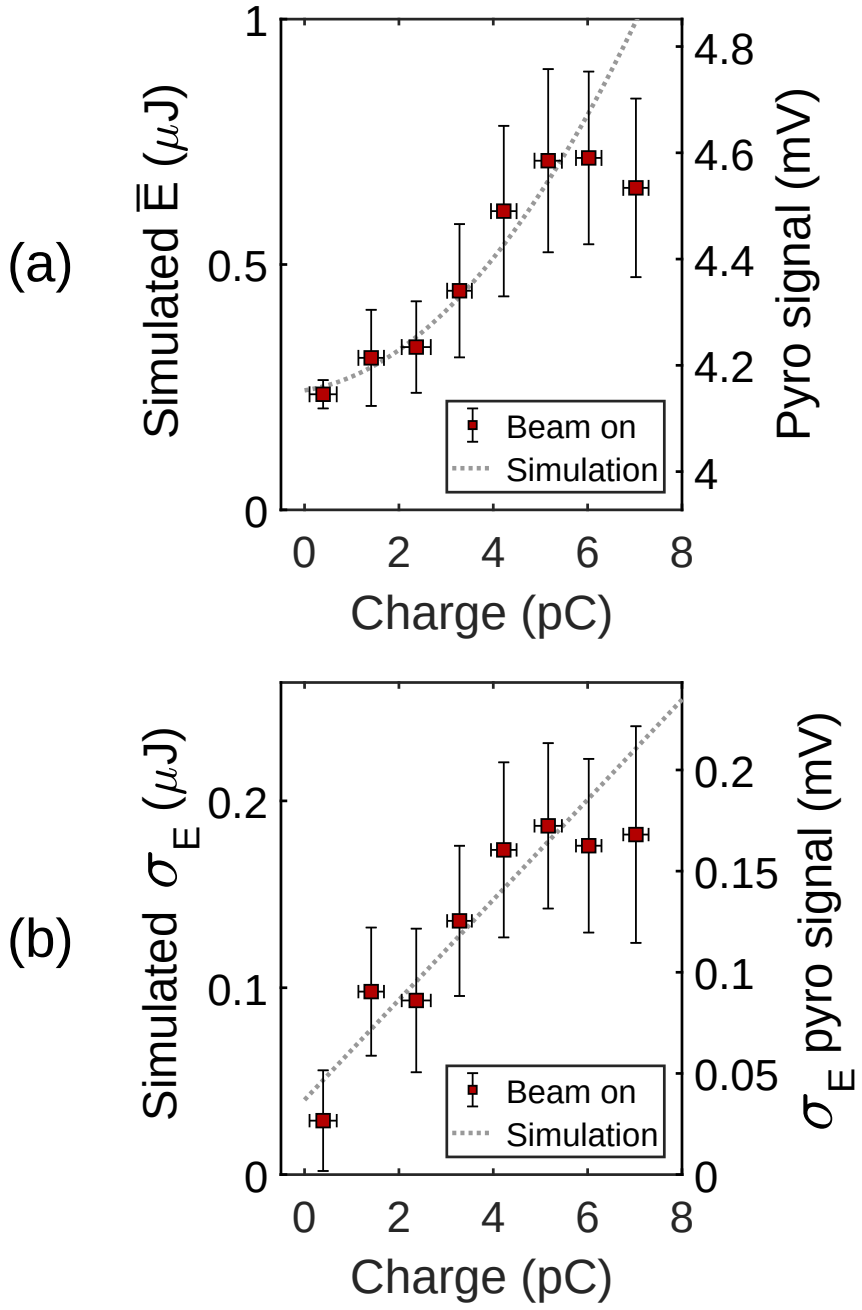

Figure 5.6: (a) Average output THz signal as a function of beam charge. (b) Standard deviation of the output THz signal measured as a function of beam charge.

superradiance, and these processes scale differently with the bunch charge. The average THz output energy conforms to the scaling for spontaneous superradiance, because the time dependent effect of stimulated amplification is averaged out due to beam timing jitter. We expect the superradiant contribution to scale quadratically with charge as shown by the simulation curve in Fig. 5.6.

As shown in the timing scan measurement, the time-dependent effect of stimulated amplification of the seed THz pulse can be quantified by the standard deviation of the output THz energy. With the THz arrival fixed at the time corresponding to peak output fluctuations, we expect the standard deviation to increase linearly with beam charge, as shown by the simulation curve in Fig. 5.6.

The measurements of output THz energy, performed with varying beam charge, are in good agreement with the predicted relationships shown by the simulation curves in Figs. 5.6a and b. The charge value plotted on the horizontal axis, was determined by binning the pixel sum on the after-box screen calibrated to correspond to beam charge.

At the highest charge, both the average output energy and the standard deviation of the output energy fall off relative to the predicted value. This effect may be the result of a variety of factors. Space charge effects most likely increase the beam size and emittances both longitudinally and transversely, causing poor spatial overlap for interaction in the regions of increased transverse beam size, and a wider range of interaction phases, i.e. less coherence in the emitted radiation, for the longer beam.

5.2 THz FEL simulations

The measurements performed in the THz FEL experiment show the great potential of this technique for application as a THz amplifier, or a stand alone source requiring no THz seed. The WAFFEL simulation code provides the tools for exploring the capabilities of the "zero-slippage" FEL in these two scenarios. The parameters of THz-IFEL and FEL experiments at PEGASUS offer a useful starting place for these simulation, but we'll now proceed with more freedom in the choice of undulator and beam parameters. In particular, the peak on-axis

field in the undulator can be increased along with the undulator period (now $\lambda_u = 3.6$ cm) in order to achieve a higher initial undulator parameter of $K = 2$, for a larger decelerating gradient ($\propto \frac{K}{\gamma}$). We'll also increase the total charge of the beam in order to increase the available energy that can be extracted for THz generation.

To improve the long-term extraction of energy from the beam, tapering of the undulator parameters can be used to prolong resonant interaction with the decreasing beam energy. Research has shown that careful optimization of the tapering scheme can lead to dramatic improvements in overall beam energy extraction (better than 30%) [114, 48], using the rate of change of the resonant energy and the ponderomotive gradient to determine the K taper in terms of resonant particle phase, Ψ_r. For the purposes of our simulations, exploring the capabilities of a hypothetical THz FEL, we'll restrict ourselves to simple linear tapering schemes with constant undulator period, avoiding the practical constraints and corresponding optimization that would be necessary in the design of the taper for an actual FEL experiment.

5.2.1 Broadband THz amplification

We'll first look at the application of broadband THz amplification using a long (4 ps rms) beam. The THz seed pulse to be amplified will begin the microbunching process necessary for coherent emission from the long beam. The initial energy modulation that develops into a density modulation can be imparted by a separate upstream undulator section, a.k.a. "prebuncher" [114], followed by a drift, or by the initial periods of the undulator, which then necessitates more periods overall to give the interaction time to reach saturation by the end of the undulator. We'll discuss here simulation results for the case in which the microbunching of the beam occurs within the first section of a single undulator.

In Fig. 5.7 we show the results of a simulation targeted to achieve 100 μJ THz output using a 200 pC beam. The input seed is a 2 μJ pulse with a Gaussian spectrum peaked at 0.4 THz. As microbunching is established and the energy gain approaches saturation, the undulator parameter is decreased, as shown in Fig. 5.7c. The interaction is allowed to evolve over 21 undulator periods.

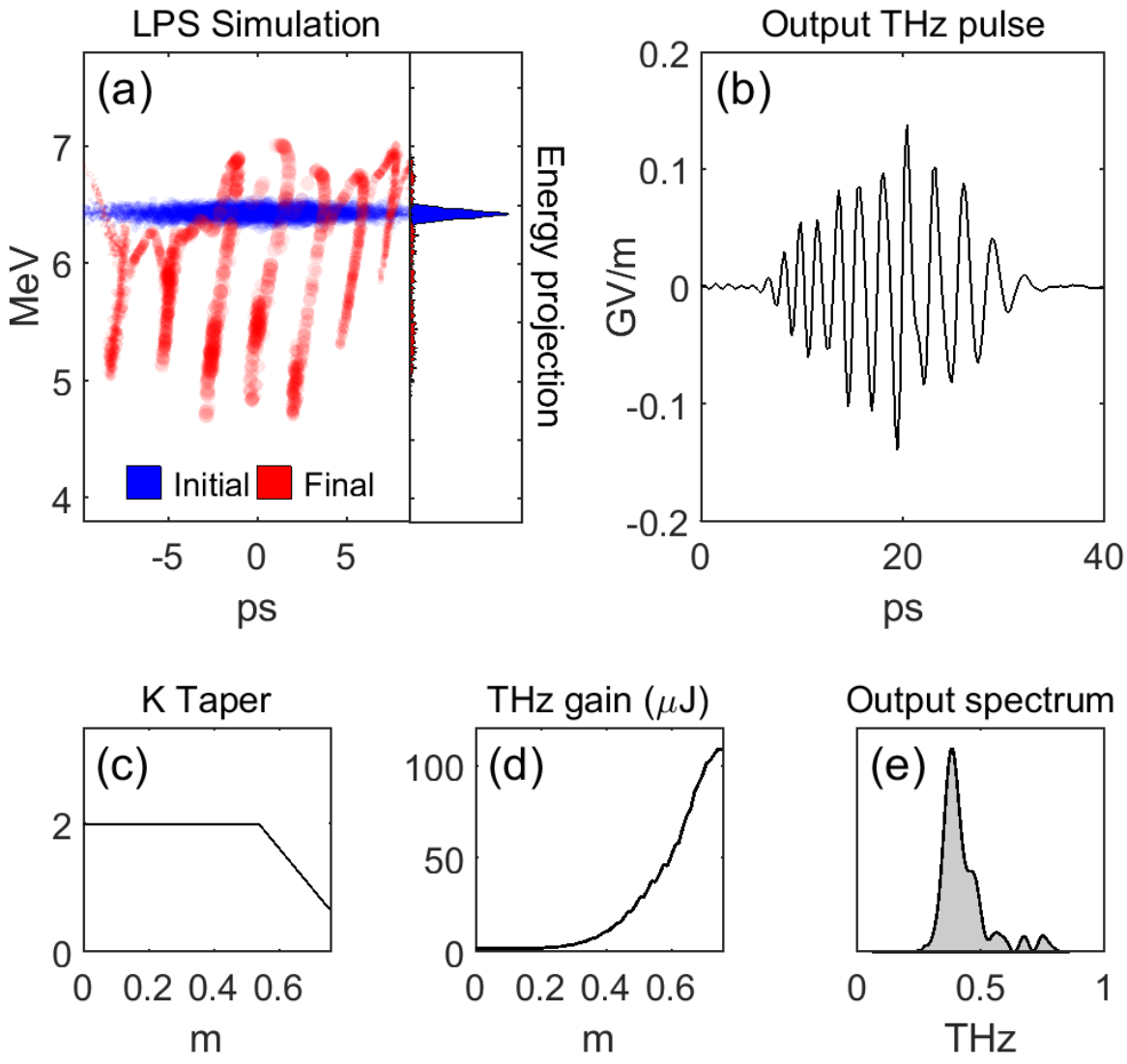

Figure 5.7: WAFFEL simulation of seeded THz FEL gain. (a) LPS beam distribution before and after interaction, with energy projection at right. (b) Simulated output THz pulse. (c) Tapering of undulator parameter, K. (d) Evolution of the THz pulse energy during interaction. (e) Final spectrum of the simulated THz output.

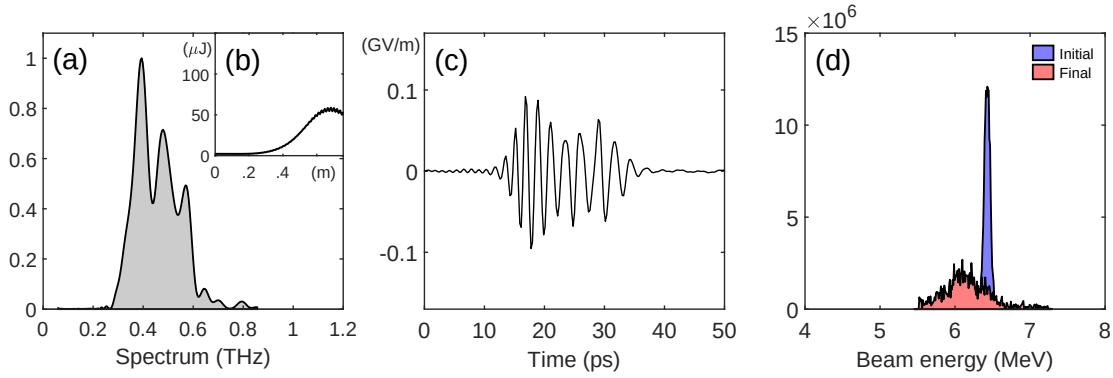

Figure 5.8: WAFFEL simulation of seeded THz FEL gain without tapering. (a) Final spectrum of the simulated THz output. (b) Evolution of the THz pulse energy during interaction. (c) Simulated output THz pulse. (c) Initial and final beam energy distribution.

Using the same initial parameters, but without tapering of the undulator, we see the THz output energy saturate just over 50 uJ. Figure 5.8 shows the simulation results using the same parameters but with the tapering turned off. The desired peak at 0.4 THz is joined by two significant secondary peaks at higher frequencies which are suppressed when the tapering is turned on.

The conversion of beam energy into coherent THz emission is most efficient when the process operates as an amplifier, i.e. the output spectrum is peaked near the input seed. However, for a high current beam, the output spectrum is quickly dominated by the resonance condition set by the undulator parameters, beam energy and plate spacing, potentially deviating from the peak frequency of the input THz spectrum.

5.2.2 Spontaneous superradiance

For the case of spontaneous superradiance in an unseeded THz FEL, the output frequency is fully set by the undulator parameters, beam energy and plate spacing. We'll look at a simulation using the same undulator and waveguide parameters as in the previous amplification results, but now with a 100 pC beam compressed to 120 fs. The sub-THz scale bunch length allows the beam to radiate coherently as soon as it undergoes oscillations in the undulator,

creating a superradiant THz source.

Without the waveguide the resonant frequency would be set by the standard FEL resonance condition

$$\lambda_r = \lambda_u \frac{1 + K^2/2}{2\gamma^2} \tag{5.1}$$

calculated from Eq. 2.10, using the average longitudinal beam velocity (Eq. 2.12) and $k_u/k_0 << 1$ for the case that $k_z = k_0$. For our parameters, this would give us resonance at around 0.86 THz, but with the waveguide at 3.5 mm plate spacing, the interaction is tuned for resonance at 0.4 THz. Given this very short, high-charge beam, not only is a THz seed unnecessary, but the interaction would proceed independently even with an input THz seed, since the spontaneous emission immediately dominates in the formation of the ponderomotive potential.

In Fig. 5.9, we show the results of the superradiant gain simulation which achieved 32% energy extraction to produce a 200 μJ pulse at the desired 0.4 THz. The initial beam LPS distribution has a slight energy chirp, not quite at maximum compression, assuming that a velocity bunching scheme, similar to that used in our experimental work, would be necessary to get the short, high current beam for spontaneous superradiance. The elongated LPS distribution of the final beam is the result of detrapping of particles from the ponderomotive potential well. In general, optimized energy extraction requires balancing the competing benefits of a large deceleration gradient to reach a lower final beam energy and a large ponderomotive bucket area to keep a greater fraction of the beam decelerating [48].

We can estimate the decrease in resonant energy as the undulator is tapered using the FEL resonance condition (Eq. 2.10) once again, with the same approximation for the average longitudinal beam velocity (Eq. 2.12) and $k_u/k_z << 1$, now for the case that $k_z \neq k_0$

$$\gamma_r = \sqrt{\frac{k_z(1 + K^2/2)}{2(k_z - k_0 + k_u)}}\,. \tag{5.2}$$

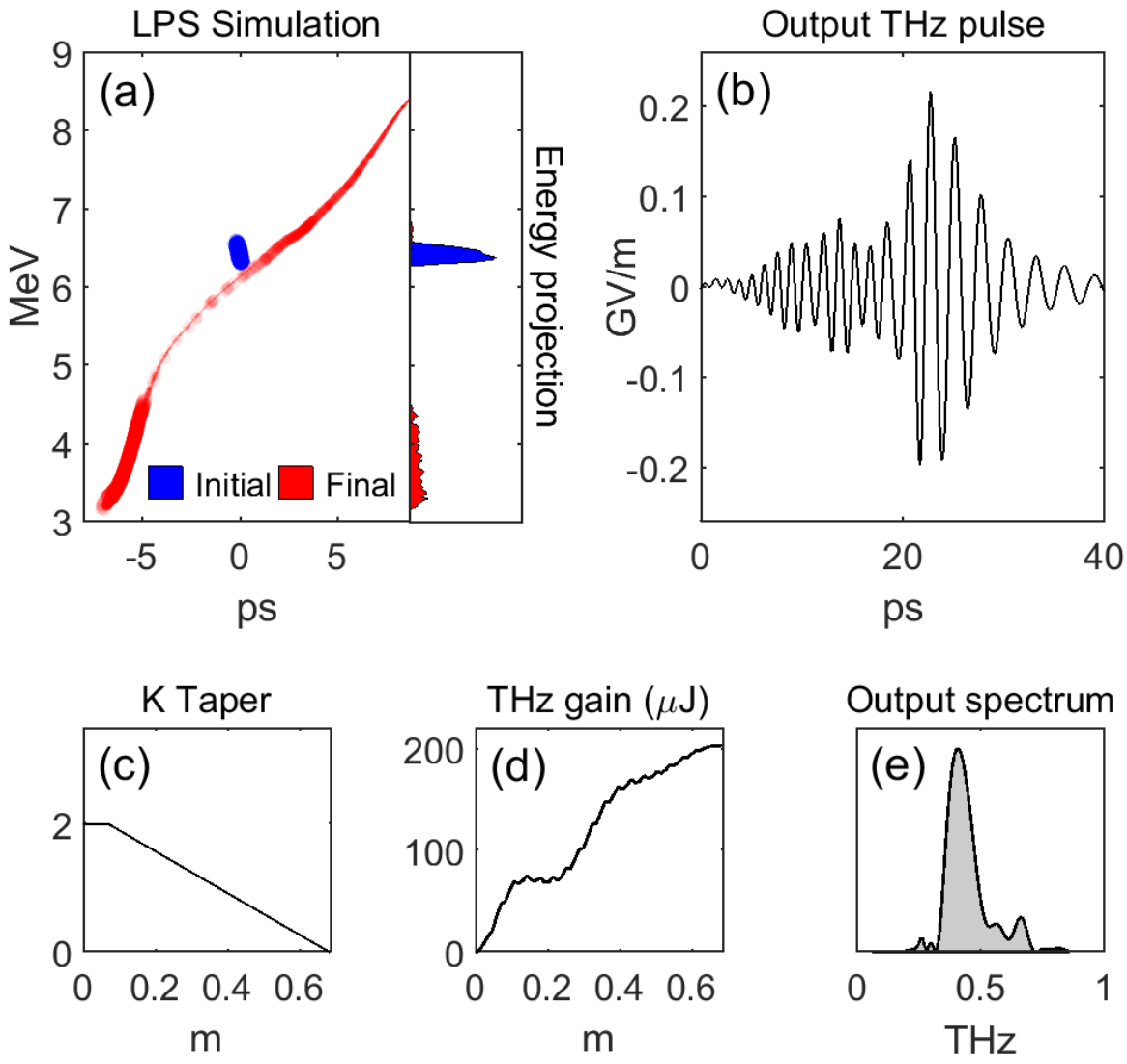

Figure 5.9: WAFFEL simulation of spontaneous superradiant THz FEL gain. (a) LPS beam distribution before and after interaction, with energy projection at right. (b) Simulated output THz pulse. (c) Tapering of undulator parameter, K. (d) Evolution of the THz pulse energy during interaction. (e) Final spectrum of the simulated THz output.

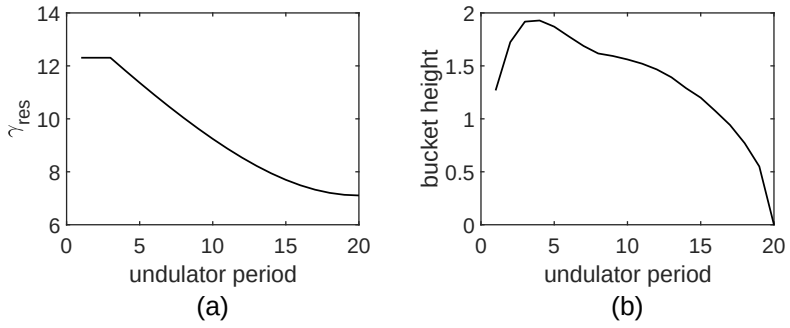

Figure 5.10: (a) Resonant beam energy and (b) bucket height ($\gamma_{max} - \gamma_{res}$) as a function of undulator period from the simulation of spontaneous superradiance in a tapered undulator.

In Fig. 5.10, we plot this shift in resonant energy and corresponding ponderomotive bucket height as a function of undulator period in the simulation. Obviously the taper of the undulator parameter cannot go to zero in practice, so the characterization of the resonant interaction towards the end of the undulator is not very meaningful. In the design of an actual undulator for a superradiant THz source, the tapering scheme will need to keep the undulator parameter within realistic bounds and the trade off between decelerating gradient and trapping fraction must be more thoroughly explored.

In Fig. 5.11, we show the evolution of the simulated THz spectrum, in which we expect to see a broad output spectrum produced by the wide-bandwidth coupling of the "zero-slippage" interaction. While the initial bandwidth is consistent with a prediction based on the inverse number of oscillations (typical of the low-gain regime), the value diverges from this relation after a few periods, exceeding the free-space-interaction bandwidth models for both low and exponential gain. A rough Gaussian fit of the simulated waveform over time shows the "zero-slippage" group velocity matching keeps the pulse length near the transform limited value with a fairly constant time-bandwidth product.

In Table 5.1, we show a comparison of the input parameters and results from the presented THz FEL simulations. Both techniques offer a promising method of producing broadband THz radiation with $> 100\,\mu$J energies in a nearly transform limited pulse. The "zero-slippage" operation facilitates broadband interaction, keeps the emitted radiation longitudi-

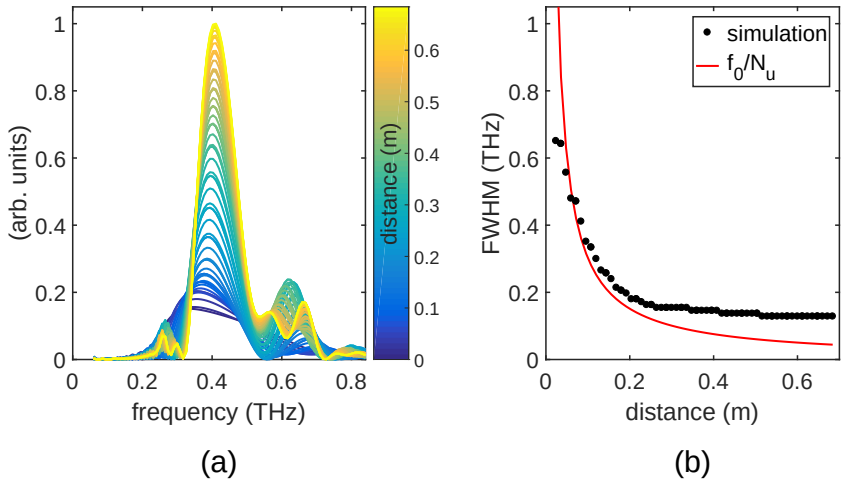

Figure 5.11: (a) Evolving THz spectrum produced in a simulation of spontaneous superradiance. Color indicates the distance the interaction has progressed along the waveguide. (b) FWHM of spectral content as a function of distance.

nally overlapped, minimizing pulse lengthening except due to dispersion, and ensures that the broad spectral content survives to the end of the interaction by limiting the attenuation due to diffraction and angular divergence of the disparate frequencies.

Eventually the "zero-slippage" condition breaks down due to factors like prolonged dispersive pulse broadening or changes in the average longitudinal beam velocity for a strongly decelerated beam. For $K > 1$, tapering of the undulator parameter should still keep the average longitudinal beam velocity matched to the THz pulse, with the decrease of the deflection angle (K/γ) tuned such that the longitudinal component of the beams velocity remains the same. However, this feature breaks down for $K < 1$, resulting in slippage that changes which frequency dominates the interaction, potentially producing a multi-peak output spectrum.

The next steps in exploring the tapered THz FEL design should include a quantitative study of the compromise between deceleration gradient and trapping fraction, using more realistic undulator parameters. With optimized tapering schemes, in which the period of the undulator is allowed to vary and K is not kept strictly linear, higher gain may be attainable. It will require more simulation work and ultimately, proof-of-principle experimental work, to determine the full potential of the "zero-slippage" FEL for a THz source application, but

Table 5.1: FEL Gain Simulations

	Amplifier	**Source**
Bunch length	4 ps	120 fs
Bunch charge	200 pC	100 pC
THz input energy	2 μJ	unseeded
Energy extraction	9 %	32 %
THz output energy	110 μJ	200 μJ
Peak THz field	0.14 GV/m	0.22 GV/m
Bandwidth (FWHM)	84 GHz	118 GHz

the outlook, based on our initial round of simulation studies, is highly promising.

CHAPTER 6

Conclusion

We have presented results in this thesis showing the successful demonstration of both THz IFEL and FEL interaction using a novel "zero-slippage" scheme. As predicted by our theoretical investigation of the "zero-slippage" regime, this coupling scheme has proven to be a highly efficient method of energy exchange with a THz pulse. In the THz IFEL experiment, we measured a record THz-induced energy modulation (150 keV) of a relativistic beam using only a 1 μJ source. This result is due in large part to the extended interaction length (30 cm) facilitated by the "zero-slippage" technique. While alternate schemes for THz-driven beam manipulation using a near-single cycle pulse [23, 27] have achieved significantly higher accelerating gradients (order of magnitude in both THz source energy and demonstrated gradient), the "zero-slippage" IFEL has allowed us to extract energy more efficiency using an interaction length that is two orders of magnitude longer.

Over the course of this work, we explored implementing the "zero-slippage" technique for a wide range of accelerator physics applications, including bunch compression, timing stabilization, THz streaking and broadband THz generation. A key characteristic of the "zero-slippage" interaction is the broadband coupling which allows it to extract energy from broadband pulses more efficiently, or, as an FEL, to produce broadband THz pulses. To model this novel interaction scheme, we developed our own 1-dimensional, multifrequency simulation code, outlined in this thesis, which allowed us to investigate the capabilities of this technique and extrapolate to new operating regimes.

The performance of a "zero-slippage" IFEL or FEL will easily be enhanced by increasing the THz field. This could be accomplished via both optimization of the waveguide coupling and by improving the power output of the THz source. There is an abundance of on-going

research dedicated to improving THz source technology [18], and even laser-driven techniques could soon provide single-cycle pulses with > 100 μJ energies [22]. At UCLA, the very recent Ti:Sapphire laser system upgrade at PEGASUS means a new era of THz projects may be on the horizon, utilizing the 40 mJ laser pulse now available for THz generation. Where before we obtained bunch length reduction by a factor of two in our proof-of-principle THz IFEL, the "zero-slippage" THz-driven compression scheme could now be fully realized at higher peak fields, producing <10 fs beams with applications in UED, microscopy, and advanced acceleration schemes.

The compatibility of the THz IFEL regime with comparatively low energy electron beams can point us to where the THz-driven "zero-slippage" IFEL may be most useful as an accelerator. For example, the THz IFEL could be a component in an all-optical staged acceleration scheme, bringing beams up to relativistic energies without any RF system and thereby eliminating the RF-induced timing jitter. The microbunching capability evidenced by the long beam longitudinal phase space measurements performed in the THz IFEL experiment at UCLA, could also potentially be applied to the formation of drive bunch trains with spacing at the THz lengthscale for plasma wakefield acceleration schemes.

The effect of spontaneous superradiance, already observed in the results of our THz FEL experiment, is a unique opportunity enabled by the length scale of the THz regime, in which total bunch capture becomes attainable. One of the features of the "zero-slippage" regime that may prove exciting in future FEL research is the potential for interaction between the short bunch and the spontaneous radiation it emits, as they remain spatially overlapped due to the group velocity delay in the guide. Initial results from the WAFFEL simulation tool suggest that at higher beam charges (100-200 pC), a tapered "zero-slippage" THz FEL could provide a >100 μJ level THz source. Given more thorough simulation studies and proof-of-principle experimental research, this technique has the potential to reach the mJ level.

APPENDIX A

EOS signal calculation

We derive here the change to the IR probe polarization that occurs during copropagation with the THz pulse in the EOS crystal, in our case ZnTe, and the corresponding change in measured signal at the two photodiodes used for so-called balanced detection. We will follow closely the derivation in Ref. [75]. The effect of each optical element in the electro-optic sampling setup is conveniently described in terms of Jones matrices, allowing us to put together a single expression for the start-to-finish effect on the probe using matrix multiplication. To begin with, we'll assume a horizontally polarized IR probe in the lab frame, represented by

$$\text{Probe} = E_{laser} \begin{bmatrix} 1 \\ 0 \end{bmatrix}. \tag{A.1}$$

In Eq. 3.35 of Chapter 3, we defined the phase shift, Γ, induced between the orthogonal components of the IR probe in the ZnTe crystal as a function of the angle, α, indicating the orientation of the linearly polarized THz field with respect to the X' crystal axis, as shown in Fig. A.1. In the coordinate system defined by the new slow and fast axis of the ZnTe crystal, this corresponds to

$$\text{ZnTe}(\alpha) = e^{-i\phi} \begin{bmatrix} e^{-i\Gamma(\alpha)/2} & 0 \\ 0 & e^{i\Gamma(\alpha)/2} \end{bmatrix} \tag{A.2}$$

where $\phi = \frac{\omega d(n_s+n_f)}{2c}$.

To get the IR probe description into and out of this coordinate system, we'll use the

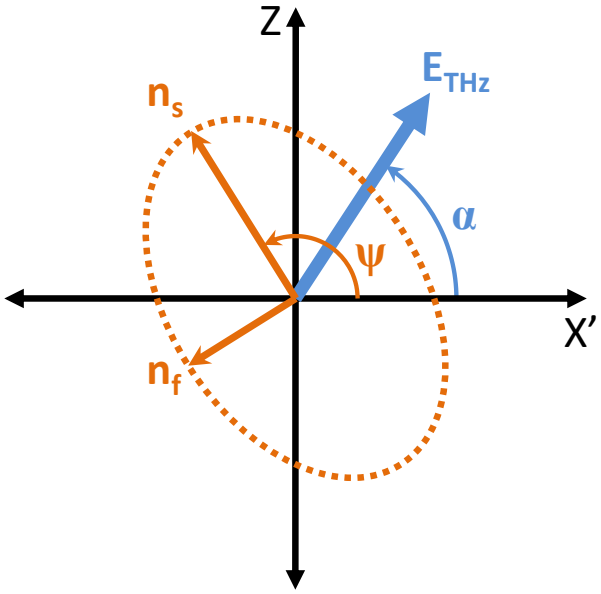

Figure A.1: With respect to the coordinate system determined by the crystal lattice, where Z is parallel to the [(0,0,0);(0,0,1)] line and X' is parallel to [(1,0,0);(0,1,0)] (as shown in Fig. 3.6 of Chapter 3), the index of refraction ellipse defined by the fast and slow axes (smaller index of refraction, n_f, and larger, n_s, respectively) rotates by angle Ψ in the presence of an electric field, E_{THz}, polarized at angle α.

standard rotation matrix

$$R(\theta) = \begin{bmatrix} \cos\theta & \sin\theta \\ -\sin\theta & \cos\theta \end{bmatrix}. \tag{A.3}$$

We'll need to use the same prescription for the coordinate system of the quarter waveplate, described by

$$\text{QWP} = \begin{bmatrix} e^{-i\pi/4} & 0 \\ 0 & e^{i\pi/4} \end{bmatrix}. \tag{A.4}$$

Finally, the Wollaston prism will separate the outgoing IR pulse into vertically and horizontally polarized components, each monitored by a photodiode. The effect of the EOS optics on the IR probe field measured, for example, at the "horizontal" photodiode is then described by

$$A_1 = E_{laser} \begin{bmatrix} 1 & 0 \end{bmatrix} \times R(-\pi/4) \times \text{QWP} \times R(\pi/4) \times R(-\psi) \times \text{ZnTe}(\alpha) \times R(\psi) \times \begin{bmatrix} 1 \\ 0 \end{bmatrix} \tag{A.5}$$

given that the quarter waveplate angle $(\pi/4)$ is set to turn an unmodulated horizontal IR polarization into circular polarization. The angle ψ indicates the rotation, relative to the lab frame, of the slow and fast axes of the altered indices of refraction in the ZnTe, as shown in Fig. A.1. This angle will be defined by the polarization of the THz pulse, according to the relation

$$\cos(2\psi) = \frac{\sin\,\alpha}{\sqrt{1+3\cos^2\alpha}}\,. \tag{A.6}$$

Working through the matrix multiplication step by step, up to the point just prior to taking the horizontal component, and gathering like terms, we have

$$\frac{e^{-i\phi}}{2} \begin{bmatrix} \left(\cos\psi^2 e^{-i\frac{\Gamma(\alpha)}{2}} + \sin\psi^2 e^{i\frac{\Gamma(\alpha)}{2}}\right)\left(e^{-i\frac{\pi}{4}} + e^{i\frac{\pi}{4}}\right) + \cos\psi\sin\psi\left(e^{-i\frac{\Gamma(\alpha)}{2}} - e^{i\frac{\Gamma(\alpha)}{2}}\right)\left(e^{-i\frac{\pi}{4}} - e^{i\frac{\pi}{4}}\right) \\ \left(\cos\psi^2 e^{-i\frac{\Gamma(\alpha)}{2}} + \sin\psi^2 e^{i\frac{\Gamma(\alpha)}{2}}\right)\left(e^{-i\frac{\pi}{4}} - e^{i\frac{\pi}{4}}\right) + \cos\psi\sin\psi\left(e^{-i\frac{\Gamma(\alpha)}{2}} - e^{i\frac{\Gamma(\alpha)}{2}}\right)\left(e^{-i\frac{\pi}{4}} + e^{i\frac{\pi}{4}}\right) \end{bmatrix} \tag{A.7}$$

With the simplification that

$$\left(e^{-i\pi/4} + e^{i\pi/4}\right) = \sqrt{2} \tag{A.8}$$

$$\left(e^{-i\pi/4} - e^{i\pi/4}\right) = -i\sqrt{2}\,, \tag{A.9}$$

the horizontal photodiode sees a field A_1 given by

$$A_1 = E_{laser}\frac{e^{-i\phi}}{\sqrt{2}}\left(\left(\cos\psi^2 e^{-i\frac{\Gamma(\alpha)}{2}} + \sin\psi^2 e^{i\frac{\Gamma(\alpha)}{2}}\right) - i\cos\psi\sin\psi\left(e^{-i\frac{\Gamma(\alpha)}{2}} - e^{i\frac{\Gamma(\alpha)}{2}}\right)\right) \tag{A.10}$$

and the vertical photodiode sees a field A_2 given by

$$A_2 = E_{laser}\frac{e^{-i\phi}}{\sqrt{2}}\left(-i\left(\cos\psi^2 e^{-i\frac{\Gamma(\alpha)}{2}} + \sin\psi^2 e^{i\frac{\Gamma(\alpha)}{2}}\right) + \cos\psi\sin\psi\left(e^{-i\frac{\Gamma(\alpha)}{2}} - e^{i\frac{\Gamma(\alpha)}{2}}\right)\right)\,. \tag{A.11}$$

Using these fields to calculate the measured intensity, we end up with

$$|A_1|^2 = \frac{E_{laser}^2}{2}\left(1 - 2\cos\psi\sin\psi\sin\Gamma(\alpha)\right) \tag{A.12}$$

$$|A_2|^2 = \frac{E_{laser}^2}{2}\left(1 + 2\cos\psi\sin\psi\sin\Gamma(\alpha)\right) \tag{A.13}$$

To see how the difference in these measured intensities is related to the phase shift, we take

$$|A_1|^2 - |A_2|^2 = -2E_{laser}^2\cos\psi\sin\psi\sin\Gamma(\alpha)\,, \tag{A.14}$$

giving us

$$\sin\Gamma(\alpha) = -\frac{|A_1|^2 - |A_2|^2}{2E_{laser}^2\cos\psi\sin\psi}\,. \tag{A.15}$$

Since we know from Eq. 3.35 that

$$\Gamma(\alpha) = \frac{\omega d}{2c}n_0^3 r_{41}E_{THz}\sqrt{1 + 3\cos\alpha^2}\,, \tag{A.16}$$

we can now express the THz field as

$$E_{THz} = \frac{2c}{\omega d n_0^3 r_{41}\sqrt{1 + 3\cos\alpha^2}}\arcsin\left(-\frac{|A_1|^2 - |A_2|^2}{2E_{laser}^2\cos\psi\sin\psi}\right)\,. \tag{A.17}$$

For $\alpha = 0$, as in our setup, Eq. A.6 tells us that $\psi = \pi/4$, so E_{THz} is given by

$$E_{THz} = \frac{c}{\omega d n_0^3 r_{41}}\arcsin\left(-\frac{|A_1|^2 - |A_2|^2}{E_{laser}^2}\right)\,. \tag{A.18}$$

To describe a rotation of the ZnTe crystal orientation, the angle α must be updated to indicate the new direction of THz polarization relative to the crystal axis.

REFERENCES

[1] L. Evans and P. Bryant. LHC machine. *Journal of instrumentation*, 3, no. 08 (2008): S08001.

[2] A. Grassellino, A. Romanenko, D. Sergatskov, O. Melnychuk, Y. Trenikhina, A. Crawford, A. Rowe, M. Wong, T. Khabiboulline, and F. Barkov. Nitrogen and argon doping of niobium for superconducting radio frequency cavities: a pathway to highly efficient accelerating structures. *Superconductor Science and Technology*, 26, no. 10 (2013): 102001.

[3] S. G. Tantawi. rf distribution system for a set of standing-wave accelerator structures. *Physical Review Special Topics-Accelerators and Beams* 9, no. 11 (2006): 112001.

[4] C. Joshi and V. Malka. Focus on laser-and beam-driven plasma accelerators. *New Journal of Physics* 12, no. 4 (2010): 045003.

[5] T. Tajima and J. M. Dawson. Laser electron accelerator. *Physical Review Letters*, 43, no. 4 (1979): 267.

[6] P. Chen, J. M. Dawson, Robert W. Huff, and T. Katsouleas. Acceleration of electrons by the interaction of a bunched electron beam with a plasma. *Physical review letters*, 54, no. 7 (1985): 693.

[7] G. Andonian and E. Simakov. Summary report of working group 3: Laser and high-gradient structure-based acceleration. *AIP Conference Proceedings*, vol. 1812, no. 1, p. 030003. AIP Publishing, 2017.

[8] J. W. Wang, and G. A. Loew. Rf breakdown studies in copper electron linac structures. *Proceedings of the 1989 IEEE Particle Accelerator Conference*, pp. 1137-1139. IEEE, 1989.

[9] D. Cesar, S. Custodio, J. Maxson, P. Musumeci, X. Shen, E. Threlkeld, R. J. England et al. High-field nonlinear optical response and phase control in a dielectric laser accelerator. *Communications Physics* 1, no. 1 (2018): 46.

[10] R. B. Palmer, Interaction of relativistic particles and free electromagnetic waves in the presence of a static helical magnet. *Journal of Applied Physics*, 43, no. 7 (1972): 3014-3023.

[11] J. M. Madey, Stimulated emission of bremsstrahlung in a periodic magnetic field. *Journal of Applied Physics*, 42, no. 5 (1971): 1906-1913.

[12] A. M. Kondratenko, and E. L. Saldin. Generating of coherent radiation by a relativistic electron beam in an ondulator. *Particle Accelerators*, 10 (1980): 207-216.

[13] P. Emma, R. Akre, J. Arthur, R. Bionta, C. Bostedt, J. Bozek, A. Brachmann et al. First lasing and operation of an ngstrom-wavelength free-electron laser. *Nature Photonics*, 4, no. 9 (2010): 641.

[14] K. Shimoda. Proposal for an electron accelerator using an optical maser. *Applied Optics*, 1, no. 1 (1962): 33-35.

[15] S. J. Smith and E. M. Purcell. Visible light from localized surface charges moving across a grating. *Physical Review* 92, no. 4 (1953): 1069.

[16] A. Gover and P. Sprangle. A unified theory of magnetic bremsstrahlung, electrostatic bremsstrahlung, Compton-Raman scattering, and Cerenkov-Smith-Purcell free-electron lasers. *IEEE Journal of Quantum Electronics* 17, no. 7 (1981): 1196-1215.

[17] G. P. Gallerano and S. Biedron, Overview of terahertz radiation sources. *Proceedings of the 2004 FEL Conference*, no. 1, pp. 216-221. 2004.

[18] S. S. Dhillon, et al. The 2017 terahertz science and technology roadmap. *Journal of Physics D: Applied Physics* 50.4, (2017).

[19] P. U. Jepsen, D. G. Cooke, and M. Koch. Terahertz spectroscopy and imagingModern techniques and applications. *Laser & Photonics Reviews*, 5.1, (2011).

[20] K. L. Yeh, M. C. Hoffmann, J. Hebling, and K. A. Nelson. Generation of 10 J ultrashort terahertz pulses by optical rectification. *Applied Physics Letters*, 90, no. 17 (2007): 171121.

[21] J. Hebling, G. Almasi, I. Z. Kozma, and J. Kuhl. Velocity matching by pulse front tilting for large-area THz-pulse generation. *Optics Express*, 10, no. 21 (2002): 1161-1166.

[22] C. Vicario, B. Monoszlai, and C. P. Hauri. GV/m single-cycle terahertz fields from a laser-driven large-size partitioned organic crystal. *Physical Review Letters*, 112, no. 21 (2014): 213901.

[23] E. A. Nanni, W. R. Huang, K.-H. Hong, K. Ravi, A. Fallahi, G. Moriena, R. D. Miller, and F. X. Kärtner. Terahertz-driven linear electron acceleration. *Nature communications*, 6 (2015): 8486.

[24] W. R. Huang, A. Fallahi, X. Wu, H. Cankaya, A.-L. Calendron, K. Ravi, D. Zhang, E. A. Nanni, K.-H. Hong, and F. X. Kärtner. Terahertz-driven, all-optical electron gun. *Optica*, 3(11):1209–1212, 2016.

[25] L. Zhao, Z. Wang, C. Lu, R. Wang, C. Hu, P. Wang, J. Qi et al. Terahertz streaking of few-femtosecond relativistic electron beams. *Physical Review X*, 8, no. 2 (2018): 021061.

[26] R. K. Li, M. C. Hoffmann, E. A. Nanni, S. H. Glenzer, A. M. Lindenberg, B. K. Ofori-Okai, A. H. Reid et al. Terahertz-based attosecond metrology of relativistic electron beams. *arXiv preprint* arXiv:1805.01979 (2018).

[27] D. Zhang, A. Fallahi, M. Hemmer, X. Wu, M. Fakhari, Y. Hua, H. Cankaya et al. Segmented terahertz electron accelerator and manipulator (STEAM). *Nature photonics*, (2018): 1.

[28] C. Kealhofer, W. Schneider, D. Ehberger, A. Ryabov, F. Krausz, and P. Baum. All-optical control and metrology of electron pulses. Science, 352, no. 6284 (2016): 429-433.

[29] S. S. Yu, W. M. Sharp, W. M. Fawley, E. T. Scharlemann, A. M. Sessler, and E. J. Sternbach. Waveguide suppression of the free electron laser sideband instability. *Nuclear Instruments and Methods in Physics Research Section A: Accelerators, Spectrometers, Detectors and Associated Equipment*, 259, no. 1-2 (1987): 219-225.

[30] A. Doria, G. P. Gallerano, and A. Renieri. Kinematic and dynamic properties of a waveguide FEL. *Optics communications*, 80, no. 5-6 (1991): 417-424.

[31] A. Gover, F. V. Hartemann, G. P. Le Sage, N. C. Luhmann Jr, R. S. Zhang, and C. Pellegrini. Time and frequency domain analysis of superradiant coherent synchrotron radiation in a waveguide free-electron laser. *Physical review letters*, 72, no. 8 (1994): 1192.

[32] A. Van Steenbergen, J. Gallardo, J. Sandweiss, and J-M. Fang. Observation of energy gain at the BNL inverse free-electron-laser accelerator. *Physical review letters*, 77, no. 13 (1996): 2690.

[33] P. Musumeci, S. Ya Tochitsky, S. Boucher, C. E. Clayton, A. Doyuran, R. J. England, C. Joshi et al. High energy gain of trapped electrons in a tapered, diffraction-dominated inverse-free-electron laser. *Physical review letters*, 94, no. 15 (2005): 154801.

[34] J. Duris, P. Musumeci, M. Babzien, M. Fedurin, K. Kusche, R. K. Li, J. Moody et al. High-quality electron beams from a helical inverse free-electron laser accelerator. *Nature communications*, 5 (2014): 4928.

[35] G. Ramian. The new UCSB free-electron lasers. *Nuclear Instruments and Methods in Physics Research Section A*, 318.1-3, (1992).

[36] A. Doria, V. B. Asgekar, D. Esposito, G. P. Gallerano, E. Giovenale, G. Messina, and C. Ronsivalle. Long wavelength compact-FEL with controlled energyphase correlation. *Nuclear Instruments and Methods in Physics Research Section A*, 475.1-3, (2001).

[37] M. Tecimer, H. Jiang, S. Hallman, and L. Elias. Variable height slot-outcoupling for the compact UH THz-FEL. *Free Electron Lasers 2003*, pp. 146-151. 2004.

[38] Y. U. Jeong, G. M. Kazakevitch, H. J. Cha, S. H. Park, and B. C. Lee. Demonstration of a wide-band compact free electron laser to the THz imaging of bio samples. *Nuclear Instruments and Methods in Physics Research Section A*, 575.1-2, (2007).

[39] G. N. Kulipanov, E. G. Bagryanskaya, E. N. Chesnokov, Y. Y. Choporova, V. V. Gerasimov, Y. V. Getmanov, S. L. Kiselev, B. A. Knyazev, V. V. Kubarev, S. E. Peltek, and V. M. Popik. Novosibirsk free electron laserfacility description and recent experiments. *IEEE transactions on terahertz science and technology*, 5.5, (2015).

[40] P. Tan, J. Huang, K. Liu, Y. Xiong, and M. Fan. Terahertz radiation sources based on free electron lasers and their applications. *Science China Information Sciences*, 55.1, (2012).

[41] C. Sung, S. Y. Tochitsky, S. Reiche, J. B. Rosenzweig, C. Pellegrini, and C. Joshi. Seeded free-electron and inverse free-electron laser techniques for radiation amplification and electron microbunching in the terahertz range. *Physical Review Special Topics-Accelerators and Beams*, 9.12, (2006).

[42] Y. C. Huang. Desktop megawatt superradiant free-electron laser at terahertz frequencies. *Applied Physics Letters*, 96.23, (2010).

[43] Y. U. Jeong, et al. Conceptual Design of a Table-top Terahertz Free-electron Laser *Journal of Korean Physical Society*, 59 (2011).

[44] D. Alesini, A. Battisti, M. Ferrario, L. Foggetta, V. Lollo, L. Ficcadenti, V. Pettinacci et al. New technology based on clamping for high gradient radio frequency photogun. *Physical Review Special Topics-Accelerators and Beams*, 18, no. 9 (2015): 092001.

[45] I. Wernick, and T. C. Marshall. Experimental test of the inverse free-electron-laser accelerator principle. *Physical Review A*, 46.6, (1992).

[46] W. D. Kimura, M. Babzien, I. Ben-Zvi, L. P. Campbell, D. B. Cline, C. E. Dilley, J. C. Gallardo et al. Demonstration of high-trapping efficiency and narrow energy spread in a laser-driven accelerator. *Physical review letters*, 92.5, (2004).

[47] J. T. Moody, S. G. Anderson, G. Anderson, S. Betts, S. Fisher, A. Tremaine, and P. Musumeci. Ultrashort laser pulse driven inverse free electron laser accelerator experiment. *Physical Review Accelerators and Beams*, 19.2, (2016).

[48] J. Duris High Efficiency Electron-Laser Interactions in Tapered Helical Undulators. Doctoral dissertation, University of California, Los Angeles. (2015).

[49] J. Rosenzweig. Fundamentals of beam physics. *Oxford University Press*, (2003).

[50] H. Wiedemann. Particle accelerator physics. *Springer*, (2015).

[51] P. Craievich, S. Di Mitri, M. Milloch, G. Penco, and F. Rossi. Modeling and experimental study to identify arrival-time jitter sources in the presence of a magnetic chicane. *Physical Review Special Topics-Accelerators and Beams*, 16, no. 9 (2013): 090401.

[52] R. Pompili, M. P. Anania, M. Bellaveglia, A. Biagioni, G. Castorina, E. Chiadroni, A. Cianchi, M. Croia, D. Di Giovenale, M. Ferrario, and F. Filippi. Femtosecond timing-jitter between photo-cathode laser and ultra-short electron bunches by means of hybrid compression. *New Journal of Physics*, 18, no. 8 (2016): 083033.

[53] Z. Zhang, Y. Du, L. Yan, Q. Du, J. Hua, J. Shi, J. Yang, D. Wang, W. Huang, H. Chen, and C. Tang. High time resolution beam-based measurement of the rf-to-laser jitter in a photocathode rf gun. *Physical Review Special Topics-Accelerators and Beams*, 17, no. 3 (2014): 032803.

[54] R. K. Li and C. X. Tang. Temporal resolution of MeV ultrafast electron diffraction based on a photocathode RF gun. *Nuclear Instruments and Methods in Physics Research Section A: Accelerators, Spectrometers, Detectors and Associated Equipment*, 605, no. 3 (2009): 243-248.

[55] E. Curry, S. Fabbri, P. Musumeci, and A. Gover. THz-driven zero-slippage IFEL scheme for phase space manipulation. *New Journal of Physics*, 18.11, (2016).

[56] I. M. Yakover, Y. Pinhasi, and A. Gover. Study of waveguide resonators for FEL operating at submillimeter wavelengths. *Nuclear Instruments and Methods in Physics Research Section A: Accelerators, Spectrometers, Detectors and Associated Equipment*, 375, no. 1-3 (1996): 260-263.

[57] E. Curry, S. Fabbri, P. Musumeci, and A. Gover. Simulation of 3-D effects in THz-based phase space manipulation. *Nuclear Instruments and Methods in Physics Research Section A: Accelerators, Spectrometers, Detectors and Associated Equipment*, 865, (2017).

[58] S. I. Bajlekov, et al. "Simulation of free-electron lasers seeded with broadband radiation," *Physical Review Special Topics-Accelerators and Beams*, 14.6, (2011).

[59] L. T. Campbell, and B. W. J. McNeil. "Puffin: A three dimensional, unaveraged free electron laser simulation code," *Physics of Plasmas*, 19.9 (2012).

[60] N. Piovella. "High gain free electron laser amplifiers starting from coherent and incoherent spontaneous emission," *Physics of Plasmas*, 6.8, (1999).

[61] L. F. Shampine, and M. W. Reichelt. The matlab ode suite. *SIAM journal on scientific computing*, 18.1, (1997).

[62] T. Nakahara, and N. Kurauchi. Guided beam waves between parallel concave reflectors. *IEEE Transactions on Microwave Theory and Techniques*, 15, 2 (1967).

[63] A. A. Zholents, and M. S. Zolotorev. Attosecond x-ray pulses produced by ultra short transverse slicing via laser electron beam interaction. *New Journal of Physics*, 10.2, (2008).

[64] G. Andonian, E. Hemsing, D. Xiang, P. Musumeci, A. Murokh, S. Tochitsky, and J. B. Rosenzweig. Longitudinal profile diagnostic scheme with subfemtosecond resolution for high-brightness electron beams. *Physical Review Special Topics-Accelerators and Beams*, 14.7, (2011).

[65] J. Maxson, D. Cesar, G. Calmasini, A. Ody, P. Musumeci, and D. Alesini. Direct measurement of sub-10 fs relativistic electron beams with ultralow emittance. *Physical review letters*, 118.15, (2017).

[66] M. J. De Loos, and S. B. Van Der Geer. General Particle Tracer: A new 3D code for accelerator and beamline design. *In 5th European Particle Accelerator Conference*, (1996).

[67] M. Bass, P. A. Franken, J. F. Ward, and G. Weinreich. Optical rectification. Physical Review Letters, 9, no. 11 (1962).

[68] J. Hebling, K. L. Yeh, M. C. Hoffmann, B. Bartal, and K. A. Nelson. Generation of high-power terahertz pulses by tilted-pulse-front excitation and their application possibilities. *JOSA B*, 25.7, (2008).

[69] K. L. Yeh. The generation of high field terahertz radiation and its application in terahertz nonlinear spectroscopy. Doctoral dissertation, Massachusetts Institute of Technology. (2009).

[70] S. W. Huang, E. Granados, W. R. Ronny Huang, K. H. Hong, L. E. Zapata, and F. X. Kärtner. High conversion efficiency, high energy terahertz pulses by optical rectification in cryogenically cooled lithium niobate. *Optics letters*, 38.5, (2013).

[71] J. T. Moody. Inverse Free Electron Laser Interactions with Sub-Picosecond High Brightness Electron Beams. Doctoral dissertation, University of California, Los Angeles. (2014).

[72] L. Pálfalvi, J. Hebling, G. Almási, Á. Péter, K. Polgár, K. Lengyel, and R. Szipöcs. Nonlinear refraction and absorption of Mg doped stoichiometric and congruent $LiNbO_3$. *Journal of applied physics*, 95.3, (2004).

[73] GENTEC-EO USA, INC. 5825 Jean Road Center, Lake Oswego, OR 97035, USA https://www.gentec-eo.com/products/special-products/Discrete_Pyros

[74] A. Yariv. Quantum Electronics, 2nd. *Edn. John Wiley & Sons, Inc.*, (1967).

[75] M. Brunken et al. Electro-optic sampling at the TESLA test accelerator: experimental setup and first results. TESLA Report 2003-11, (2003).

[76] I. M. Yakover, Y. Pinhasi, and A. Gover. Resonator design and characterization for the Israeli tandem electrostatic FEL project. *Nuclear Instruments and Methods in Physics Research Section A: Accelerators, Spectrometers, Detectors and Associated Equipment*, 358:1-3, (1995).

[77] D. H. Auston, and M. C. Nuss. Electrooptical generation and detection of femtosecond electrical transients. *IEEE Journal of quantum electronics*, 24.2, (1988): 184-197.

[78] K. Kan, I. Nozawa, Y. Yoshida, T. Kondoh, M. Gohdo, and J. Yang. Frequency and Time Domain Measurement of Coherent Transition Radiation. Proceedings IPAC16, MOPMB026, (2016).

[79] K. Kan, M. Gohdo, T. Kondoh, I. Nozawa, J. Yang, and Y. Yoshida. Measurement of Femtosecond Electron Beam Based on Frequency and Time Domain Schemes. Proceedings IBIC'16, TUPG58, (2016).

[80] E. Curry, B. Jacobson, A. Murokh, and P. Musumeci. Sub-picosecond shot-to-shot electron beam and laser timing using a photoconductive THz antenna. *In 4th International Beam Instrumentation Conference*, IBIC 2015, pp. 243-245. JACOW, (2016).

[81] B. Hidding, J. B. Rosenzweig, Y. Xi, B. O'Shea, G. Andonian, D. Schiller, S. Barber, O. Williams, G. Pretzler, T. Knigstein, and F. Kleeschulte. Beyond injection: Trojan horse underdense photocathode plasma wakefield acceleration. AIP Conference Proceedings, 1507.1 (2012).

[82] N. T. Yardimci, S. H. Yang, C. W. Berry, and M. Jarrahi. High-power terahertz generation using large-area plasmonic photoconductive emitters. IEEE Transactions on Terahertz Science and Technology, 5.2, (2015).

[83] N. T. Yardimci and M. Jarrahi. High sensitivity terahertz detection through large-area plasmonic nano-antenna arrays. Scientific reports, 7, 42667 (2017).

[84] E. Curry, B. Jacobson, M. Jarrahi, P. Musumeci, and N. Yardimci. Synchronization of ps Electron Bunches and fs Laser Pulses Using a Plasmonics-Enhanced Large-Area Photoconductive Detector. *In 5th Int. Beam Instrumentation Conference*, IBIC 2016, pp. 775-778. JACOW, (2017).

[85] J. Frisch Beam Arrival Time Monitors Proceedings IBIC'15, TUALA01, (2015).

[86] A. Angelovski, M. Kuntzsch, M. K. Czwalinna, A. Penirschke, M. Hansli, C. Sydlo, V. Arsov, S. Hunziker, H. Schlarb, M. Gensch, and V. Schlott. Evaluation of the cone-shaped pickup performance for low charge sub-10 fs arrival-time measurements at free electron laser facilities. Physical Review Special Topics-Accelerators and Beams, 18.1 (2015).

[87] A. Brachmann, C. Bostedt, J. Bozek, R. Coffee, F. J. Decker, Y. Ding, D. Dowell, P. Emma, J. Frisch, S. Gilevich, and G. Haller. Femtosecond operation of the LCLS for user experiments. Proceedings IPAC10, TUPE066, (2010).

[88] H. Matthias, B. Zeitler, A. Angelovski, S. Vilcins, R. Jakoby, H. Schlarb, K. Floettmann, D. Lipka, A. Penirschke, and F. Grner. A beam arrival time cavity for regae at desy. Proceedings IPAC'14, TUPRI104, (2014).

[89] X. Yan, A. M. MacLeod, W. A. Gillespie, G. M. H. Knippels, D. Oepts, A. F. G. van der Meer, and W. Seidel. Subpicosecond electro-optic measurement of relativistic electron pulses. Physical Review Letters, 85.16 (2000).

[90] J. Van Tilborg, C. B. Schroeder, C. V. Filip, C. Tth, C. G. R. Geddes, G. Fubiani, R. Huber, R. A. Kaindl, E. Esarey, and W. P. Leemans. Temporal characterization of femtosecond laser-plasma-accelerated electron bunches using terahertz radiation. Physical review letters, 96.1 (2006).

[91] C. M. Scoby, P. Musumeci, J. T. Moody, and M. S. Gutierrez. Electro-optic sampling at 90 degree interaction geometry for time-of-arrival stamping of ultrafast relativistic electron diffraction. Physical Review Special Topics-Accelerators and Beams, 13.2 (2010).

[92] F. Löhl, V. Arsov, M. Felber, K. Hacker, W. Jalmuzna, B. Lorbeer, F. Ludwig, K. H. Matthiesen, H. Schlarb, B. Schmidt, and P. Schmser. Electron bunch timing with

femtosecond precision in a superconducting free-electron laser. Physical review letters, 104.14 (2010).

[93]

[94] S. Winnerl, B. Zimmermann, F. Peter, H. Schneider, and M. Helm. Terahertz Bessel-Gauss beams of radial and azimuthal polarization from microstructured photoconductive antennas. Optics Express, 17.3, (2009).

[95] S. Winnerl. Scalable microstructured photoconductive terahertz emitters. *Journal of Infrared, Millimeter, and Terahertz Waves*, 33.4, (2012).

[96] G. Sciaini, and R. D. Miller. Femtosecond electron diffraction: heralding the era of atomically resolved dynamics. Reports on Progress in Physics, 74.9, (2011).

[97] S. P. Weathersby, G. Brown, M. Centurion, T. F. Chase, R. Coffee, J. Corbett, J. P. Eichner, J. C. Frisch, A. R. Fry, M. Gühr, and N. Hartmann. Mega-electron-volt ultrafast electron diffraction at SLAC National Accelerator Laboratory. Review of Scientific Instruments, 86.7, (2015).

[98] E. Curry, S. Fabbri, J. Maxson, P. Musumeci, and A. Gover. Meter-scale terahertz-driven acceleration of a relativistic beam. *Physical review letters*, 120.9, (2018): 094801.

[99] J. A. Clarke. The science and technology of undulators and wigglers. *Oxford University Press on Demand*, (No. 4). 2004.

[100] Dura Magnetics, Inc. 5500 Schultz Dr, Sylvania, OH 43560, USA https://www.duramag.com/neodymium-magnets-ndfeb/

[101] O. Chubar, P. Elleaume, and J. Chavanne. A threedimensional magnetostatics computer code for insertion devices. *Journal of synchrotron radiation*, 5.3, (1998).

[102] P. Musumeci, J. T. Moody, R. J. England, J. B. Rosenzweig, and T. Tran. Experimental generation and characterization of uniformly filled ellipsoidal electron-beam distributions. *Physical review letters*, 100.24, (2008).

[103] J. T. Moody, P. Musumeci, M. S. Gutierrez, J. B. Rosenzweig, and C. M. Scoby. Longitudinal phase space characterization of the blow-out regime of rf photoinjector operation. *Physical Review Special Topics-Accelerators and Beams*, 12.7, (2009).

[104] R. K. Li, K. G. Roberts, C. M. Scoby, H. To, and P. Musumeci. Nanometer emittance ultralow charge beams from rf photoinjectors. *Physical Review Special Topics-Accelerators and Beams*, 15.9, (2012).

[105] X. H. Lu, C. X. Tang, R. K. Li, H. To, G. Andonian, and P. Musumeci. Generation and measurement of velocity bunched ultrashort bunch of pC charge. *Physical Review Special Topics-Accelerators and Beams*, 18.3, (2015).

[106] P. Musumeci, J. T. Moody, C. M. Scoby, M. S. Gutierrez, and M. Westfall. Laser-induced melting of a single crystal gold sample by time-resolved ultrafast relativistic electron diffraction. *Applied Physics Letters*, 97.6, (2010).

[107] R. K. Li, and P. Musumeci. Single-shot MeV transmission electron microscopy with picosecond temporal resolution. *Physical Review Applied*, 2.2, (2014).

[108] D. Cesar, J. Maxson, P. Musumeci, Y. Sun, J. Harrison, P. Frigola, F. H. OShea, H. To, D. Alesini, and R. K. Li. Demonstration of single-shot picosecond time-resolved MeV electron imaging using a compact permanent magnet quadrupole based lens. *Physical review letters*, 117.2, (2016).

[109] L. Zhao, Z. Wang, C. Lu, R. Wang, C. Hu, P. Wang, J. Qi et al. Terahertz streaking of few-femtosecond relativistic electron beams. *Physical Review X*, 8.2, (2018).

[110] D. Stterlin, D. Erni, V. Schlott, H. Sigg, H. Jckel, and A. Murk. Single-shot electron bunch length measurements using a spatial electro-optical autocorrelation interferometer. *Review of scientific instruments*, 81.10, (2010).

[111] N. I. Agladze, J. M. Klopf, G. P. Williams, and A. J. Sievers. Terahertz spectroscopy with a holographic Fourier transform spectrometer plus array detector using coherent synchrotron radiation. *Applied optics*, 49.17, (2010).

[112] S. Wesch, B. Schmidt, C. Behrens, H. Delsim-Hashemi, and P. Schmser. A multi-channel THz and infrared spectrometer for femtosecond electron bunch diagnostics by single-shot spectroscopy of coherent radiation. *Nuclear Instruments and Methods in Physics Research Section A: Accelerators, Spectrometers, Detectors and Associated Equipment*, 665, (2011).

[113] J. Thangaraj, G. Andonian, R. Thurman-Keup, J. Ruan, A. S. Johnson, A. Lumpkin, J. Santucci et al. Demonstration of a real-time interferometer as a bunch-length monitor in a high-current electron beam accelerator. *Review of Scientific Instruments*, 83.4, (2012).

[114] N. Sudar, P. Musumeci, J. Duris, I. Gadjev, M. Polyanskiy, I. Pogorelsky, M. Fedurin et al. High efficiency energy extraction from a relativistic electron beam in a strongly tapered undulator. *Physical review letters*, 117.17, (2016).